NASA CONTRACTOR REPORT 152402

NASA-CR-152402
19800024811

Large Deployable Reflector (LDR)

W. H. Alff
L. W. Bandermann
M. K. Bartosewcz
R. H. Pohle

CONTRACT NAS2-10427
July 1980

NASA

NASA CONTRACTOR REPORT 152402

Large Deployable Reflector (LCR)

W. H. Alff
L. W. Bandermann
M. K. Bartosewcz
Lockheed Missiles & Space Company, Inc.
Palo Alto, California 94304

Prepared for
Ames Research Center
under Contract NAS2-10427

National Aeronautics and
Space Administration

Ames Research Center
Moffett Field, California 94035

FOREWORD

This report is submitted by Lockheed Missiles & Space Company, Inc. (LMSC), to the National Aeronautics and Space Administration (NASA), Ames Research Center, in fulfillment of contract NAS2-10427.

The support by and cooperation with scientific and technical staff at LMSC is acknowledged. Many helpful discussions with the study monitors and other scientific staff at NASA Ames and Jet Propulsion Laboratory (JPL) are greatly appreciated by the study team. We also owe a special thanks to Cal Tech for a demonstration and discussion of their 10-millimeter antenna construction facilities and to General Research Corporation (GRC) for their electrostatic membrane mirror concept (ECMM). We also thank Kodak Company for freely contributing a paper on lightweight glass mirror technology (Appendix D). A final briefing on the effects of shielding the primary mirror of a large deployable reflector telescope is included as Appendix E.

W. H. Alff (Study Leader)
L. W. Bandermann
M. K. Bartosewcz
R. H. Pohle

ABSTRACT

The results of a technology study are presented for a large, ambient temperature, orbiting astronomical reflecting telescope, which is diffraction-limited at 30 μm. The reflector (LDR) is deployed with one Shuttle load into a ten-year lifetime orbit in the early 1990s. A 10- to 30-m diameter reflector was determined to be feasible with the mirror fabrication and control technology which is now in development.

CONTENTS

ILLUSTRATIONS

TABLES

Section 1
INTRODUCTION AND SUMMARY

1.1 SCIENCE BACKGROUND

From about 30- μm to 1-mm wavelength, the earth's atmosphere is nearly opaque even from high-altitude observatories, yet this spectral region contains continuum and atomic and molecular line radiation from many important astronomical sources. Study of this radiation would yield vital information about star formation, galactic structure and evolution, extragalactic sources, the cosmic background, comets, and planetary atmospheres.

In addition to being nearly opaque, the earth's atmosphere is turbulent and limits the degree of spatial resolution of astronomical sources from the ground. A large ambient temperature telescope in an earth orbit could make important astronomical sources accessible with greater resolution than is possible from the ground even with next-generation ground telescopes. Such a telescope would also complement and in several aspects surpass the capabilities of several orbiting telescopes now in design or under construction.

1.2 STUDY OBJECTIVES AND APPROACH

This report outlines results of a 6-month study of the feasibility and cost of a 10- to 30 m-diameter ambient temperature, infrared-to-submillimeter orbiting astronomical telescope.

The telescope, called the Large Deployable Reflector (LDR), is Shuttle-deployed, free-flying, and has a 10-year mission. It is diffraction-limited at λ=30 μm. Its detailed specifications are listed in Table 1-1.

Table 1-1
LDR SPECIFICATIONS

DEPLOYMENT	PERFORMANCE
(1) Single Shuttle Load	(1) 10-m minimum diameter ambient primary
(2) 1990+ Launch, 1985+ Technology	(2) 10% total emissivity
(3) Automatic or man-assist deployment	(3) Diffraction-limited operation required at $\lambda = 30\ \mu m$, desired at $2\ \mu m$
(4) Low Earth Orbit	(4) Field-of-view 30 $\widehat{s}$ or 10x beamwidth, whichever is larger
(5) 10-yr operational life (1- to 2-yr refurbishing)	(5) Secondary chopping (field-of-view) at 10 Hz
	(6) 180-deg slew in 5 to 10 min
	(7) Pointing stability 1/10 beamwidth
	(8) Stray light below zodiacal light at 60° solar elongation, or below telescope emission (whichever is larger)

Key objectives of the study were:

(1) Identify critical design issues and find promising design approaches to those issues
(2) Assess the state-of-the-art of the critical technologies which support these design approaches
(3) Determine significant breakpoints of the system performance cost and risk, as a function of systems design, aperture size, and operating wavelength
(4) Identify one or more systems concepts which can serve as the basis for further studies

The objectives were achieved by the following approach:

(1) Basic system constraints were determined from specified requirements for size, delivery, life, and performance (Section 2)
(2) Critical design options were identified and evaluated in the areas of mirror technology (Section 3), optical layout (Section 4), figure control (Section 5), and materials and fabrication (Section 6)
(3) Relationships between performance, technology level, and cost were derived for these design options (Section 7)

1.3 STUDY RESULTS

A 10- to 30-m-diameter, ambient temperature, orbiting telescope which is background- and diffraction-limited at 30 μm, is feasible within the stated time frame. A 10-m system is feasible with current mirror technology, while a 30-m system requires technology still in development.

Two conceptual designs satisfying all LDR requirements have been identified which are summarized in Table 1-2 (second and third columns). Both have a segmented primary mirror, and the mirror segments are aligned on a graphite-magnesium support truss. The smaller of the two concepts is 10 to 12 m in diameter, and self-deployable, while for the larger, 15 to 30 m in diameter, the mirror segments are assembled on the previously deployed support structure.

Table 1-2
LDR BASELINE CONCEPTS

Diameter (m)	10 to 12	10 to 12	15 to 30
f/No.	0.5	0.5	0.5
Deployment	Self-deployed	Self-deployed	Assembled
Passive or active	Passive	Active	Active
Segments (4-m diameter)	Al hexel	ULE	Be (solid), or ULE (light-weight)
Support structure	Gr/Mg	Gr/Mg	Gr/Mg
Segment Alignment	Star (Telescope)	Star, Edge Sensing	Star, Trilateration
Operational λ (μm)	500	30	30
Cost ($M)	250	250	500

Both systems use active alignment of the mirror segments to be diffraction-limited at 30 μm. Neither requires a sunshade for background-limited operation, but may require one for thermal control of the primary. The point deserves further study.

Active control of the segment shape (in addition to position) is not required. A totally passive LDR would be self-deployed (10- to 12-m diameter) and diffraction limited at 500 μm at best. Although this concept does not satisfy all LDR requirements (Table 1-1), it is listed in Table 1-2 (Column 1) as an alternative concept representing a near-millimeter version of an LDR. It may be further studied if a near-millimeter rather than a near-infrared large, orbiting, astronomical telecope is seriously considered in the future.

Significant cost breakpoints, as a function of either operating wavelength or primary mirror diameter, probably do not exist. Satellite cost of a 10-m LDR is approximately $250 M, of a 30-m LDR $500 M, excluding Shuttle, special facilities, and focal plane costs.

Section 2
BASIC CONSIDERATIONS

2.1 SUMMARY

Constraints on delivery and deployment of the LDR are evaluated. For a 10-year orbit lifetime, the required orbit altitude is 700 km. The systems weight budget is discussed. The budget allows for a 10-m-diameter mirror, a maximum areal density (reflector mass/area), corresponding to Space Telescope technology ($\sim$180 kg/m^2), whereas a 30-m-diameter mirror allows 25 kg/m^2, thereby requiring a very advanced mirror technology. Radiation from the primary mirror is the major background of LDR, and therefore a sunshade or telescope baffle tube is not needed except for control of temperature gradients of the mirror.

2.2 ORBIT AND DEPLOYMENT

The LDR requirements for delivery, deployment, and lifetime are basic system constraints, affecting the choices for size, weight, and orbital altitude. These three parameters are interdependent and can be optimized in an iterative process. For example, the minimum altitude of a 10-year life orbit depends on the system's ballistic coefficient and, therefore, on the total mass and area, specifically on m/A. The maximum on-orbit mass depends on the Shuttle capacity and on the fuel requirements to boost the satellite from a Shuttle handoff to its orbit. The fuel requirements in turn depend on the satellite mass.

As with the Space Telescope, a circular, low inclination (28.5 deg) orbit is assumed, giving maximum Shuttle payload capability. We assume a 1990 launch, and recognize two possible scenarios. In the first, the orbit has a 10-year life. In the second, the initial altitude is sufficient for only a 2- to 3-year life, but the satellite is reboosted, at 2-year intervals, at a time when the spacecraft and telescope are refurbished. The second scenario would permit an only slightly

lower initial altitude orbital altitude (Fig. 2-1). We therefore did not investigate this scenario in more detail. For a 10-year lifetime, the orbital altitude is about 700 km.

Direct insertion by the Shuttle into a 700-km orbit is uneconomical and involves a large payload weight penalty (Fig. 2-2). Therefore, the satellite will be boosted by a small engine from 200-nmi Shuttle handoff. The required propulsion mass (fuel and engine) is about 3500 kg. This leaves a LDR payload of 25,000 kg.

2.3 WEIGHT, VOLUME, AND MIRROR TECHNOLOGY

The payload constraint of the LDR sets an upper limit to the ratio mass/area and thereby constrains the required mirror technology, a strong function of m/A.

LDR has tasks similar to the Space Telescope, A weight budget for the spacecraft, scaled from ST, is given in Table 2-1: the total mass is about 3000 kg. not including instruments. Since LDR will presumably be a multipurpose facility like ST, the instrument package weight will be similar (~1500 kg). Substracting 4500 kg from a 25,000-kg maximum payload, we obtain a maximum reflector weight of 20,500 kg, which is the sum of that of a support structure and of the dish itself. Anticipating results of the study, we assume the reflective surface to be segmented (hexagonal segments of glass or beryllium) and supported by a composites structure (in fact, graphite/magnesium).

The weight of that support structure is 15% to 25% of the dish, depending on reflector size (the percentage increasing with reflector diameter). With these considerations, we can now calculate the maximum areal density of the segments; the results are shown in Fig. 2-3 for various diameters of the primary mirror.

The figure illustrates a strong dependence of areal density, and thereby of the required mirror technology, on mirror diameter. A "small" LDR (10- to 12-m diameter) can be built with proven technology, because the areal density can be similiar to that for ST (180 kg/m^2). However, a "large" (25- to 30-m diameter)

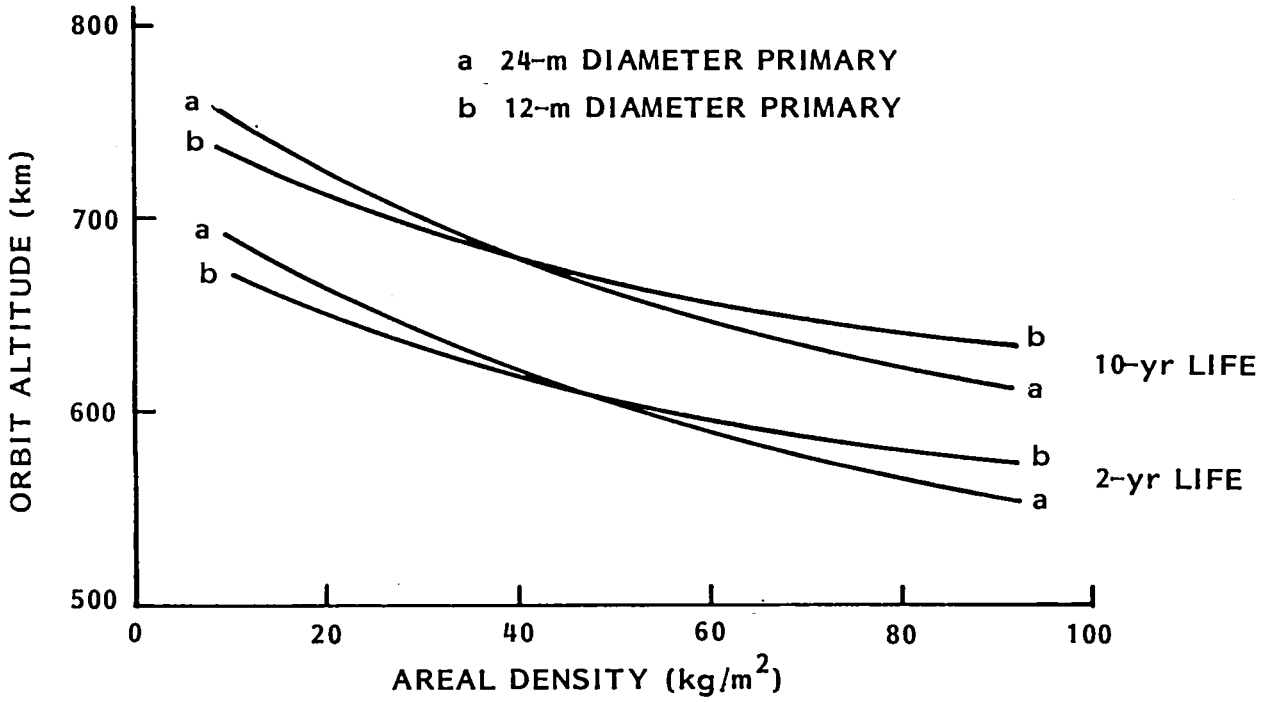

Fig. 2-1 Initial Altitude Requirements

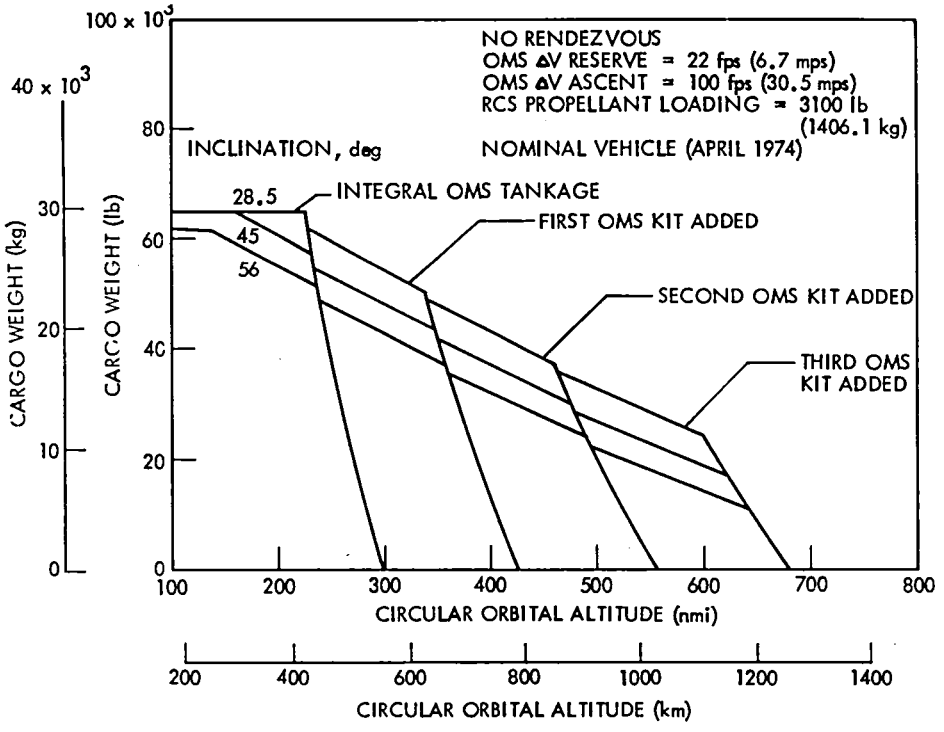

Fig. 2-2 Shuttle Orbit Capabilities

Table 2-2 LDR SPACECRAFT WEIGHT (kg)

Electrical Power (incl. solar panels)	640
Communications Data Management	203
Guidance, Navigation	61
Pointing Control	500
Thermal Control	200
Structure	1261
Total	2875

LDR requires mirror technology quite advanced from ST and, in fact, also from currently developed lightweight glass mirror technology represented by the FRIT technology. The required $m/A=25\ kg/m^2$ is near the value for the Cal Tech millimeter ground telescope ($15\ kg/m^2$).

The width of the Shuttle bay restricts the maximum diameter of the mirror segments to about 4 m. The maximum allowed segment thickness depends on the total mirror diameter. A possible scenario is illustrated in Fig. 2-4 for a 20-m telescope, assuming 10 m of Shuttle payload are allowed for the segments. The required segment thickness is 26 cm (Fig. 2-5), and the total aspect ratio of the LDR mirror (diameter/thickness) is 77. The ratio is much larger than for the Space Telescope, 8 representing current mirror technology.

2.4 SUN SHIELD

A sun shield or baffle can reduce low stray light on the focal plane and provide temperature uniformity over the primary mirror. We have not studied the latter but have investigated the former by estimating the background noise from principal sources in the sky and from the telescope itself. Details are given in Appendix A. The various contributions to the noise-equivalent power (NEP) on a diffraction-limited detector are shown in Fig. 2-6. We estimate that the primary mirror temperature will be approximately 200 K, and the total emissivity 0.06. A 10% spectral bandwidth is assumed. The sky noise (infrared zodiacal light, diffuse galactic light, and cosmic 3 K background) is far less than that of the optics, sun illumination at 60 deg, and the earth albedo and earth shine. Thermal emission by the optics dominates for wavelengths greater than 10 μm. Since the LDR operates primarily above 30 μm, we

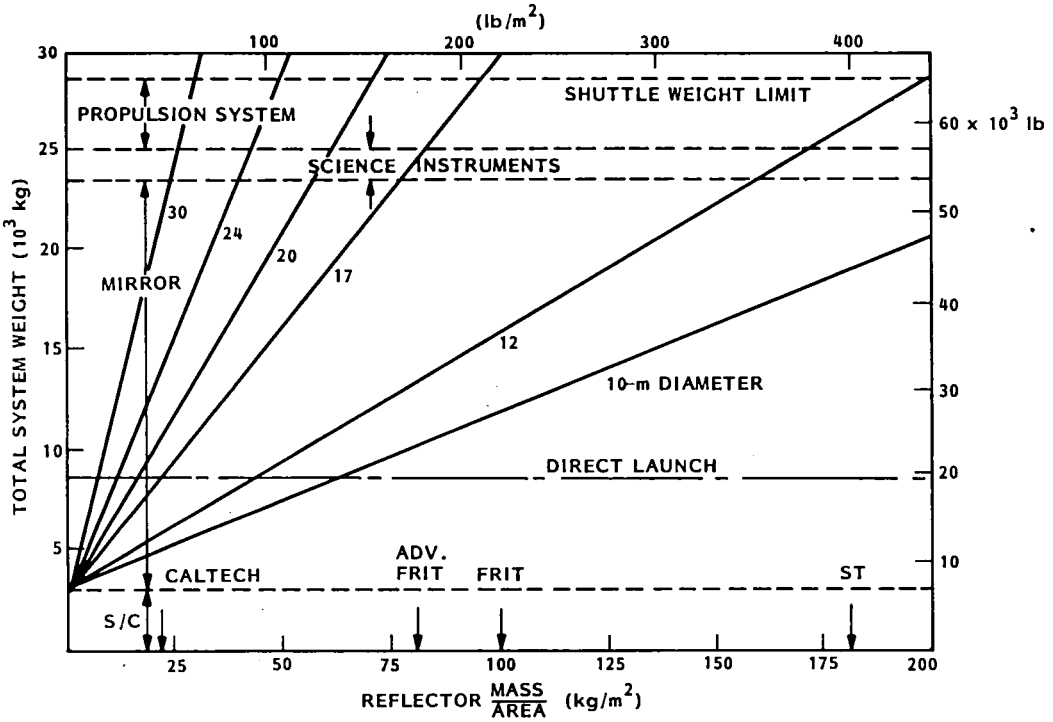

Fig. 2-3 System Weight Budget (720-km Orbit)

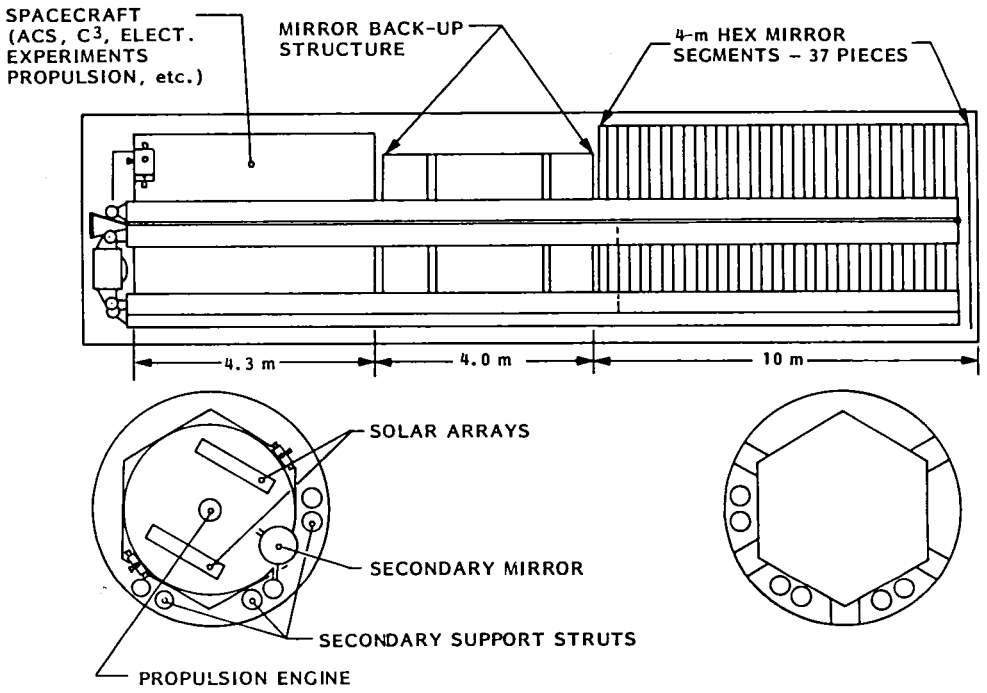

Fig. 2-4 20-m Telescope – Stowed

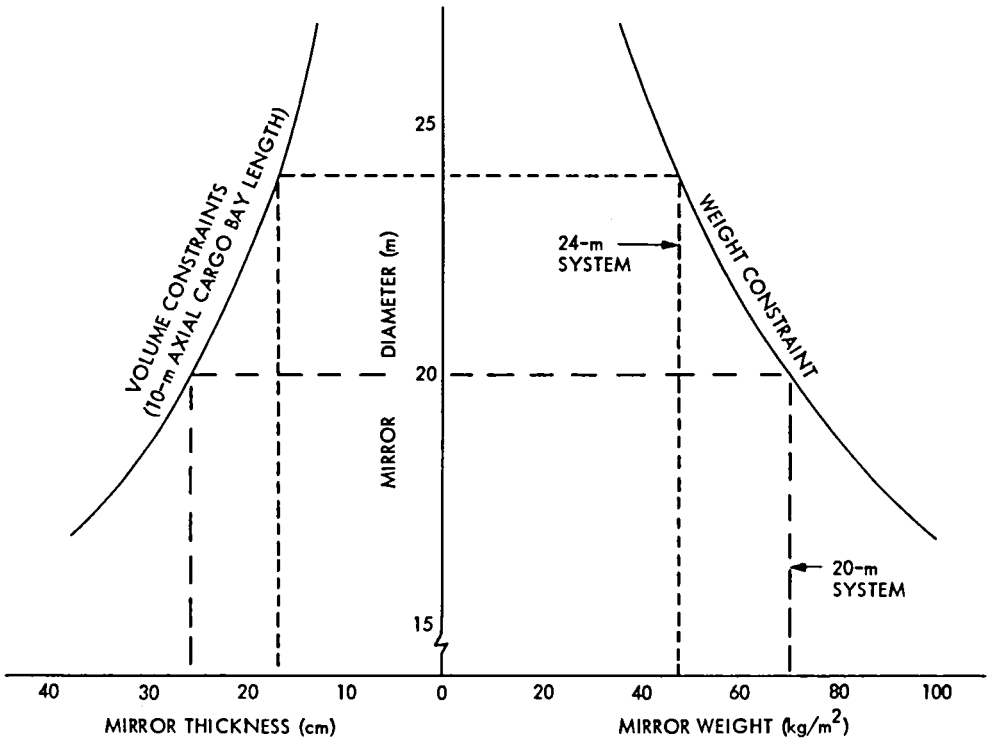

Fig. 2-5 Shuttle Constraints

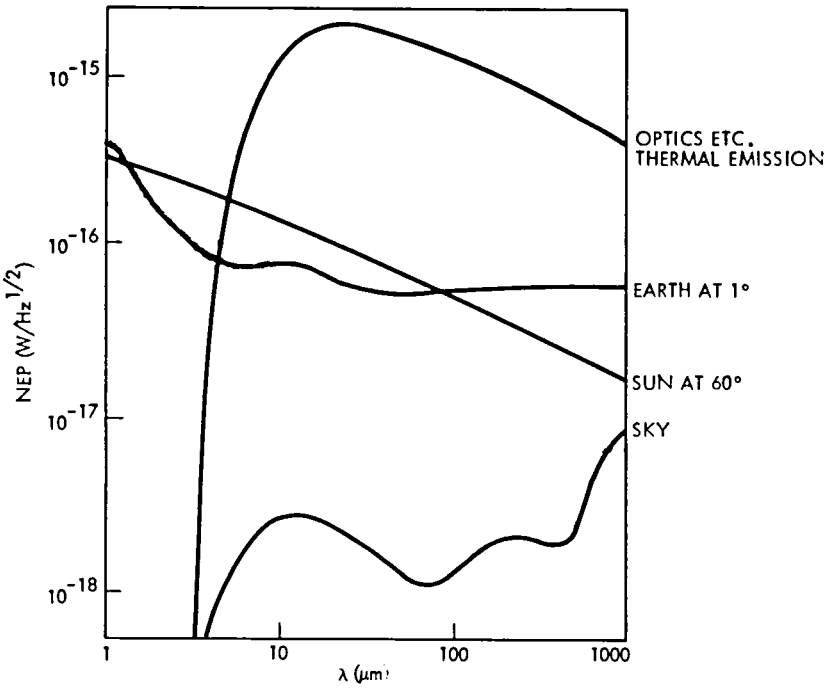

Fig. 2-6 LDR Sensitivity Limits Summary

conclude that a sun shield is not necessary for the purpose of achieving minimum background. Nonetheless, it may be necessary for thermal control of the mirror; i.e., thermal uniformity over the mirror surface required for chopping over the FOV, and minimum gradients across and through the mirror for minimum thermal distortion. Additional analysis is required.

Section 3
REFLECTOR CONCEPTS

3.1 SUMMARY

Section 2 showed that a large primary mirror for LDR must be lightweight and thin. It must also be deployed automatically or semiautomatically. In this section we evaluate the potential of various current candidate concepts of such reflectors for their applicability to LDR. Among current design concepts of large, deployable, lightweight space reflectors, only those are viable for LDR which have a segmented primary using rigid reflector panels which are aligned in real time. Self-deployable (unfolding) concepts have a maximum mirror diameter of 10 to 12 m, assembled concepts (segments placed on separate structure) of about 30 m.

3.2 OVERVIEW

For diffraction-limited performance at wavelength λ, the LDR mirrors have a surface accuracy of $\lambda/20$ rms. There are two types of reflector surfaces. "Hard" reflectors can maintain the shape by structural strength. Such reflectors have a large ratio m/A and imply a large mass for the system as a whole. Reflectors with "soft surfaces" maintain their shape by tension. They can have very low areal densities; i.e., low total weight. Because of their packagability and low mass, the soft reflectors appear most attractive for very large systems. However, none of the present concepts are viable for LDR. The mesh antennas, although well developed and flight-proven, are inherently limited to (and indeed intended for) applications at $\lambda > 1$ mm. The membrane mirrors, on the other hand, have the potential to work well at infrared wavelengths, but they are insufficiently developed to be ready in the LDR time frame.

Hard reflectors have rigid mirror panels aligned on a rigid support structure. We define such reflectors as self-deployable if panels and structure unfold automatically and as a unit; assembled, if the panels must individually be placed on a previously deployed support structure.

Figure 3-1 shows outstanding examples of the four reflector concepts: mesh and membrane antennas (soft), and the self-deployed and assembled reflectors (hard). We shall evaluate each in turn.

3.3 MESH ANTENNA

This type of reflector is represented in Fig. 3-1a by the Lockheed wrap-rib antenna. It has a finely woven or knitted mesh stretched between and attached to a large number of ribs of the required parabolic shape. In the stored configuration, the ribs are wrapped around a central hub. They are deployed and can be refurled in a controlled manner by a power-driven spool. In other designs, the ribs are folded forward or back rather than wrapped around a central hub. In current systems, the ribs are made with aluminum, but they will in the future be made from a thermally superior material such as graphite/epoxy or a graphite/metal.

Since the reflector mesh is stretched between the ribs, the reflecting surface shape is only approximately parabolic. The surface contour accuracy can be improved by controlling the mesh contour between ribs. For that case, the mesh fineness sets a limit to the achievable surface accuracy. The minimum operational wavelength of the mesh antenna is thus determined by the number of ribs, the mesh quality and type, the accuracy of the rib positions (particularly of the tips), the hub rigidity, as well as the thermal and dynamical factors. Current estimates of the limiting frequency of performance, shown in Fig. 3-2. suggest that a 10-m-diameter antenna would work at $\lambda = 2.2$ mm. This value is above the wavelengths of interest to LDR. We conclude that the mesh concept is not viable for LDR.

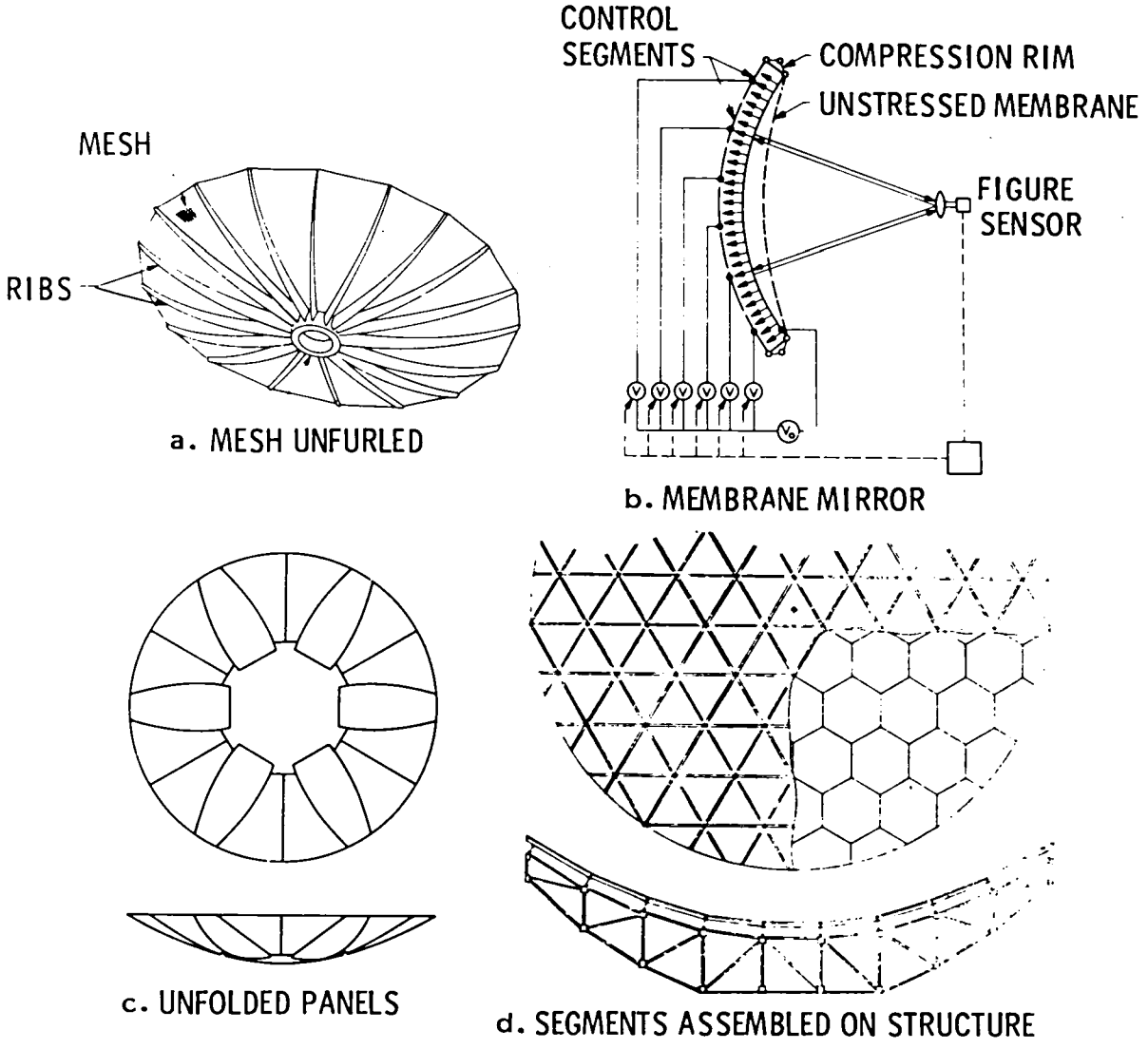

Fig. 3-1 Lightweight Reflector Concepts

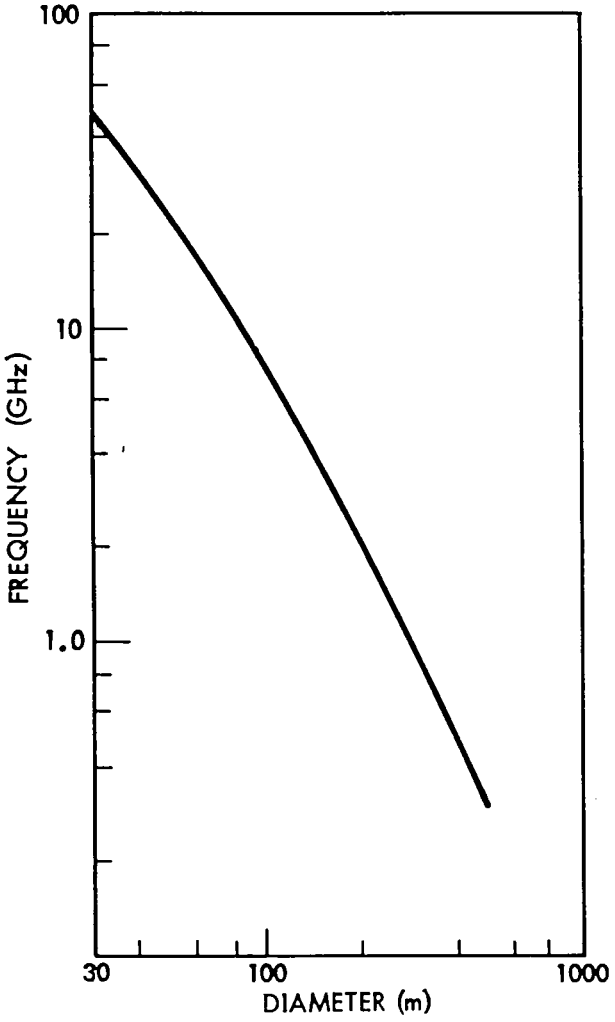

Fig. 3-2 Limiting Frequency for Wrap-Rib Reflector

3.4 MEMBRANE REFLECTOR

The key elements of an electrostatically controlled membrane mirror (ECMM) are shown in Fig. 3-1b (a General Research Corporation concept): the reflecting membrane is shaped to a paraboloid by electrostatic forces attracting it to a control surface (which may be soft or rigid), under the control of a surface contour evaluation system. The membrane, held inside a tension ring, can be flat or concave in its relaxed state. (For low f/nos., a concave shape may be required.) The control surface contains a number of electrodes suitably shaped and held at various potentials, relative to the front (i.e., reflecting) member. The electrostatic attraction force on the membrane varies rather smoothly over the surface because of edge effects. This contrasts sharply with the point-like character of the mechanical force applied by actuators in the hard reflector concept discussed later. The force tends to shape the membrane naturally to the typically concave reflector shape.

The ECMM has inherent characteristics suited for a large space reflector including low m/A ratio. Its development is still at a stage of demonstrating the concept feasibility: no flight or ground-proven membrane telescope exists as yet. There are no apparent fundamental physical difficulties – questions of principle – but there may be many practical challenges which cannot be met within the LDR time frame. Some of these are: (1) manufacturing high-quality membranes; (2) operating near the membrane's yield limit or near electromechanical

instabilities;* (3) operability in the space environment; (4) effective electrostatic shielding to prevent breakdown or large changes in the electrostatic field by solar wind and cosmic rays; (5) effect of seams of the membrane (unavoidable for large reflectors); and (6) effective thermal and dynamic control. We therefore think that the membrane mirror is not a viable LDR concept.

3.5 SELF-DEPLOYABLE REFLECTOR

The example of a segmented self-deploying reflector having "hard" mirror segments is shown in Fig. 3-1c (TRW Sunflower). This 10-m-diameter concept has 6 main mirror panels which are hinged to a central panel and to 12 other panels. It has also a support and stiffening ring underneath the dish which is not shown in the figure. The shape of the panels is computer-designed for efficient packaging; their structural rigidity is sufficient to withstand Shuttle launch loads. The panels are spring-deployed against precision-designed stops for high deployment accuracy.

All designs are for low f/nos. (f/0.4) since they are intended for narrow field-of-view communication applications. The packagability, and therefore the maximum reflector diameter, increases slightly with increasing f/no., but for a single ring of panels, the maximum diameter is about 13 m. For larger diameters additional rings are required. Advanced Sunflower designs employ up to 3 rings of reflector panels, thereby allowing a total diameter of up to 25 m (one Shuttle load limit). The complexity and, thereby, the risk of failure of the deployment mechanisms, and the resulting reduced deployment accuracy, make multiring self-deployable concepts noncompetitive with the assembled reflector concept discussed later.

---

*Work at MIT is exploring this problem.

The achievable surface accuracy of the TRW Sunflower depends on the manufacturing accuracy and provisions for post-fabrication adjustment of the panels. Presently, the panels are made of thin (1/2 in. for a 10-m dish) aluminum honeycomb sandwich, and the reflecting surface layer is graphite/epoxy. Such panels cannot provide the accuracy required for infrared work. This point is substantiated by TRW's estimates of surface accuracy achievable with present (I) and advanced (II-IV) Sunflower technology (Fig. 3-3). The technologies represented are: I, present; II, improved panel fabrication; III, post-fabrication panel adjustment; and IV, on-orbit active panel control.

To obtain the figure accuracy required for LDR, the panels must be stiffer and have a better surface layer. Assuming an inert support structure and perfectly rigid panels, the accuracy of a self-deployed reflector depends on the achievable

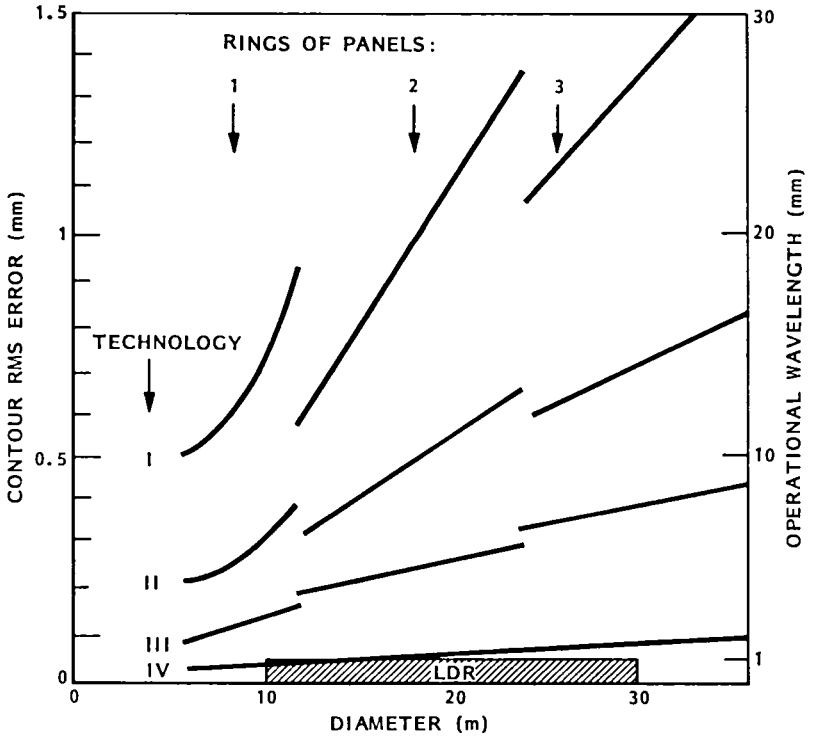

Fig. 3-3 TRW Sunflower Surface

deployment accuracy. A best engineering estimate is 2.5 μm/contact assuming lapped, polished contact surfaces free of contaminents. A total of 10^2 contacts is estimated for deployment of a 10- to 12-m system. Thus, the rms accuracy is $\sqrt{10^2} \times 2.5\ \mu m = 25\ \mu m$.

Assuming no change in that accuracy after deployment, we conclude that a totally passive deployed telescope (no active panel alignment such as discussed in other sections) can work at 500 μm. This number is necessarily "soft," but it is close to that achieved for the Cal Tech 10-m (assembled) dish (discussed in the next section). Active alignment, discussed in Section 5, can lower the minimum wavelength from 500 to 30 μm. Thermal analysis of the support truss also shows (section 5.4) that thermal distortion of the truss by sun-soak-induced gradients limits a passive reflector to operations near or above 1 mm.

A LMSC conceptual design of a self-deployable LDR is shown in Fig. 3-4, in stored and deployed configuration. It has a center panel, 4-m in diameter, and 8 panels of quasi-pie shape and 4-m-maximum diameter. Four of the panels are stored forward, the others behind the spacecraft. The central support truss column telescopes. The diameter of this reflector is 11.2 m, close to the maximum diameter of a single-ring, self-deployable reflector stowable in the Shuttle bay.

In summary, a viable, 10 to 12 m, self-deployable LDR has

- A thermally and dynamically inert mirror support structure (e.g., made of graphite/magnesium, cf. Section 5 and 6)
- Stiff reflector panels (e.g., lightweight glass, cf. Section 6)
- An active panel alignment system (cf. Section 5) for operations to 30 μm. A passive system could only work to ~ 500 μm

3.6 ASSEMBLED REFLECTOR

The maximum possible diameter of a self-deployable reflector is limited due to inefficient packaging: clearly there is much unused space in the Shuttle between the reflector panels. For more efficient packaging, the panels are stacked parallel

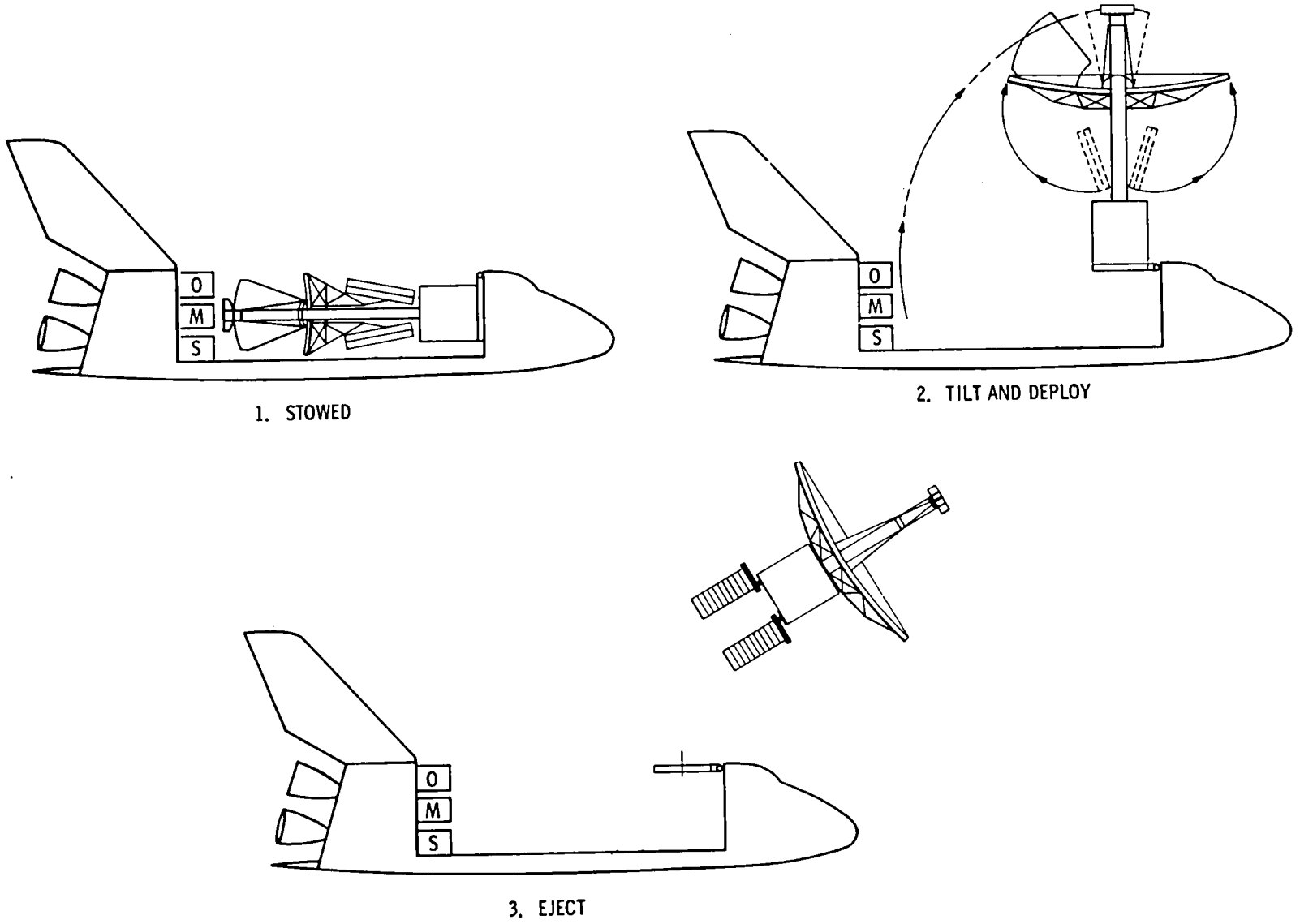

Fig. 3-4 11-m Self-Deployed Telescope

to each other. This, however, requires that the panels should have a similar size and shape. The preferred shape is hexagonal, which allows efficient use of mirror materials and of storage volume.

The concept of a ground-based reflector using hexagonal segments on a precison support structure has been spendidly realized by Prof. Leighton and his collaborators at Cal Tech. The f/0.4, 10-m-diameter dish (three have been built thus far) has 84 hexagonal Al Hexcel Honeycomb panels, 1.1 m in diameter and 3-in. thick. The concept is shown in Fig. 3-1d. The reflecting surface is 1-mm-thick aluminum skin epoxied to the segment. The total weight of the dish is 4735 kg, and the areal density of a segment is 15 kg/m^2.

The parabolic surface of the reflector is shaped as a unit, using a high-speed rotating cutting blade, with all panels in place on the steel-tube support truss. A close-up of the precision panel support system is shown in Fig. 3-5. Leighton's careful design of the system, and ingenious fabrication and surface measurement techniques, have resulted in a measured figure accuracy of less than 25-μm rms. This accuracy is reproduced even after disassembling, transporting, and reassembling the telescope. Leighton hopes eventually to achieve a surface accuracy of 2.5-μm rms; this would make a reflector workable at $\lambda = 50\ \mu m$.

We doubt that this goal can be attained also for a space reflector, if similar components and materials are used. Two major challenges will arise from (1) testing the dish in a 1-g environment while it is intended for a 0-g environment; and (2) automatic or semiautomatic deployment from the Shuttle. The thermal environment of an earth orbit suggests a thermally more favorable material, such as low-expansion glass or ceramics, or beryllium for the panels rather than aluminum; and a composite, Gr/metal, rather than steel for the truss. The change of materials could have a major impact on fabrication, assembly, and testing procedures. The Leighton dish could be self-deployed or assembled. In fact, Leighton has suggested deployment without a substantial structural support structure. In all probability, a support truss will be required for greater thermal and dynamical stability of the system. The problem is addressed in Section 5.

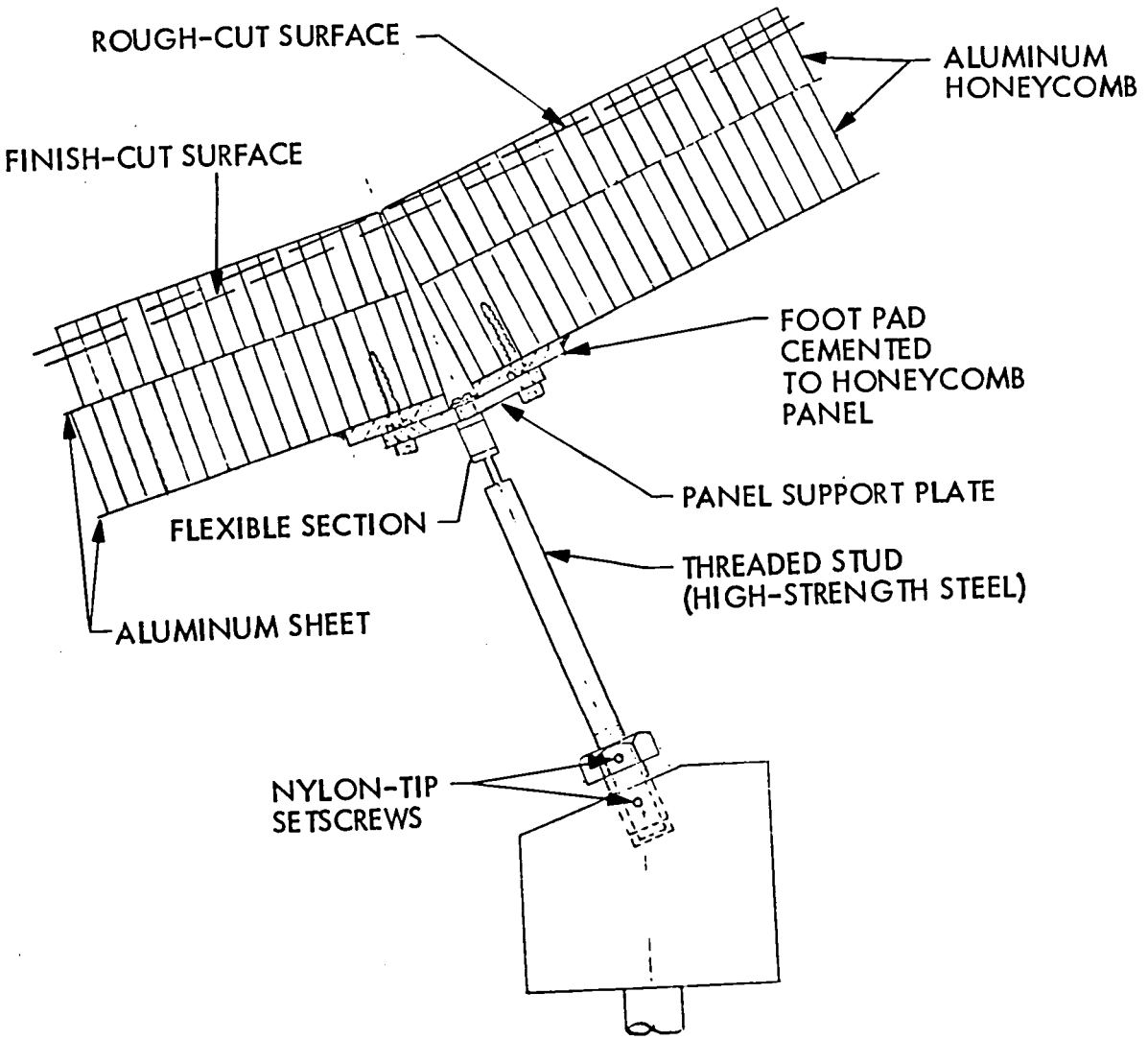

Fig. 3-5 Cal Tech 10-m Dish Panel Support

A feasible concept of a Leighton-type reflector will thus have lightweighted, low-expansion glass or solid beryllium panels on a metal-matrix support truss. The maximum reflector diameter is about 30 m. This value gives a maximum areal density of a reflector segment (allowed by the shuttle payload weight limits) of 25 kg/m^2, which is judged to be a near practical lower limit attainable in the LDR time frame. Storage in the Shuttle bay and deployment of such a reflector are shown in Fig. 3-6. The exact value of the reflector diameter can be chosen more precisely on the basis of efficient uses of mirror material as well as Shuttle payload bay. For example, the reflector panels at the rim of the dish, which are fractions of hexagons, can be placed together, and the total stack length can thereby be minimized. Figure 3-7 shows the resulting relationship between mirror thickness and stack length for several values of the total diameter, D.

As shown in Fig. 3-6, placing the mirror segments on the (previously deployed) support truss is done using the Remote Manipulating system (RMS) of the Shuttle.

The mirror support truss is held in place rigidly during the mirror assembly. Any relative motion between the telescope structure and the Shuttle must be avoided, because physical contact could damage flight-sensitive surfaces or thermal protection layers of the Shuttle.

3.7 CONCLUSION

Viable LDR reflector concepts have a segmented, actively aligned, hard mirror on a support truss. Self-deployable reflectors are limited from 10 to 12 m diameter, those requiring assembly to about 30 m. Two active LDR concepts are summarized in Table 1-2; both use active panel alignment systems but are different in terms of either performance, material, design, and use, and therefore also in terms of cost and risk. Details of the reasoning for justifying the choices of materials and designs are given in Sections 4 through 6.

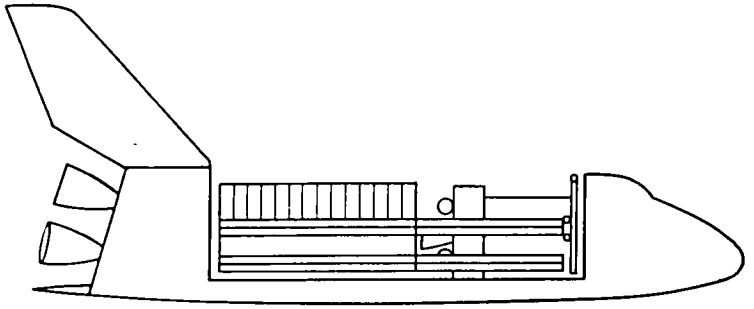

1. STOWED

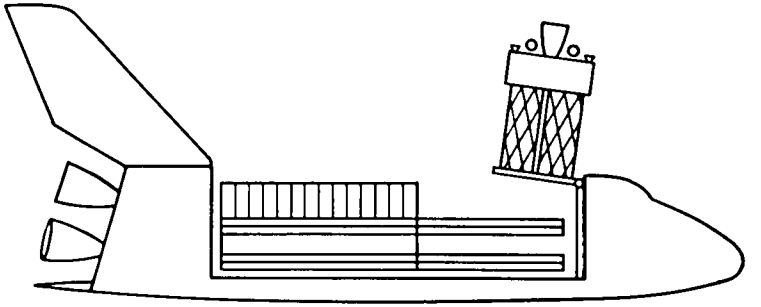

2. TILT TABLE ERECTION

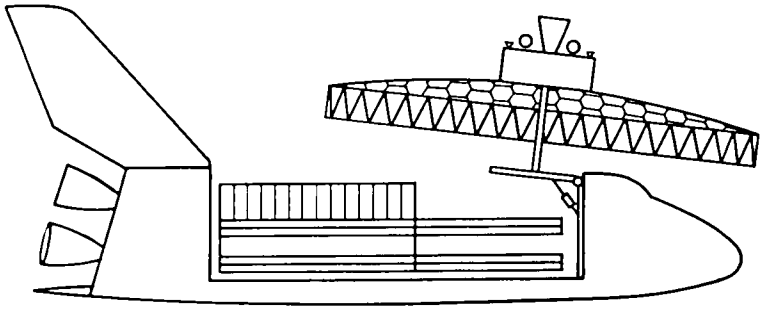

3. SUPPORT STRUCTURE ERECTED

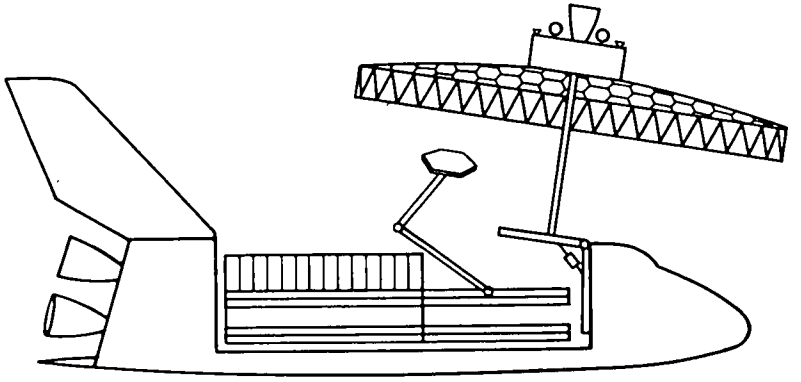

4. SEGMENT INSTALLATION

Fig. 3-6 Deployment of Segmented Telescope

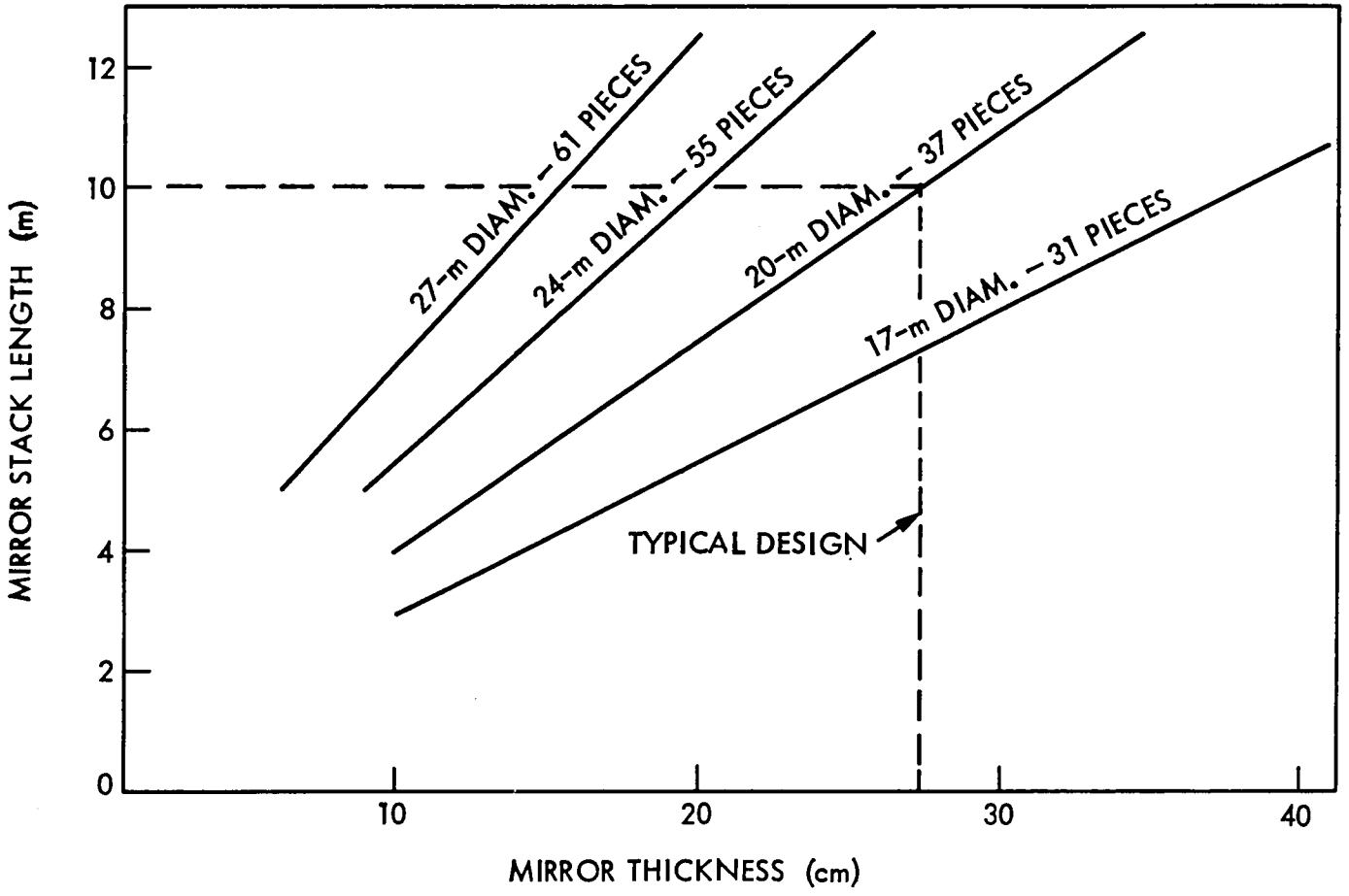

Fig. 3-7 Typical Mirror Stowage Requirements

Section 4
OPTICAL CONFIGURATION

4.1 SUMMARY

The preferred configuration of LDR is a two-mirror Cassegrain with a f/0.5 parabolic primary mirror. Such a system satisfies the optical requirements. Other systems are either unnecessarily complex or do not meet these requirements. The section outlines the analyses and tradeoffs leading to these conclusions.

4.2 SELECTION OF TWO-MIRROR CONFIGURATION

The LDR field-of-view requirements (Table 1-1) can be satisfied by the easily deployed two-mirror parabolic Cassegrain configuration. Telescopes of three or more mirrors can utilize spherical primaries but are less desirable because of packing inefficiencies, alignment problems, multiple elements, and structural complexity. If there were an overriding cost or fabrication advantage in the use of a spherical primary, the complexity inherent in three-mirror systems might be acceptable. In the infrared, however, no such advantages are apparent. With close attention paid to grinding metrology, mirror surface figure errors equivalent to 0.6-μm wavefront error (WFE) may be achieved in grinding, after which the mirror can be polished "to remove the gray." Therefore, for telescope diffraction-limited operation at $\lambda = 30\ \mu$m, mirror fabrication tolerances are sufficiently relaxed so that the parabolic figure can be achieved in grinding. [For a 2-μm diffraction-limited telescope, the extra time and cost required to obtain a parabolic rather than a spherical mirror is appreciable (although exactly how much more extra effort is required depends on as yet undefined mirror fabrication techniques).] For the LDR application, the greater complexity of the three-mirror system relative to the two-mirror telescope makes a two-mirror system preferable.

4.3 BASIC PARAMETERS OF THE TWO-MIRROR TELESCOPE

The telescope configuration is shown in Fig. 4-1. The primary mirror has a diameter D and a focal ratio F. The convex secondary is near the prime focus and the principal focal plane is at the primary vertex. This focal plane position simplifies the optical analysis, and small changes in the position will not significantly affect our conclusions on system performance.

The secondary magnification is

$$m = F/F_T \tag{4.1}$$

where F_T is the telescope focal ratio. The primary-to-secondary separation is

$$S = \frac{m}{m+1} D F \tag{4.2}$$

The magnification and the diameter of the secondary are related by

$$D_s = D/(m+1) \tag{4.3}$$

(the secondary is slightly oversized to avoid vignetting). The choice of m also affects the focal plane size for a given FOV. An object at angle, α, from the telescope optical axis is imaged in the focal plane at a distance $\alpha F_T D = \alpha mFD$ from the optical axis. As a starting point, we select m on the basis of minimum obscuration. For this condition, the secondary mirror diameter equals the focal plane diameter required by the maximum FOV, $2\alpha_{max}$. This gives

$$\frac{D}{m+1} = 2\alpha_{max} mFD \tag{4.4}$$

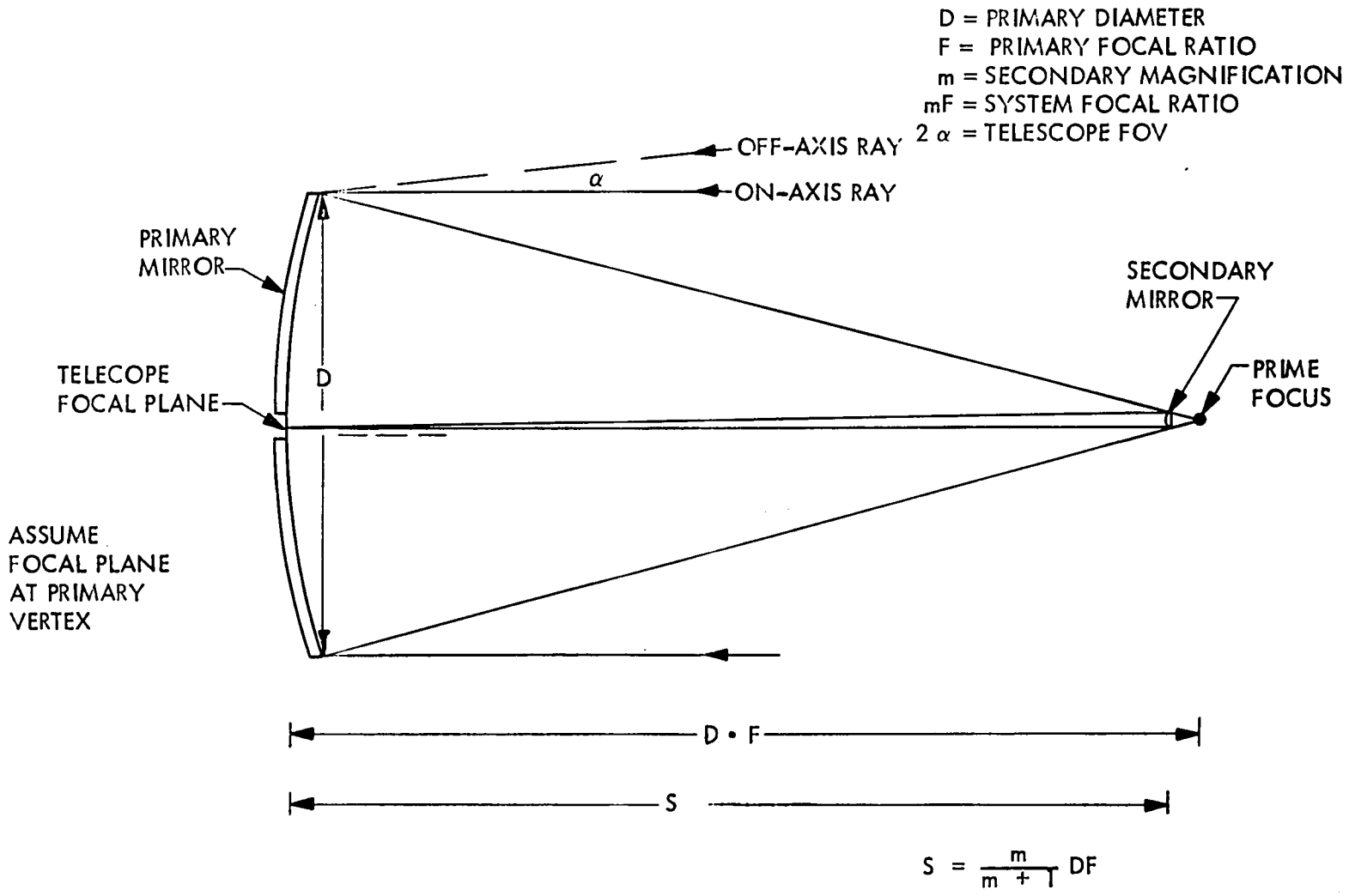

Fig. 4.1 Two-Mirror Telescope Concept

By SOW specification, the half-width of the FOV, α_{max}, must be 5 Airy disk diameters at the longest working wavelength, λ_{max} = 1 mm:

$$\alpha_{max} = 1.22 \times 10^{-2}/D \ , \quad D \text{ in meters.} \tag{4.5}$$

This condition gives

$$m \sim 6.4 \sqrt{D/F} \ , \ D \text{ in meters} \tag{4.6}$$

since m >> 1.

Substitution of values of the primary diameter, D, from 13 to 30 m, and focal ratios from 0.5 to 2, yield magnification ratios from 14 to 50. Such high ratios give small secondary mirror diameters. Substitution of Eq. (4.6) into Eq. (4.3) gives

$$D_s = 0.156 \sqrt{DF} \ , \ D \text{ in meters.} \tag{4.7}$$

Typcial values of D_s range from 35 cm to 1 m. Larger secondaries are more difficult to deploy, support, align, and adapt to secondary chopping.

The advantages of a low primary focal ratio (F = 0.5) are apparent. Not only is the telescope short – implying easier packaging and deployment and a stiffer structure – but also the secondary mirror and the focal plane are small. For F = 0.5 telescopes diffraction limited at 30 μm (as required for LDR), the alignment tolerances and optical performance are acceptable. However, for a F = 0.5, 2-μm telescope, a goal but not requirement for LDR, the alignment tolerances are difficult to meet with existing sensors and mirror fabrication is more difficult, although possible; field aberrations are acceptable. Therefore, for a 2-μm telescope, the choice of the most cost effective primary focal ratio is an issue requiring further study.

4.4 FIELD ABERRATIONS OF THE TWO-MIRROR TELESCOPE

Four designs were considered: (1) Ritchey-Chrétien; (2) parabolic primary; (3) tilted aplanat; and (4) spherical primary. Third-order aberration theory of Bottema and Woodruff* was used to estimate the field aberrations of these designs, as a function of fundamental telescope parameters, D, F, m, and α_{max} discussed above. None of the designs have third-order spherical aberration, but they do exhibit field curvature and distortion.

Field curvature can be removed by a sensor design which conforms to the curved field. Distortion does not affect point source imagery and can be removed by image processing. The remaining aberrations are coma and astigmatism. Algebraic expressions for the corresponding rms wavefront errors as a function of telescope design parameters are given in Table 4-1 and in Appendix B.

Table 4-1

THIRD-ORDER FIELD ABERRATIONS OF VARIOUS TWO-MIRROR TELESCOPES

OPTICAL CONFIGURATION

ABERRATION	RITCHEY CHRÉTIEN	PARABOLIC PRIMARY	TILTED APLANAT	SPHERICAL PRIMARY
COMA (rms WAVES)	0	$\frac{D\ \alpha}{96\sqrt{8}\,m^2\,\lambda\,F^2}$	$\frac{(m^2-1)D\,\alpha'}{192\sqrt{8}\,m^2\,\lambda\,F^2}$	$\frac{(m^3+2)D\,\alpha}{192\sqrt{8}\,m^2\,\lambda\,F^2}$
BEST FOCUS AND ASTIGMATISM MIXTURE (rms WAVES)	$\frac{(2m+1)D\,\alpha^2}{32\sqrt{6}\,m\,\lambda\,F}$	$\frac{D\,\alpha^2}{16\sqrt{6}\,\lambda\,F}$	$\frac{(m+2)D\,\alpha^2}{32\sqrt{6}\,\lambda\,F}$	$\frac{(m^2-4)D\,\alpha^2}{64\sqrt{6}\,\lambda\,F}$

α' ≡ Relative look angle of object to primary mirror axis

*Applied Optics, Vol 10, No. 2, 1971, pp. 300-303. See also Vol. 11, No. 12, 1972 p. 2965.

Both the spherical primary and the tilted aplanat fail to provide diffraction limited performance over entire FOV. By contrast, the Ritchey-Chrétien and parabolic designs actually exceed that requirement. As shown in Fig. 4-2, the largest wavefront error, 0.8 μm rms, is present at the FOV edge of the F = 0.5, D = 10-m system. In all cases, the field aberration is easily less that 0.2 μm over the central 30 $\widehat{s}$ FOV. Finally, the table also shows that the limiting aberration is astigmatism rather than coma. In other words, at field angles large enough so that rms wavefront error exceeds that amount defined as "diffraction limited" (i.e., λ/10 rms at the minimum working wavelength of 30 μm), astigmatism is larger than coma. This fact has two important consequences:

(1) The parabolic primary is better suited to the LDR requirements than the Ritchey-Chrétien design. Not only is the astigmatism slightly lower, but, more importantly, the excellent prime focus on-axis imagery simplifies mirror testing. It also allows for on-orbit conversion to a prime focus instrument

(2) Since third-order astigmatism is not a function of secondary magnification for a parabolic primary, telescope performance is nearly independent of the particular values of F_T and D_s (which may be determined by system considerations outside the scope of this study).

The rms wavefront error at best focus of a parabolic primary is plotted in Fig. 4-2 as a function of field angle. The crosses denote data points obtained with the optical design program ACCOS-V. Close agreement between Table 4-1 and results from this program was observed in all cases selected.

In summary: (1) a parabolic primary gives diffraction limited performance over the entire FOV without undue complexity; (2) a primary focal ratio of F = 0.5 is acceptable for a telescope working wavelength as low as 30 μm and possibly to 2 μm.

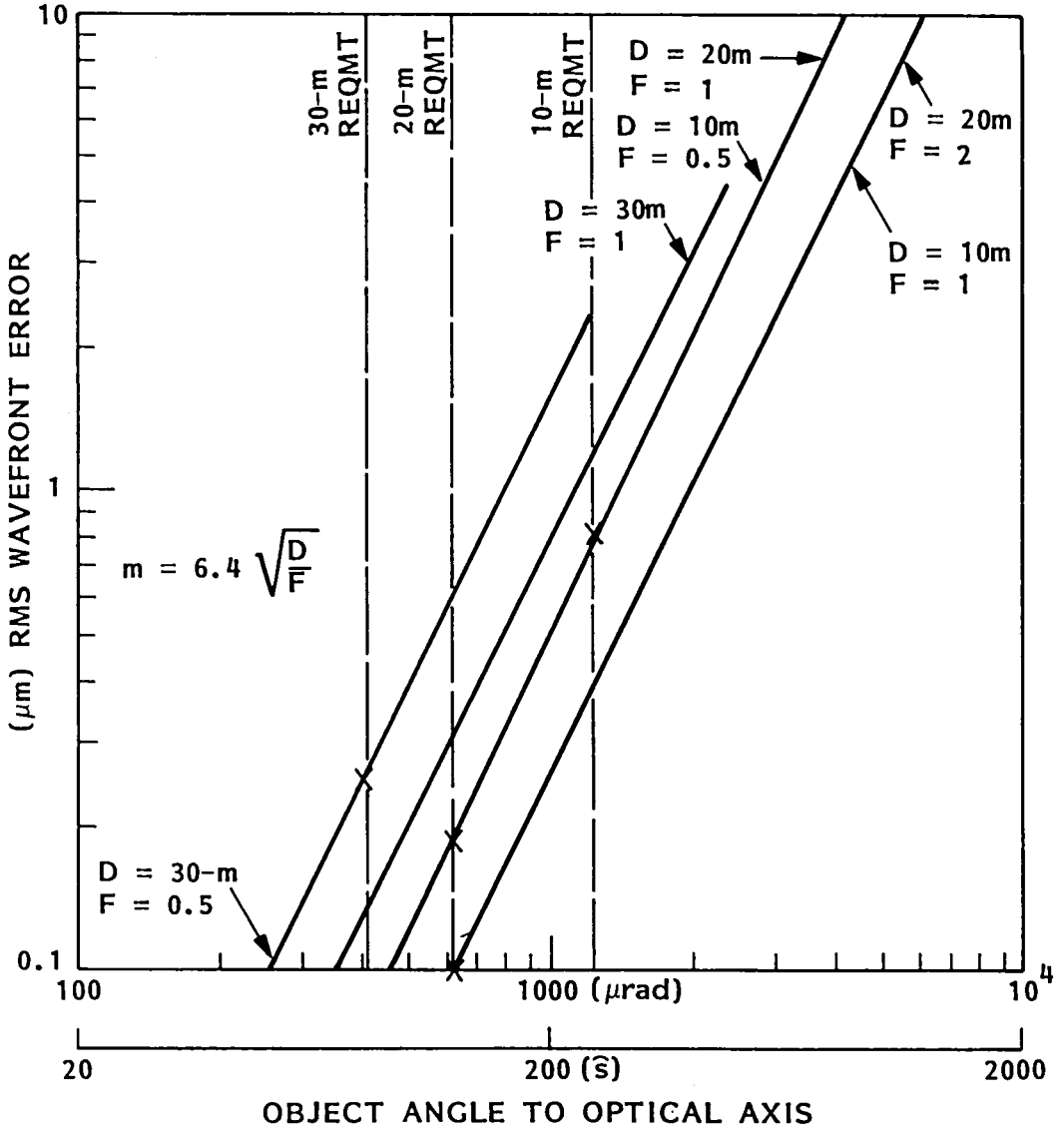

Fig. 4-2 Field Aberrations (Astigmatism) of the Parabolic Primary Two-Mirror Telescope (Best Focus)

4.5 SECONDARY MIRROR CHOPPING

Field-of-view scanning by oscillating the secondary mirror ("chopping") is a requirement for the LDR. We find that chopping at 10 Hz is feasible except at very short wavelengths ($\lambda < 30\ \mu m$) and for large secondary mirror diameters, where the performance is compromised and alternate scanning methods may be preferable.

Conceptually, the secondary mirror chopping technique has two possible problems. First, tilting the secondary mirror misaligns the telescope thereby increasing the telescope wavefront error. Second, the vibration of the rather large secondary distorts the primary mirror, the telescope structure, or the secondary itself. We first address the wavefront error issue.

If the secondary mirror is tilted by an angle β, then the change in the telescope look angle is

$$\Delta\alpha = \frac{2\beta}{m + 1} \cdot \tag{4.8}$$

Telescope misalignment from a secondary mirror tilt by an angle β about its vertex introduces a rms wavefront error of

$$\omega_c = \frac{D_s \beta}{96\ \sqrt{8}\lambda F^2} \tag{4.9}$$

waves, where a best-fit wavefront tilt has been removed. Substitution of Eq. (4.3) and (4.8) into (4.9) (to find the coma introduced from a change in look angle) yields

$$\omega_c = \frac{D\Delta\alpha}{192\ \sqrt{8}\lambda F^2} \tag{4.10}$$

For $\lambda > 100\ \mu m$ and a scan amplitude of 5 times the Airy disk diameter at the observation wavelength, Eq. (4.10) yields

$$\omega_c = 2.25 \times 10^{-2}/F^2, \tag{4.11}$$

Thus, even for F = 0.5, $\omega_c = 0.09$ rms waves, i.e., under the long-wavelength chopping conditions, the telescope performance is not compromised. For $\lambda < 100\ \mu m$, the scan amplitude requirement is

$$\Delta\alpha = \pm 75\ \mu rad \tag{4.12}$$

which gives at the maximum secondary misalignment,

$$\omega_c = \frac{1.38 \times 10^{-7}\ D/\lambda}{F^2} \tag{4.13}$$

Thus at F = 0.5, $\lambda = 30\ \mu m$, D = 30 m, we have $\omega_c = 0.55$ rms waves. In this case, the scan amplitude is ±31 diameters or about 6 times the number of Airy disk diameters required for $\lambda > 100\ \mu m$. Hence the requirements are not met at $\lambda < 100\ \mu m$ since the SOW-specified scan amplitude is so large that at the wavelength of observation, misalignment coma is unacceptable if the scan is accomplished by secondary tilt.

For a tilted aplanat, coma on-axis in the focal plane is zero even if the secondary mirror is tilted about the vertex. However, Table 4-1 shows that astigmatism is m/2 times as large as for a parabolic primary, no possibility of prime focus imagery exists, and the tilted apalanat has a considerable amount of fifth-order aberration. For these reasons, the system advantage inherent with the parabolic design should be retained and the SOW specifications be reexamined in the light of its system impact (i.e., elimination of an otherwise excellent telescope design form). Change of the specifications might be along the following lines:

(1) Reduce the scan amplitude to 5 times the Airy disk radius at the wavelength of observation. The impact of this specification relaxation on telescope utility is unknown.

(2) Let the secondary mirror oscillate between states of perfect alignment and misalignment by an angle 2β. If the sensor sees a uniform background during misalignment, telescope wavefront error will not significantly affect sensor accuracy. If the specification cannot be relaxed, FOV scanning may be accomplished by other methods than secondary tilt about its vertex, for example:

   (a) Reimage the primary mirror on an oscillating scan mirror. Although this approach requires additional reimaging optics (i.e., more optical elements), it does eliminate entrance pupil motion on the primary with its inherent scan noise. The beam path moves slightly across the secondary in this approach. However, since the secondary mirror is smaller and less exposed (or even cooled), the scan noise from this source should be relatively low.

   (b) Tilt the secondary mirror about the neutral point (which is located approximately at the secondary focus). This approach is more difficult to implement and is half as efficient as tilting about the vertex. However, secondary mirror tilts about the neutral point do not introduce third-order coma.

   (c) Increase the primary focal ratio from 0.5 to about 1.2. The telescope structure would be longer and focal plane and secondary size larger (with a subsequent increase in difficulties of secondary tilt implementation). However, Eq. (4.13) shows that coma would be reduced to acceptable levels at $\lambda = 30\ \mu m$. For $\lambda = 2\ \mu m$, the required focal ratio would be F = 4.6.

The second problem with secondary chopping is the mechanical and structural distortions due to the vibration of the secondary mirror. These distortions depend on the size and scan amplitude of the mirror and chopping frequency. Equation (4.7) provides an estimate of secondary mirror size. An estimate of scan angle, β, required to achieve FOV change of $\Delta\alpha$, is provided by Eqs. (4.6) and (4.8)

which yield

$$\beta = 3.2\sqrt{D/F}\ , \text{ D in meters} \qquad (4.9)$$

Below 100 m, $\Delta\alpha$ = 150 μrad (30 $\widehat{s}$). For an LDR of D = 20 m and F = 0.5, a secondary mirror diameter of 50 cm and scan angle of 3 mrad are appropriate. Satisfaction of such specifications is not a feasibility issue; it can be done. In fact, 50-Hz chopping mirrors are being constructed. LMSC reactionless motors of 60-cm diameter can oscillate over 4 mrad at 10 Hz.

Above 100 μm, $\Delta\alpha = 2.44\,\lambda/D$ (10 times beamwidth), for a maximum vertex tilt change of 25 mrad at λ = 1 mm. The implementation difficulties of the eightfold increase in scan angle have not been determined. Typically, such an increase can be obtained by relatively modest reduction in scan frequency (from 10 to 5 Hz). A detailed design study would determine whether the 25-mrad, 10-Hz, chopping specification could be met or whether the scan frequency must be lowered.

The effects of the vertex tilt changes from a 10-Hz scan on the figure to the 50-cm cored Be secondary mirror are shown in Fig. 4-3.

The cycle time of 0.1 s is divided into two periods of acceleration and two periods of staring. The scan efficiency is the staring interval divided by the total scan time; scan efficiency increases with mirror acceleration but so does mirror distortion. The scan efficiencies are shown in Fig. 4-3 for various constant torque drivers. The mirror acceleration unacceptably deforms the figure of the secondary mirror at short wavelengths ($\lambda < 10\mu$m). The figure shows how the applied torques must be reduced to keep secondary mirror figure error below $\lambda/20$ rms. This reduction in torque lessens the scan efficiency, as shown by the left-hand-side of the figure. At wavelengths longer than 100 μm, the FOV throw must increase from 30 $\widehat{s}$ (150 μrad) to 10 times the Airy disk diameter.

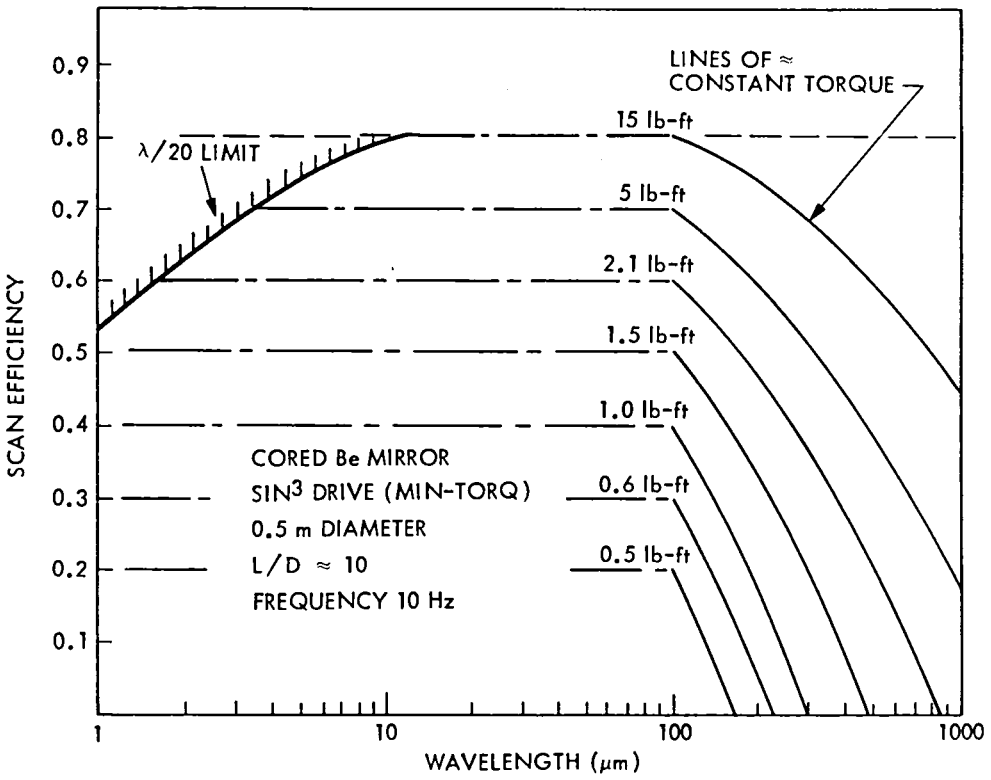

Fig. 4-3 Secondary Mirror Chopping

The given torque is insufficient to change the vertex tilt according to Eq. (4.9) in the allotted time. Therefore, the scan efficiency falls off as shown on the right-hand side of Fig. 4-3. Since the mirror deformation is small compared to the wavelength on the right side of the figure, scan efficiency may be restored simply by providing additonal torque.

To summarize, FOV scanning at 10 Hz seems feasible except that the permissible wavefront error may be exceeded for very short wavelengths and large diameters. Rather than let this problem drive the LDR optical configuration away from an otherwise excellent parabolic design, either the FOV specification chopping should be reexamined or the FOV scan should be accomplished by other techniques.

Section 5
ALIGNMENT AND POINTING

5.1 SUMMARY

The alignment tolerances of the LDR are specified and several fundamentally different approaches to alignment sensing are outlined and compared. Structural and thermal modeling of a 30-m-diameter LDR suggests that pointing performance is satisfactory and that active segment alignment is required to compensate for thermal distortion. Two sensing concepts for pointing stabilization are described.

5.2 REQUIREMENTS

Alignment of a telescope having a segmented primary requires that:

(1) Each primary mirror segment is correctly positioned to match the figure of the ideal large parabolic mirror
(2) The secondary mirror is correctly positioned on the optical axis of the best fit to the parabola formed by the segments

Each primary segment has six types of possible misalignment, shown in Fig. 5-1. They are: piston error, defined to be misalignment along the normal of the mirror segment center; in-plane displacement, the motion of the segment perpendicular to its center normal either in or perpendicular to the plane of incidence of the light on the segment; out-of-plane tilt, the rotation of the mirror about either one of the two above defined axes of lateral motion; and in-plane rotation about the segment normal.

The secondary mirror has only five misalignment sources since rotation about its optical axis does not introduce wavefront error. They are: longitudonal positioning error (despace); lateral positioning error (decenter) in two axes; and vertex tilt about two axes (Fig. 5-1).

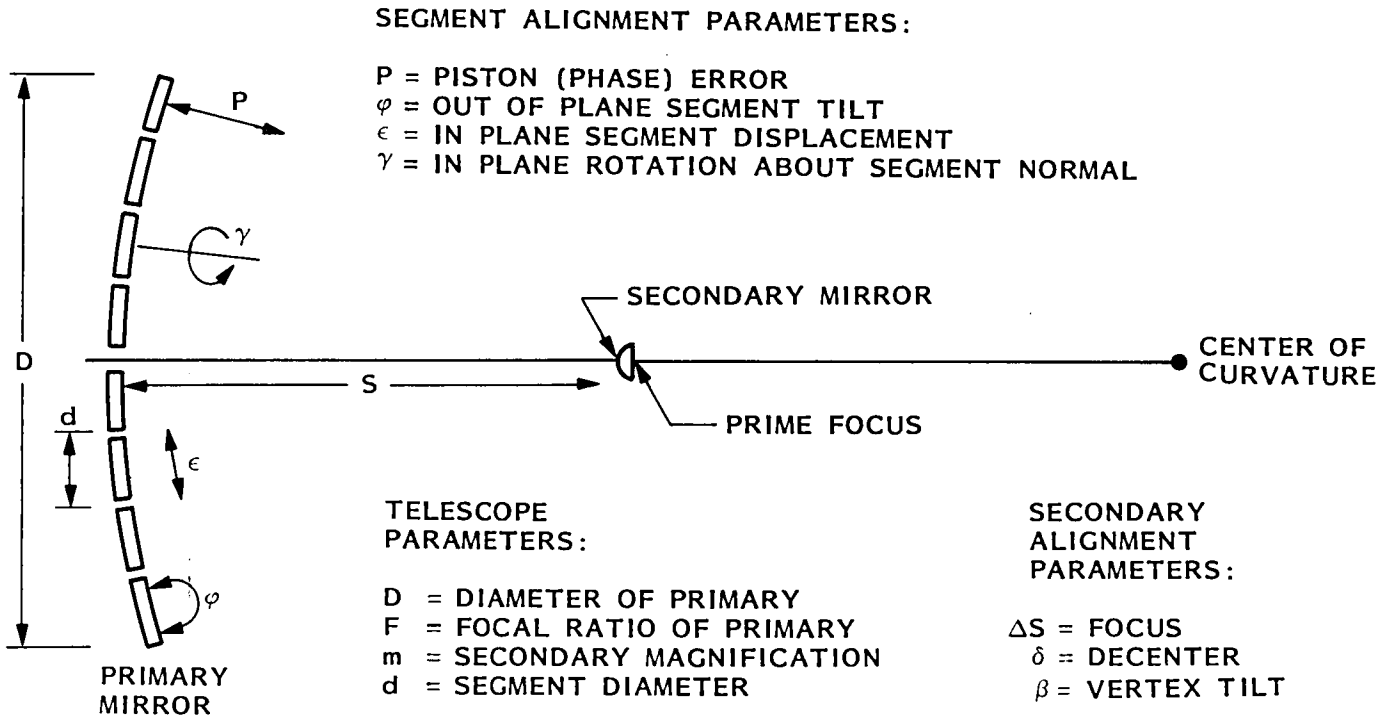

Fig. 5-1 Telescope Alignment Parameters

Table 5-1 gives estimates of telescope system rms wavefront error (best tilt removed) for a given rms misalignment. One type of misalignment may largely compensate for another; for example, secondary decenter and tilt which correspond to rotation about a point near the prime focus produce no third-order misalignment coma, an otherwise limiting aberration. Similarly, segment decenter and tilt which correspond to rotation about a point near the center of curvature will produce no segment wavefront tilt error.

The fact that segment decenter may be compensated for by tilt has important implications:

(1) Exact lateral positioning of the primary segments is not important (so long as they do not touch each other) since tilt actuation can compensate for lateral position error

(2) Alignment sensors (capacitive sensors, for example) which do not respond to rotation about the segment's respective centers of curvature are suitable for primary mirror alignment if they measure only mirror phasing

(3) Alignment sensors (such as the trilateration concept described below) which do require a measurement of segment rotation about their respective centers of curvature to determine segment phasing, must accurately measure segment decentration

5.3 ALIGNMENT TECHNIQUES

The various techniques of telescope alignment sensing are listed in Table 5-2 and are illustrated by Fig. 5-2. Segment alignment using a stellar wavefront is not included. Although this is an important technique for initial telescope alignment and calibration during observation, it must be supplemented by a totally onboard technique since a star of sufficient brightness need not be near the observation point.

Table 5-1

TELESCOPE ALIGNMENT PARAMETERS

	ALIGNMENT PARAMETER		ABERRATION	rms WAVES WFE EXPRESSION	PARAMETER VALUE FOR 1/100 WAVES rms*
SECONDARY	AXIAL MOTION	ΔS	FOCUS	$\frac{\Delta S}{16\sqrt{3}\,\lambda\,F^2}$	2.08 μm
SECONDARY	DECENTER	δ	IMAGE SHIFT; COMA	$\delta/96\sqrt{8}\,\lambda\,F^3$	10.2 μm
SECONDARY	VERTEX TILT	β	IMAGE SHIFT; COMA	$\frac{D\beta}{96\sqrt{8}\lambda F^2\,(m+1)}$	41 μrad
	PISTON ERROR	P	WAVEFRONT SEGMENT PHASE	$\frac{2P}{\lambda}$	0.15 μm
PRIMARY	OUT-OF-PLANE SEGMENT TILT	φ	WAVEFRONT SEGMENT TILT**	$\frac{d\varphi}{\sqrt{3}\lambda}$	0.13 μrad
PRIMARY	IN-PLANE SEGMENT DISPLACEMENT	ϵ	WAVEFRONT SEGMENT TILT**	$\frac{d\epsilon}{2\sqrt{3}\,DF\,\lambda}$	2.6 μm
PRIMARY	IN-PLANE SEGMENT ROTATION (PARABOLA)	γ	WAVEFRONT ERROR	$\frac{x^2\,d^2\gamma}{\sqrt{36}\,(x^2+R^2)^{3/2}\lambda}$	12.6 μrad

*This column is the evaluation of the parameters with the formulae in the preceding column set equal to 1/100 waves rms. Example parameters used in this evaluation are λ=30 μm, D=20 m, F=0.5, R= 2FD = 20 m x=10 m (location of segment) and segment diameter 4 m. It is intended to provide a feeling for the tolerances involved. All primary segments are assumed to be randomly misaligned in selected parameters.

**Combinations of segment tilt and displacement corresponding to rotation of segment about the center of curvature have second-order effect on wavefront error.

Table 5-2

TELESCOPE ALIGNMENT SENSING TECHNIQUES

	SENSOR CONCEPT	SENSOR TYPE	SENSOR LOCATION	ADDITIONAL SYSTEM REQUIREMENTS	ADVANTAGES	PROBLEMS
LOCAL	SEGMENT-TO-SEGMENT EDGE SENSING	CAPACITIVE SENSORS	AT TIPS OF HEXAGON	SENSORS BUILT INTO PRIMARY SEGMENTS	• NO ADDITIONAL SCATTERED LIGHT • SIMPLE SENSORS	• NOT ABSOLUTE SYSTEM • SEGMENT INSERTION • REQUIRES TELESCOPE ALIGNMENT SYSTEM • ERROR PROPAGATION • DEPENDS ON SEGMENT RIGIDITY
REMOTE	CENTER OF CURVATURE TEST	INTERFEROMETRIC OR RANGE MEASUREMENT	PRIMARY MIRROR CENTER OF CURVATURE	SENSOR SUPPORT STRUCTURE DOUBLES TELESCOPE LENGTH	• MOST ACCURATE • ONLY OUT-OF-PLANE SEGMENT ALIGNMENT ERROR NEED BE DETECTED	• NOT ABSOLUTE SYSTEM • LONG SENSOR SUPPORT • SCATTERED LIGHT
	SEGMENT ALIGNMENT FROM PRIME FOCUS	INTERFEROMETRY OR RANGE MEASUREMENT LATERAL POSITION SENSOR	ON SECONDARY OR PRIMARY (WITH REFLECTORS)	RETROREFLECTORS ON PRIMARY REFLECTORS ON SECONDARY PERIMETER	• ABSOLUTE SYSTEM • USED FOR POINTING	• SCATTERED LIGHT • RETROS ON PRIMARY • REDUCED SENSITIVITY FOR GIVEN SENSOR
	SEGMENT ALIGNMENT FROM BEHIND THE PRIMARY	RANGE AND LATERAL POSITION SENSOR	(1) CENTER OF PRIMARY (2) BEHIND EACH SEGMENT	THIN MIRROR SUPPORT STRUCTURE SENSOR BEHIND EACH SEGMENT	• ABSOLUTE SYSTEM • USED FOR POINTING	• COMPLEX • MEASUREMENT REQUIRES SEVERAL SENSORS

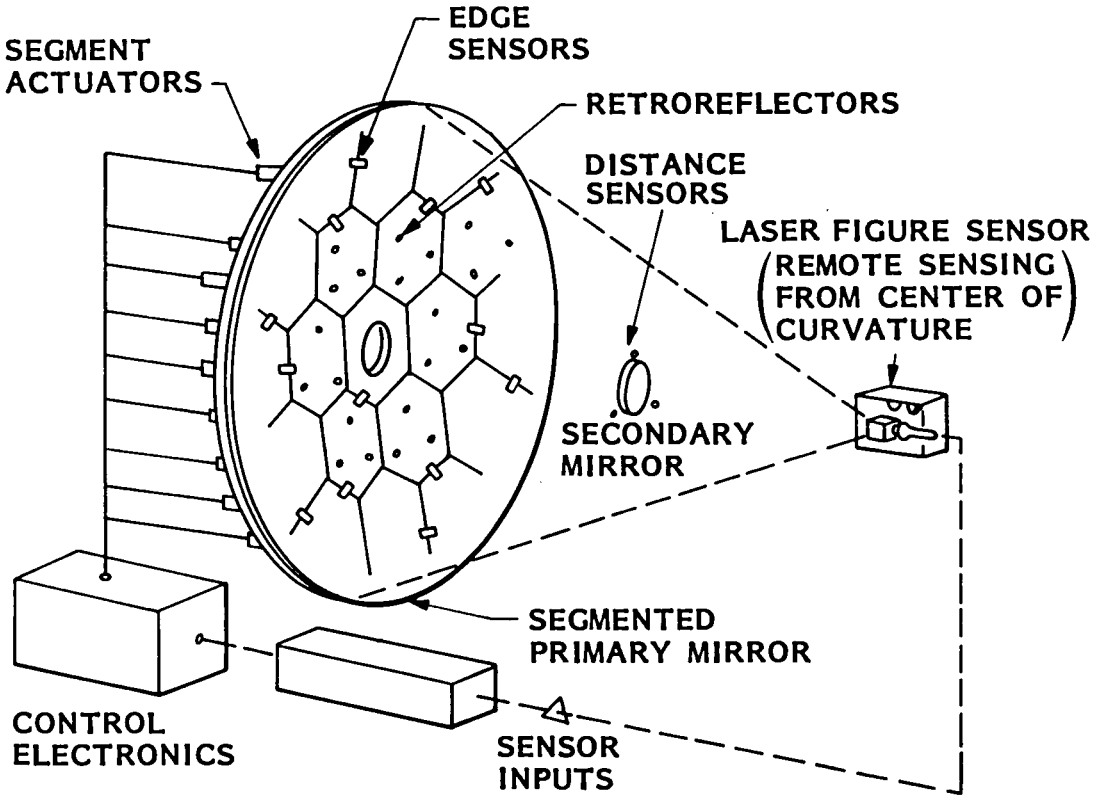

Fig. 5-2 LDR Alignment Measurement Concepts

Local alignment sensing techniques determine a segment's positon relative to its neighbors. By themselves, they determine the primary figure only and require an auxiliary system for primary-to-secondary alignment. An example of this type of sensor is segment-to-segment edge sensing done with capacitive edge sensors or equivalent edge monitoring interferometers. Since the wavefront is affected only by mirror misalignment normal to the mirror surface, out of plane surface continuity guarantees primary mirror figure if the figure of each individual segment is correct. As noted previously, in-plane segment position error has only a second-order effect if no surface discontinuities exists.

Remote alignment sensing techniques determine the segment's position relative to a central reference coordinate system - independently of the position of the neighboring segments, which may be in error. Furthermore, since the position of each segment and of the secondary mirror is known in the single reference coordinate system, the telescope look angle relative to the reference coordinate system

may also be deduced. If the orientation of this reference coordinate system relative to the stars is measured, it is possible to accurately point the telescope without use of a guide star in the telescope FOV.

Currently, the most promising remote telescope alignment concept is segment alignment from the vicinity of the prime focus, using a length measuring sensor whose source points are on the secondary mirror support structure. The concept (shown in Fig. 5-3) measures the range from three points near the secondary to at least three retroreflectors on each primary mirror segment. This is sufficient to determine the positions of each segment in the reference coordinate system. Center-of-curvature test and segment alignment from behind the primary are inferior sensing concepts. Center of curvature tests require a long supporting structure. The ensuing problems of deployment and effects on the telescope structure should be addressed only if other methods fail. Segment alignment from behind the primary employs a large number of separate and complex sensor packages. It appears too complex to compete with other options.

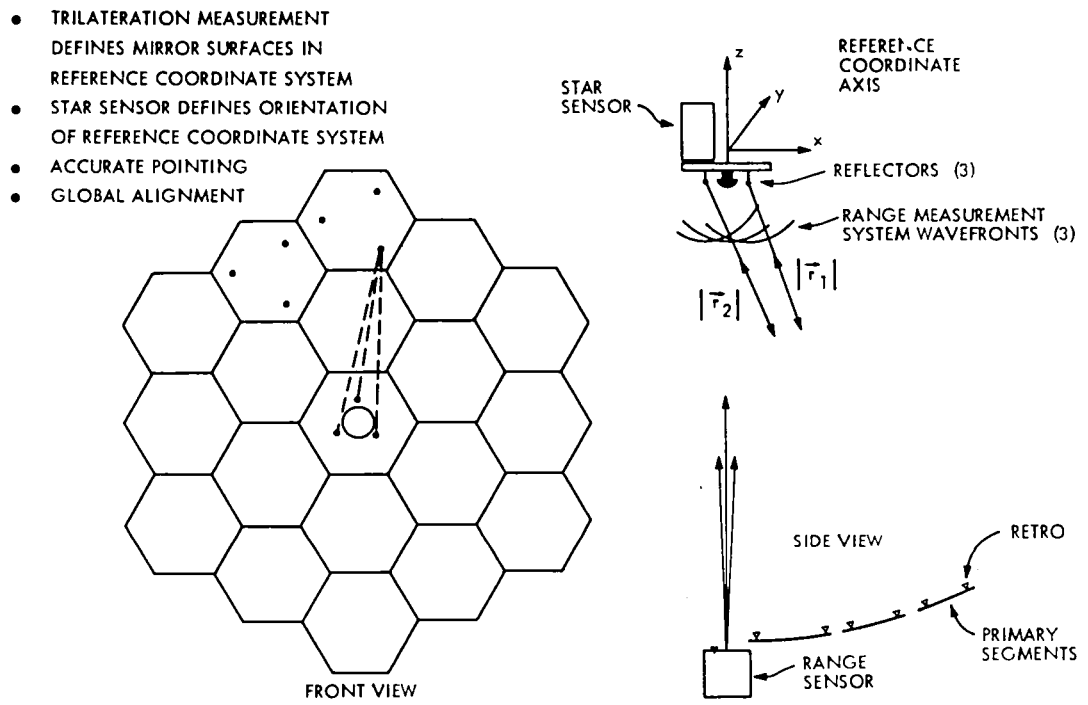

Fig. 5-3 Pointing and Alignment of Large Deployable Telescope

Comparing edge sensing and remote sensing, we recognize that both systems must be periodically calibrated using a bright star. However, the two methods are affected by time-varying figure errors in different ways.

In edge alignment, actuators maintain a set of sensor readings to values obtained during calibration. Since there is no absolute reference position, the error associated with misalignment and distortion of a single segment propagates to other segments. In additon, since edge sensing addresses primary figure only, the orientation of the primary mirror itself (required for primary-secondary alignment) is unknown and must be determined by a separate system.

Remote alignment, by contrast, maintains the alignment of each segment relative to an ideal coordinate system whose axis is known and can be used for primary-secondary alignment and telescope pointing.

Edge sensing as proposed for a 10-m ground-based telescope, uses capacitive sensors mounted on the segment edges (Ref. 1). These sensors sense out-of-plane motion of the segments. As applied to LDR, the first ring of hexagonal segments is aligned to the central reference segment, the second ring to the first ring, and so on. Since succeeding rings are aligned to an increasingly imperfect reference, the rms figure error increases with ring number or, equivalently, with mirror type. (Mirrors of different types have different figures.) The increase of mirror figure error with increasing number of types is shown on the left side of Fig. 5-4 (Fig. 10 of the reference). For example, a capacitive sensor error of 0.05 μm propagates so that with five mirror types the rms surface error of the outer mirror segment is 0.38 μm. The right-hand side of Fig. 5-4 shows the rms surface error over the entire mirror as a function of primary diameter (a 4-m segment diameter is assumed throughout).

The degradation factor, τ, is the rms surface error of the complete mirror divided by the sensor error. For a total mirror diameter of 25 m, the degradation factor is $\tau = 6$: the mirror surface error is six times the sensor error. The consequence of this error propagation is shown by Fig. 5-5. Since the edge sensor is attached to the mirror, which itself may be deformed, mirror figure

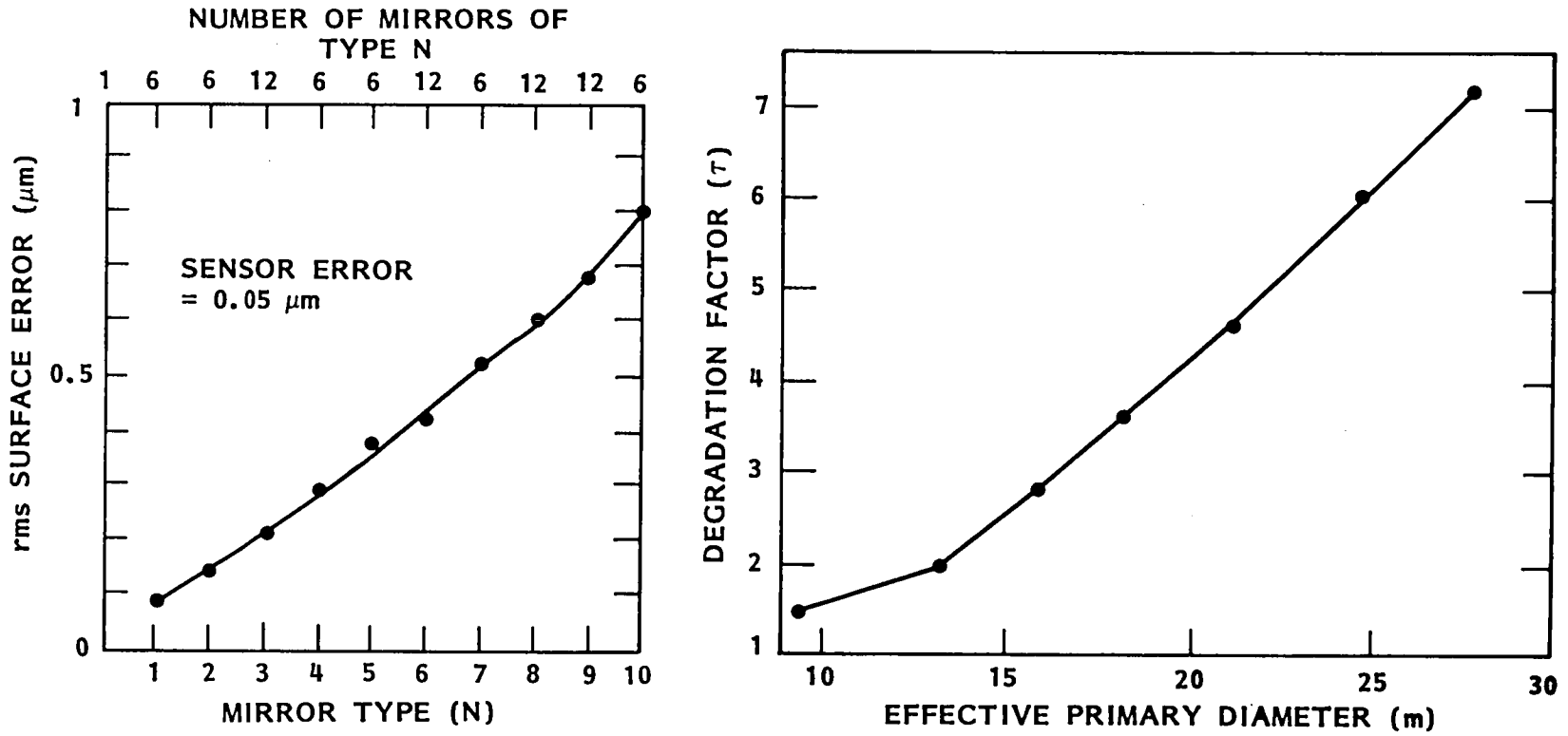

Fig. 5-4 Error Propagation in Edge Sensing

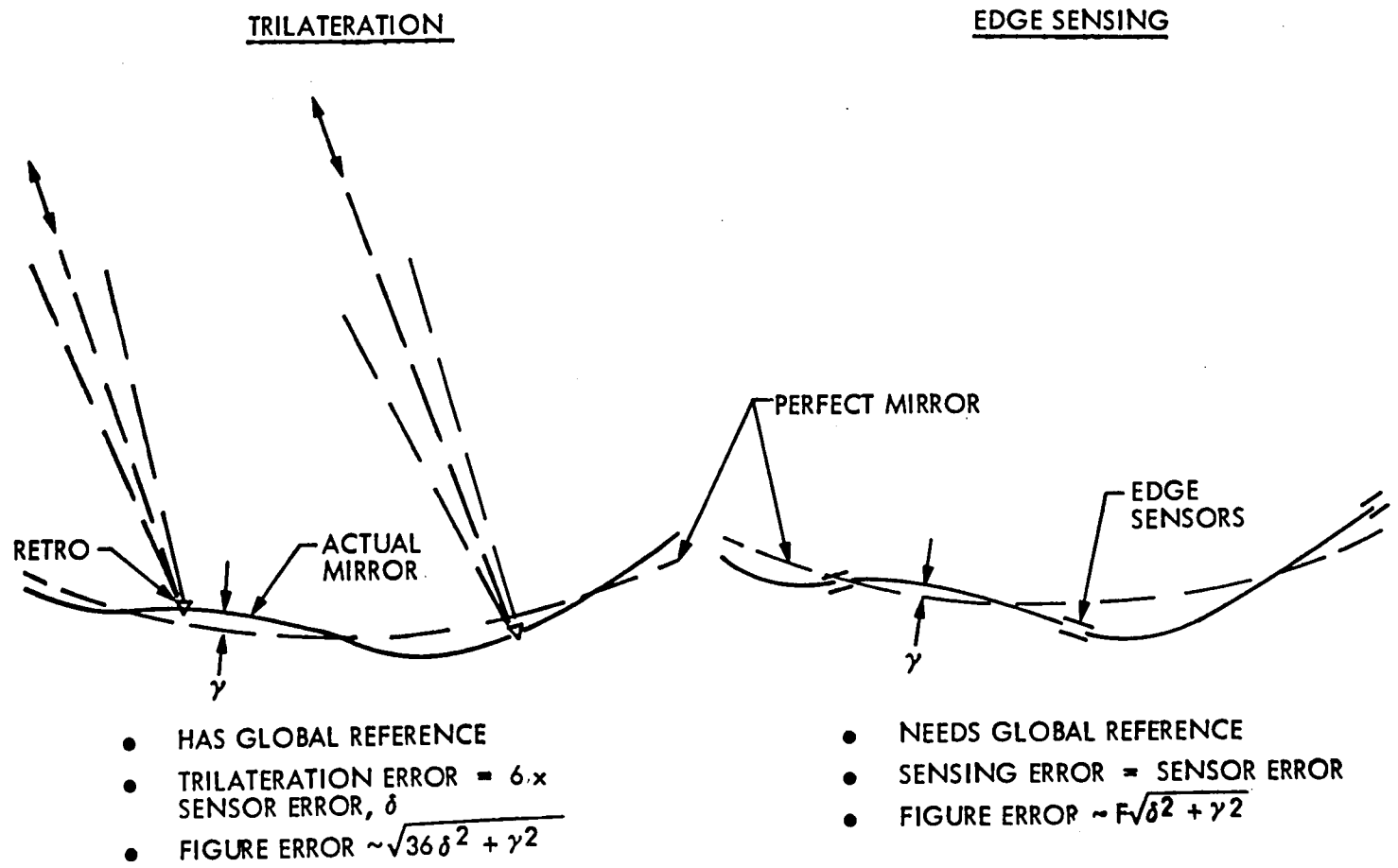

Fig. 5-5 Comparison of Trilateration and Edge Sensing

deviation from the ideal or the calibrated, γ, is averaged with the sensor error, δ, to yield an equivalent sensor error. The latter is then degraded by the factor τ to yield an estimate of the primary surface figure.

The trilateration system, because of sensor geometry discussed in Appendix C, measures the phase error of the segment retroreflector six times less accurately than the distance measurement error inherent in the sensor. This sensed phase error is averaged with the mirror figure variation, γ, as for the capacitive sensing system. However, since the error is measured relative to an absolute coordinate system, the degradation factor is unity. We therefore conclude that if the sensor error is smaller than the mirror figure error (likely to be true for the LDR but not necessarily for a ground-based telescope), the remote sensing system is superior to the local system, unless $\tau = 1$ for the edge sensing system. But $\tau = 1$ occurs only for a single ring of segments about a central mirror segment. Therefore, a mirror which has more than one ring should be aligned by trilateration if the sensor error, δ, is small compared to the mirror figure variation with time.

The sensor accuracy, δ, of both the capacitive sensor system ($\delta = 0.05\,\mu m$; see reference cited) and the range sensor system (Absolute Distance Interferometer, which can sense ranges to an accuracy of $\delta = 0.025\,\mu m$, Ref. 2) are much smaller than the unknown time varying figure errors of the mirror. (In LDR, δ is likely to approach $\lambda/10$ rms because of the weight and thickness constraints on the segments.) Therefore, the effect of the degradation factor is an extremely important consideration in the accuracy of the alignment sensor system. A telescope designed to work at 30 μm will be constructed with segments whose stability is equal to, say, 0.5- to 1- μm rms (an allowance for other error sources must be made). A 25-m LDR aligned by capacitive sensing would have $\tau = 6$, implying that each segment should be made six times more stable than would otherwise be required. Since thermal stability is likely to be the driving factor in the design of the mirror segments, such a stability requirement would impact the weight and thickness of the segments. These concerns may be summarized as follows:

(1) As the LDR telescope diameter increases, mirror segments are constrained by Shuttle requirements to become lighter and thinner, and the number of segments increases.
(2) The stability of mirror segments is the driving issue in mirror design and will probably limit the diffraction-limited wavelength of the LDR.
(3) Any more stringent requirements on segment stability, such as that resulting from capacitive sensing alignment, should be avoided since they will probably limit the maximum LDR diameter.

Reference to Table 5-2 shows that, exclusive of the issue just discussed, either capacitive sensing or trilateration has sufficient sensor accuracies to satisfy alignment requirements of a 30- μm telescope. The issue is one of convenient implementation. For a 2- μm telescope, however, sensing of mirror segment piston error would approach the limits of sensor technology.

One practical difficulty in the edge-sensing technque is that the sensors themselves must be deployed and aligned after the segments have been attached to the support truss. In trilateration, on the other hand, the segment reference points are permanently placed on the mirror. Their position may be sensed as soon as the remote sensor system is deployed.

The practical difficulty of trilateration is sensor complexity: a practical system requires a sufficiently compact and reliable sensor system which satisfies the system requirements of nearly simultaneous measurement of all reference points on the primary. LMSC has demonstrated several sensor concepts which have the required accuracy. The compactness and reliability issues await construction of a brassboard for their resolution.

5.4 STRUCTURAL RESPONSE TO INERTIAL AND THERMAL STRESS

To assess the behavior of the LDR under inertial and thermal stresses, a computer model of a D = 30 m, F = 0.5 telescope (the most stressing system) was constructed. The back structure supporting the mirror segments was assumed to be a tetrahedral truss with 3.46-m joint spacing (nodes at three of the corners of each 4-m segment),

the depth of the truss being 3 m. The truss legs were constructed of graphite/magnesium tubes. The weight budget of this telescope is given in Table 5-3.

Table 5-3
WEIGHT BUDGET FOR A 30-m LDR TELESCOPE

Backstructure	1470 kg
Secondary Tripod	90
Secondary and Associated Equipment	50
Primary Mirror	14140
Equipment Section	2400
Tripod Support Truss	3500
	21650 kg

Fig. 5-6 shows a computer-generated picture of the telescope. The equipment section lies at the node behind the primary center. The purpose of the truss structure behind the primary mirror tetrahedral truss is both to support the equipment section and to add stiffness to the secondary mirror support truss. The primary mirror was considered dead weight, not contributing to structural stiffness. The calculated structural resonant frequency is ~ 2 Hz. This relatively stiff structure easily satisfies the LDR slewing and pointing requirements from a structural viewpoint. The major structural uncertainties relate not to slewing and its associated vibrations, but to the constant vibration of the attitude control systems and the secondary mirror oscillations. A practical problem is that these vibrations, even though well isolated, could excite LDR structural resonances. A detailed modeling of these problems was not attempted in this study. However, some observations can be made.

A fixed vibration such as that produced by control moment gyros can be isolated from the structure far better than can the variable frequency vibrations of reaction wheels. Although reaction wheels are less expensive and are used in the Space Telescope, the relatively large size of the LDR and its susceptibility to vibrations argue for the fixed frequency vibration of the CMGs. This trade

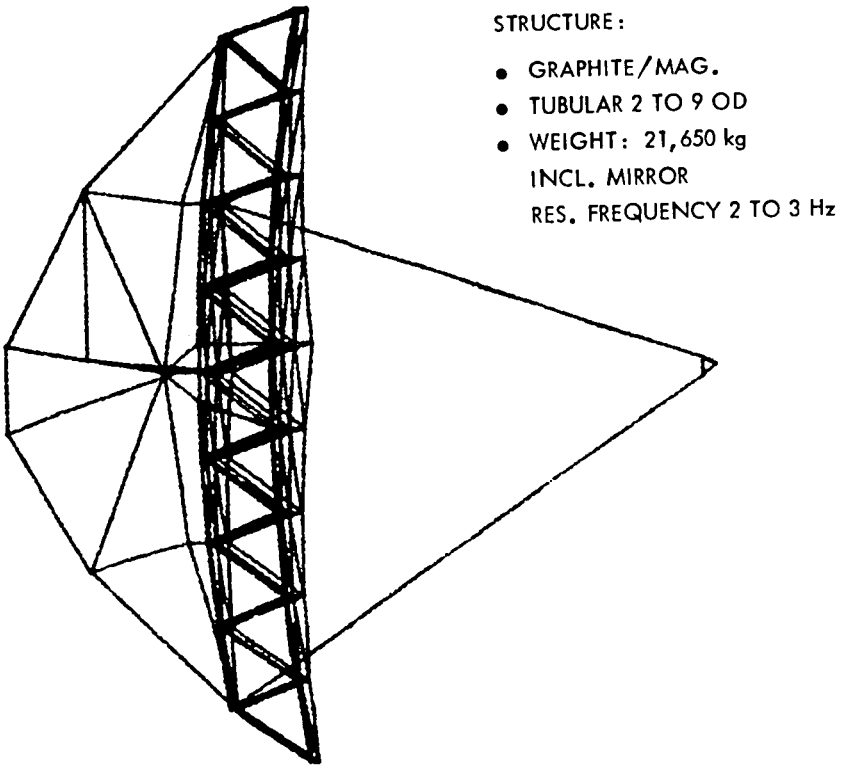

Fig. 5-6 30-m Diameter Tetrahedral Mirror Support Structure

and the effect of secondary chopping on the telescope structure should be addressed in further studies. It is our opinion that these two issues do not represent insurmountable problems.

A second purpose of the calculations was to estimate the thermal deformation by solar illumination of the primary mirror support truss and to determine whether real-time segment alignment is actually necessary. We found that a uniform temperature gradient of 20 °F across the truss depth would distort the mirror figure by 150- μm rms from a best-fit parabola of arbitrary tilt and vertex curvature unless the distortion was corrected by active segment alignment. (The same gradient plus an edge-to-edge gradient of 140 °F gave an rms surface distortion of 230 μm.) A gradient of 20 °F is probably attainable with good strut insulation and shielding. Clearly, operations at wavelengths below 1 mm require active segment alignment, or a sun shield. The selection of graphite

magnesium struts in this model is dictated by its excellent thermal stability. Aluminum struts are 100 times less stable and perform 100 times worse in the modeling. Graphite/epoxy is not quite as thermally stable; it also exhibits slow creep. Struts made of Gr/Mg will be available in the LDR time frame.

It is worthwhile to investigate real-time figure control of the segments. The figure actuators could be driven by error signals from a thermal model of the mirror segments with input data from thermal sensors in the mirror segments. While useful only for low-frequency error control such as segment curvature variations, the sytem might allow the use of very inexpensive segments, e.g., aluminum honeycomb (Ref. 3).

5.5 TELESCOPE POINTING

The telescope pointing commands could be derived by Space Telescope techniques, namely using a moderate accuracy control system to acquire guide stars near the desired observation point. The guide stars would then be used as a reference for telescope pointing stability.

On average, one 15th-magnitude star (or brighter) would be in the ≥ 3 $\widehat{\text{min}}$ FOV of the telescope. Since the LDR is diffraction limited at 30 μm, most of the energy of the star would be on the Airy disk calculated for $\lambda = 30$ μm. For a 10- to 30-m-diameter telescope, this Airy disk is 1.5 to 0.5 $\widehat{\text{s}}$. The pointing requirement will be satisfied if the stellar image in the LDR focal plane can be centroided to 1/25 of its 2.44 λ/D diameter - a requirement which is easily met.

Secondary chopping will move the guide star along with the rest of the FOV and complicate the pointing stability sensing. However, this should not affect the pointing feasibility as the extremes of guide star motion may be sensed and the pointing stability requirement in this situation can probably be relaxed. We noted earlier that secondary mirror tilt could be used to vary telescope look angles by ±5 beam widths with acceptable aberrations. Secondary mirror tilt

(or decenter) can therefore be used to compensate for small errors in pointing of the telescope axis; it is not necessary to point the entire telescope structure to accuracies and stabilities of 0.1 times the half-power beam width.

An alternative to pointing by guide stars exists. A small auxiliary telescope mounted behind the secondary (whose focal plane is precisely referenced to the alignment reference plane defined in the trilateration concept) could be used for precison pointing. Use of the alignment reference plane for precision pointing would require an increase of ~ 2 orders of magnitude in precison over that required for telescope alignment from wavefront error considerations. The trilateration technique could satisfy that requirement.

The 0.5-m-diameter auxiliary telescope would have a much wider FOV than the LDR itself and would therefore be able to use brighter guide stars. The telescope would be accurate at visible wavelengths so that the increase in Airy disk size due to the relatively small aperture would be offset by the decrease of disk size due to shorter wavelengths. Secondary chopping would, of course, not affect the guide star tracking.

5.6 CONCLUSIONS

Alignment tolerances of the LDR working at 30 μm can easily be met by existing sensors and control systems. A 2- μm LDR would require accuracies approaching the sensor limits. Trilateration (rather than edge sensing) for segment phasing is better suited to LDR diameters above 12 m.

Resonant frequencies of 2 Hz in a 30-m LDR structure ensure satisfaction of the modest pointing requirements. Isolation of the structure from broadband vibration sources (the attitude control system or secondary mirror oscillation) will prove to be a difficult but probably tractable problem.

Thermal stability of the graphite/magnesium primary mirror back structure is not sufficient to eliminate the requirement for active segment alignment. Thermal

stability requirements of the individual mirror segments may be reduced by use of a limited number of figure control actuators (segment figure control). This technique may allow the use of aluminum segments. The sensing and control problems for telescope pointing are easily solved.

5.7 REFERENCES

1. Terry S. Mast, Jerry E. Nelson, "Figure Control for a Segmented Telescope Mirror," Lawrence Berkeley Laboratories Report LBL-8621, 1979

2. C. W. Gillard, N. E. Buholz, and D. W. Ridder, "Absolute Distance Interferometry," Proc Soc. Photo-Opt Inst. Eng. Vol. 228, p. 70-77, 1980

3. D. M. Aspinwall and T. J. Karr, "Improved Figure Control With Edge Application of Forces and Moments," Proc, Soc. Photo-Opt. Inst. Eng., Vol. 228, p. 26-34, 1980

Section 6
MATERIALS

6.1 SUMMARY

Promising LDR primary mirror designs involve either solid beryllium or lightweight glass mirror segments supported on a graphite/magnesium structure. Aluminum segments (lightweight) can be used for near-mm wavelength observations. FRIT technology seems most promising for glass segments. Vacuum deposition for fabrication of solid Be segments requires extensive development.

6.2 REQUIREMENTS

It was established that the LDR primary mirror is likely to consist of rigid segments aligned on a support structure with a sensing-actuating control loop. Such a mirror has the generic structure shown in Fig. 6-1. As implied in this figure, the segment itself may have a complex structure consisting of solid face and back plates, separated by lightweight or solid sandwich material. The core material may or may not be the same as that of the plates. It is the purpose of this section to outline arguments for the choice of suitable materials and designs for the mirror segments and the support structure.

A major requirement for the primary LDR mirror is, in addition to low areal density (reflector mass/area ratio, m/A) and thinness (cf. Section 2), that its performance on-orbit, and certainly its structural integrity during launch, not be compromised. Important thermal and inertial stresses (loads) occur during the fabrication, handling, testing, assembling, launching, and in orbit. We distinguish between constant (dc) and time-varying (ac) loads. Some of these are listed in Table 6-1. We shall consider for detail study here only the dc loads listed in Table 6-1, in terms of basic constraints these make on material choices.

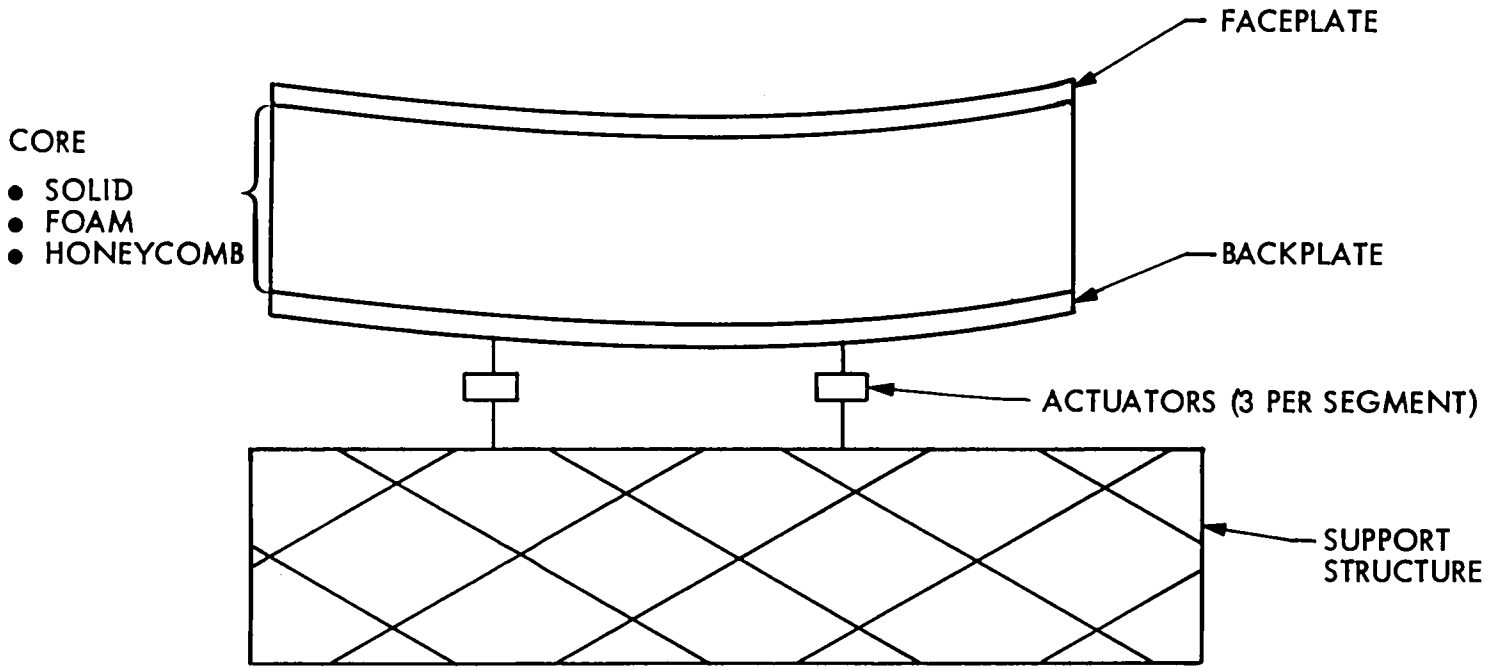

Fig. 6-1 Generic Mirror Structure

Table 6-1

MIRROR LOADS

	Constant loads (dc)	Varying loads (ac)
Thermal	Sun soak (60° incidence at 5% absorption)	Partial illumination (Orbital variation of illumination)
Dynamical	Average launch acceleration (4 g)	Launch acoustics (180 dB)
		Testing and handling; deploying
		Polishing

The ac loads are no less important than the dc loads, but cannot receive adequate treatment within the confines of this study. Their effect can also be minimized by proper design methods.

In the absence of a detailed mirror design – which must await further LDR concept development – we base our selection of suitable materials on general arguments about the desirable physical properties of such materials. These are: low density, ρ , high thermal conductivity, k, low linear expansion coefficient, α , high modulus, E, and high microyield strength, σ. Experience shows that for constant thermal and inertial loads, the compound ratios α/k, E/ρ , and E/ρ^3 are useful quality parameters for selecting materials. Their meaning is given in Table 6-2.

Table 6-2

MERIT PARAMETERS

Parameter	Maximizing the parameter minimizes the
α/k	thermal bending, for a constant given thermal flux
E/ρ	inertial bending, for a constant segment diameter
E/ρ^3	inertial bending, for a constant segment weight
σ	probability of fracture or permanent distortion

For our purpose, the parameter E/ρ^3 is more useful than E/ρ. This is because size and areal density of LDR mirror segments, and thereby the weight, are initial design parameters. They are determined by the Shuttle payload (mass and volume) limitations. This was discussed in Section 2. In effect, we want to determine which materials and designs for a fixed segment diameter of 4 m and fixed areal density respond least to the thermal and inertial dc loads in Table 6-1.

The merit parameters in Table 6-2 are derived from a simple model of the response of a mirror segment (assumed to be solid, for simplicity) to constant loads. In this model a segment is assumed to be circular and thin (large ratio diameter/thickness). If the diameter of the segment is d, total thickness h, then the maximum sag under constant acceleration parallel to the surface normal is

$$w_i = C_i(d^4/h^2)\ (\rho/E) \tag{6.1}$$

where the constant C_i depends on the segment support geometry. The segment mass is

$$m = (\pi/4)\,\rho d^2 h = Ah\rho \tag{6.2}$$

where A is the plate area. Hence

$$w_i = \text{constant}\ (A^4/m^2)\ (\rho^3/E) \tag{6.3}$$

Thus among segments with the same mass and area, and therefore same diameter and areal density, those with the largest value of E/ρ^3 will bend least.

The thermal bending of the same segment under a constant heat load (steady sun soak) q, is

$$w_t = C_t\ qd^2\ (\alpha/k) \tag{6.4}$$

Hence those segments which have the highest value of k/α will bend least.

Table 6-3 lists various materials in the order of decreasing value of the compound merit parameter $(k/\alpha)\ (E/\rho^3)^{1/2}$. This parameter is the single most appropriate quality parameter on which we can base our material selection. (The square root in the parameter is for convenience of units.) In the table we have distinguished between support structure materials and segment materials. The first cannot be used for plate construction, i.e., manufactured with the necessary surface quality, while the latter can. The table also gives values of other quality parameters. Figure 6-2 has the same materials marked in a diagram of (k/α) versus $\sqrt{E/\rho^3}$. Both table and figure clearly show that the metal-matrix materials are superior structural materials, and among these, graphite/magnesium is outstanding. BeO, Be, and the low expansion glasses/ceramics (in the following simply classified as glasses) are superior segment materials.

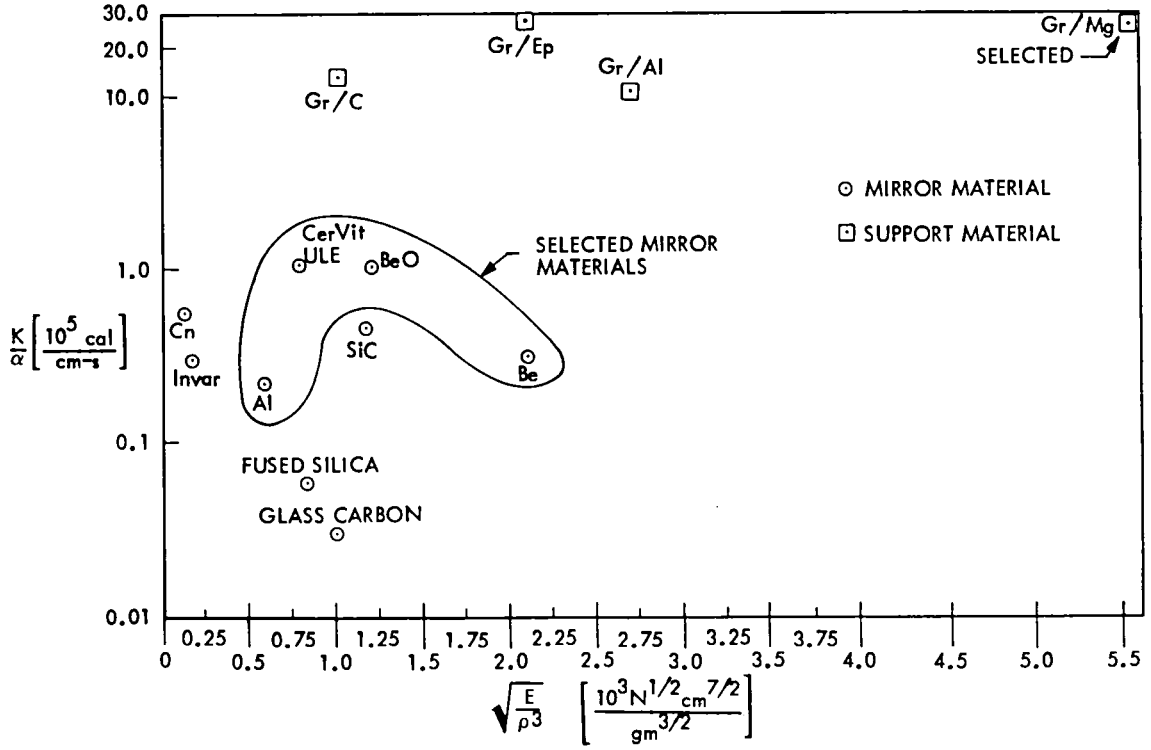

Fig. 6-2 Comparison of Candidate Materials (300° K)

Table 6-3

MATERIAL FIGURES OF MERIT

Material	k/α	E/ρ	$Ek/\alpha\rho$	$(E/\rho^3)^{1/2}$	$(k/\alpha)\ (E/\rho^3)^{1/2}$
		A. Segment Materials			
Beryllium-Oxide	1.05	12.1	1.27	1.2	1.26
ULE	1.03	3.1	0.31	0.79	0.814
Cer-Vit	1.03	3.7	0.31	0.79	0.814
Beryllium	0.303	0.5	0.45	2.09	0.633
Silicon Carbide	0.45	13	0.59	1.17	0.526
Aluminum	0.22	2.6	0.058	0.59	0.13
Copper	0.56	1.24	0.07	0.125	0.07
Invar	0.3	1.8	0.054	0.167	0.05
Fused Silica	0.059	3.36	0.0196	0.833	0.048
Glassy Carbon	0.033	2.3	0.0076	1.0	0.033
		B. Support Structure Materials*			
Graphite/Magnesium	30.3	18.57	56	5.56	168.5
Graphite/epoxy	25	12	30	2.11	52.75
Graphite/Al	10.1	14.3	14.44	2.70	27.3
Graphite/Carbon	13.2	3.23	4.28	1.0	13.2

k/α in 10^5 cal/cm.s; E/ρ in 10^{11} cm^2/s^2; $Ek/\alpha\rho$ in 10^{14} cal/s; $(E/\rho^3)^{1/2}$ in 10^3 $N^{1/2}$ $cm^{7/2}$ $gm^{-3/2}$

*Along direction of fibres.

These, as well as aluminum, are selected for further consideration. Aluminum is included in this selection, although it is inferior to SiC, because it is a very inexpensive material, well known in terms of its handling and fabrication characteristics, and was successfully used in the Cal Tech 10-m segmented ground reflectors.

6.3 SEGMENT CONSTRUCTION

The simplest segment structure is a solid plate, the next simplest being that in which the same material is used for faceplate, backplate, and core, with the plates having the same thickness, t (the total segment thickness being h). To see which of the selected materials lend themselves to solid rather than sandwich, or lightweight, construction, we investigated how the deflection under constant thermal and inertial loads varies with the ratio t/h for a given segment thickness, h. This ratio is, in effect, a measure of the degree of lightweighting.

The center sag of a thin circular lightweight segment of diameter d, mass m, plate area A ($=\pi d^2/4$), when continuously supported around the rim and under a constant heat load (absorbed heat flux) q, is approximately

$$w_t = \frac{q\, d^2 \alpha}{48\, k\, (t/h)} \left\{ 1 + \frac{1 - (m/A)\,(1/h)}{(m/a)\,(1/\rho h) - 2(t/h)} \left[1 + 6t^2/h^2 + 4t^3/h^3 \right] \right\} \quad (6.5)$$

In Eq. (6.5), α, ρ, and k refer to the (bulk) material, not to averages over the segment. For a given material and given areal density, the sag thus depends on h and on (t/h). Over the respective ranges of h and (t/h) for which the equation holds – the range is determined by m/A and by the thin plate assumption, which limits t/h to values less than about 0.1 – two properties of w_t become apparent: (The trends are typical for all materials studied, but only the example of ULE at 300 K operating temperature is discussed here). As Fig. 6-3 shows, these properties are:

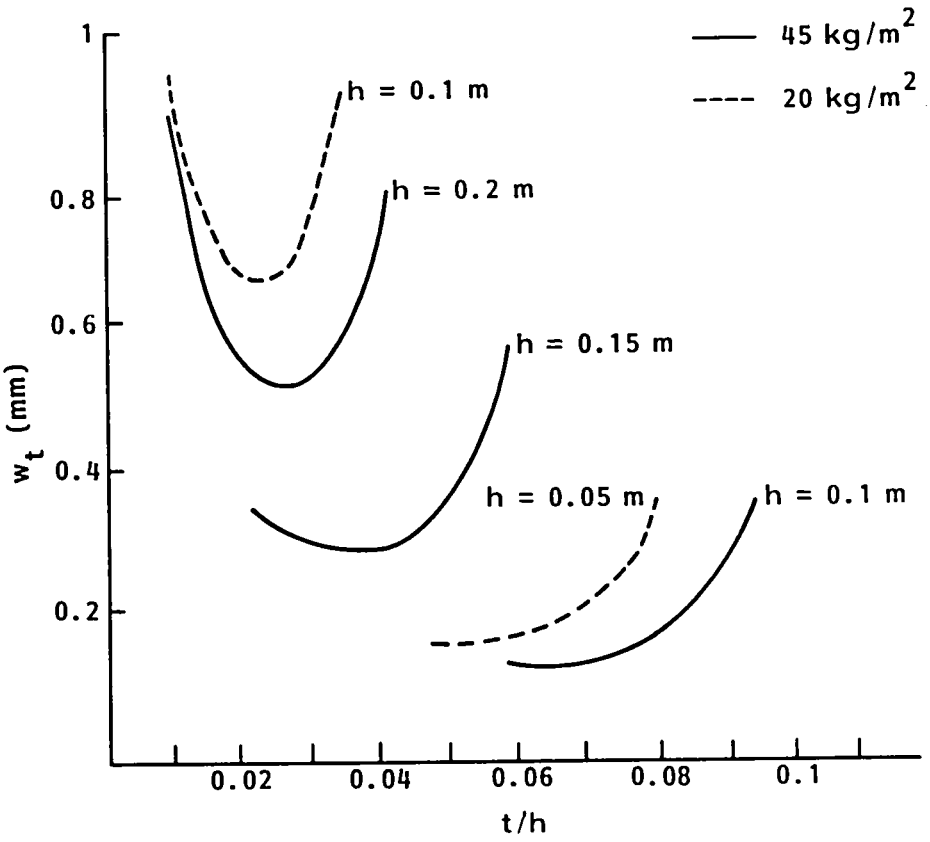

Fig. 6-3 Maximum Thermal Deflection of 4-m-Diameter ULE Segment Under Constant Heat Load 37.5 W/m^2

- For a given segment thickness h, there is an optimum value of (t/h), for which the deflection w_t is a minimum. This means there is a "best" lightweighting. Physically, this result is due to the fact that whereas the flexural rigidity decreases with increasing value of (t/h), the thermally induced bending moment increases, and w_t is proportional to (moment/rigidity). Competition between these trends produces the minimum.
- For a constant ratio t/h, the deflection is smaller for h. In other words, solid segments of a given areal density retain their figure under constant thermal load better than lightweight ones, and thin lightweight ones

better than thick lightweight ones. In this case, the physical explanation is that increasing the thickness h increases the resistance of the segment to the heat flow perpendicular to the plates through the core, and the thermal moment increases faster than the flexural regidity. (No lateral heat flow is assumed in this model nor heat transfer by radiation; in future studies this model must be improved.)

Within the limits of the accuracy of the model we therefore conclude that LDR segments should be, either solid or thin, lightweight. The conclusion plays into the hands of the requirement that the segments be thin for maximum storage capability in the Shuttle bay.

The deformation of the same segments during launch increases with decreasing thickness. The trend is evident from the inertial deflection under constant acceleration

$$w_t \propto \frac{md^2}{Eh^3 (t/h)} \tag{6.6}$$

which monotonically increases with decreasing value of t. This trend provides a lower practical limit to the segment thickness. During the acceleration, segments must not be permanently bent. We set an upper limit to the bending stress at 10% of the microyield stress. Calculating the required thickness of solid segments and comparing it with the actual thickness, we find (Table 6-4) that only beryllium segments can be solid at areal densities as low as 45 and 20 kg/m^2 - corresponding to a maximum reflector diameter of 24 and 20 m, respectively. The implication of this result is that for very large reflectors, materials other than beryllium must be lightweight.

Table 6-4

THICKNESS OF 4-m DIAMETER, SOLID MIRROR SEGMENTS

Material	Actual thickness (mm) for areal density (kg/m^2)		Required thickness (mm)
	45	20	
BeO	16	6.7	30
ULE	20	9.1	60
Be	25	12	12
Al	17	7.4	48

6.4 SEGMENT BASELINE CONCEPTS

We shall derive baseline concepts for LDR mirror segments using the materials selected earlier. Discussion of more complex segments, for example those using several diffferent materials, will be taken up in the next section.

The primary mirror must be diffraction-limited at the working wavelength λ. This requires, as a minimum condition, that for worst sun soak the thermal distortion of a segment, when translated into an rms figure error, be less than $\lambda/20$. The distortion depends on operating temperature for many materials. A typical operating temperature for LDR is assumed to be 200 K, although no detailed calculations were made to establish what temperature may be maintained by passive means. Past experience with passive systems, though not as large as LDR, indicates 200 K to be a reasonable value. The segment diameter is 4 m. As discussed earlier, the distortion given by w_t in Eq. (6.5) has a minimum value as a function of (t/h), for a given value of h, and that minimum decreases with decreasing value of h (Fig. 6-3). A lower practical limit to h is given by the requirement that the lowest vibration modes of the segment excitable during on-orbit operations be sufficiently high. Thus, a minimum stiffness is required in addition to the survivability under the launch acceleration, which was discussed earlier. Best engineering judgement sets the lowest practical value of h to a

value where the minimum of w_t as a function of (t/h) in Fig. 6-5 approaches within 25% the asymptotic value.

The limiting operational wavelength, λ_{limit}, is then calculated from that lowest value of w_t, namely w_{limit} by

$$\lambda_{limit} = \frac{10\, w_{limit}}{\sqrt{12}} \qquad (6.7)$$

Results of the calculations are given in Table 6-5. Note that for the solid segments the value of h is, of course, fixed by the m/A ratio. It follows from these results that only the glasses and Be can operated down to the required wavelength of 30 μm without on-orbit adjustment of the segment figure. Aluminum mirrors are limited to operation above about 500 μm. The glasses, with a suitable composition (TiO content for ULE and CerVit), can in fact operate to below 2 μm without figure control; 2 μm is a desirable but not a required operational goal for LDR. BeO performs better than Al but its potential for large segment fabrication is, at this point, rather uncertain, since the physical and handling characteristics are not well known. Beryllium is expensive as a raw material (12 times that of the glasses), requires facilities for manufacturing large plates and has problems of uniformity, creep, and crystal line slippage. Properties of the lightweight glasses are well understood and fabrication methods advanced. New promising lightweight techniques for the glasses are discussed in the following section and also in the enclosed essay by Kodak Co. (Appendix D).

In summary, we have three baseline concepts for LDR segments: (1) solid beryllium, for operations to 30 μm; (2) lightweight glass, also for operations to 30 μm; and (3) lightweight Al or BeO, for operations down to about 0.5 mm.

6.5 FABRICATION TECHNIQUES

Conventional fabrication of lightweight glass mirrors (Space Telescope technology) involves fusion welding of a honeycomb core to a faceplate and a backplate and

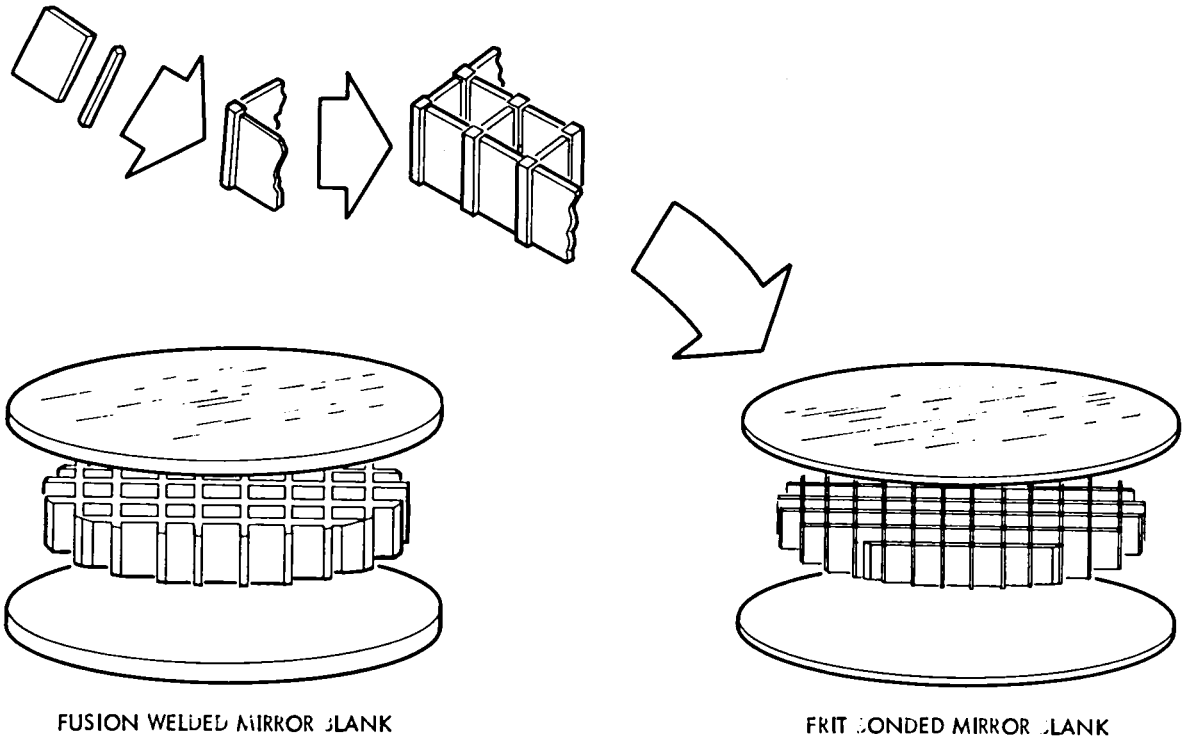

Fig. 6-4 Glass Mirror Fabrication Processes

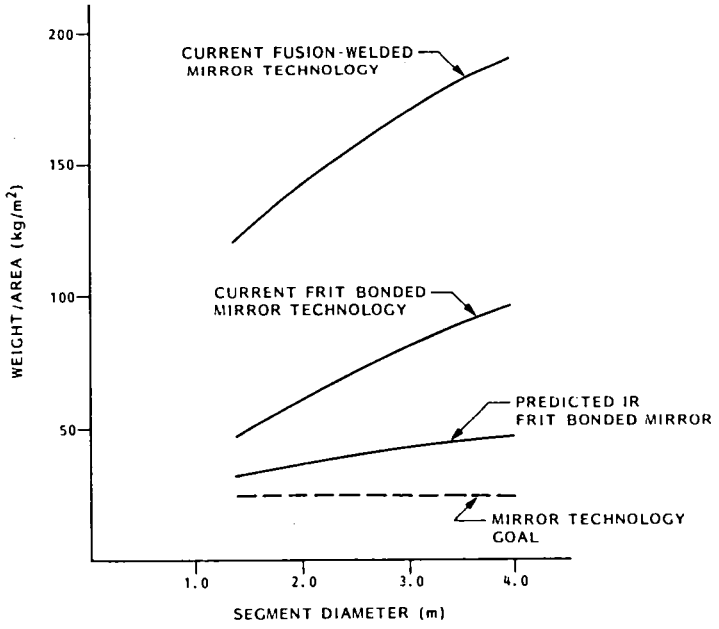

Fig. 6-5 Predicted Mirror Weight/Area for Glass Mirrors

Table 6-5

PERFORMANCE OF 4-m DIAMETER SEGMENTS

MATERIAL	TOTAL MIRROR THICKNESS (cm)	WAVELENGTH AT WHICH $\lambda/20$ rms WAVEFRONT ERROR EXISTS FOR THERMAL DEFORMATION (37.5 W/m^2 ABSORBED FLUX)	SOLID/LTWT 4g LAUNCH, 10 x YIELD/RUPTURE
ULE (7% TiO) (300 K) 20 kg/m^2	10	462 μm	ITWT
45 kg/m^2	10	87 μm	ITWT
ULE (7% TiO) (200 K) 20 kg/m^2	10	694 μm	ITWT
45 kg/m^2	10	376 μm	ITWT
ULE (4.5% TiO) (200 K) 20 kg/m^2	10	$\approx$0 (μm ROUGH LIMITED)	ITWT
45 kg/m^2	10	$\approx$0 (μm ROUGH LIMITED)	ITWT
CERVIT 20 kg/m^2	5	$\approx$0 (μm ROUGH LIMITED)	ITWT
45 kg/m^2	2	$\approx$0 (μm ROUGH LIMITED)	SOLID
FUSED QUARTZ (200 K) 20 kg/m^2	5	664 μm	ITWT
45 kg/m^2	2.1	13 μm	SOLID
GLASSY CARBON (300 K) 20 kg/m^2	1.33	77 μm	SOLID
45 kg/m^2	3	77 μm	SOLID
Be (300 K) 20 kg/m^2	1.2	6.6 μm	SOLID
45 kg/m^2	2.5	6.6 μm	SOLID
Be (200 K) 20 kg/m^2	1.2	0.65 μm	SOLID
45 kg/m^2	2.5	0.65 μm	SOLID
Be O (200 K) 20 kg/m^2	10	329 μm	ITWT
45 kg/m^2	10	64 μm	ITWT
CARBON/CARBON 20 kg/m^2	10	N/A	ITWT
45 kg/m^2	3.2	0.68 μm	SOLID
A1 20 kg/m^2	5	578 μm	ITWT
45 kg/m^2	10	462 μm	ITWT

then slumping the aggregate over a form to the desired shape. This technique limits the areal density of a 4-m segment to about 200 kg/m^2, for reasons discussed in Appendix D. A new fabrication method, FRIT bonding, uses a bonding agent to assemble individual parts to the structure (Fig. 6-4). The bonding agent sets at a temperature considerably lower than those at which the structure would be thermally deformed. Hence, thinner and more lightweight mirror segments are possible with this technque than with fusion welding. The technique is still developing, and it is likely that the areal density of 25 kg/m^2 required for a 30-m diameter LDR will be achieved (cf. Appendix D).

Promising fabrication methods for solid mirrors (i.e., also for the face sheets of lightweight ones) are vapor deposition, slip casting and slumping, and hot press and sinter. They are illustrated in Fig. 6-6.

Vapor deposition (chemical, physical, and ion) was developed for making thin films with precision molds but has been adapted to making free-standing (i.e., rigid) structures. The deposition rate can be varied, and also the composition of the deposited material, to produce optical quality surfaces without polishing or grinding. These two processes - polishing and grinding - can consume a large fraction of the total manufacturing time for mirrors. Current vapor deposition facilities, however, are not large enough to handle large (i.e., 4-m-diameter) segments, and substantial investment in development is required. Vapor deposition is possible with all three of the preferred LDR segment materials. Homogeneity is critical. If grain orientation is important, a deposit may be grown epitaxially. The advantage is precise control of the composition as well as excellent surface accuracy. A disadvantage is that a high vaccum is required, the substrate must be maintained at a high temperature, and the deposition rate is relatively low.

Slip casting and slumping is possible with several materials. LMSC has developed a slurry technique, in which ground ULE is cast into egg-crated forms, resulting in a structure with nearly the same thermal properties as ULE. The method

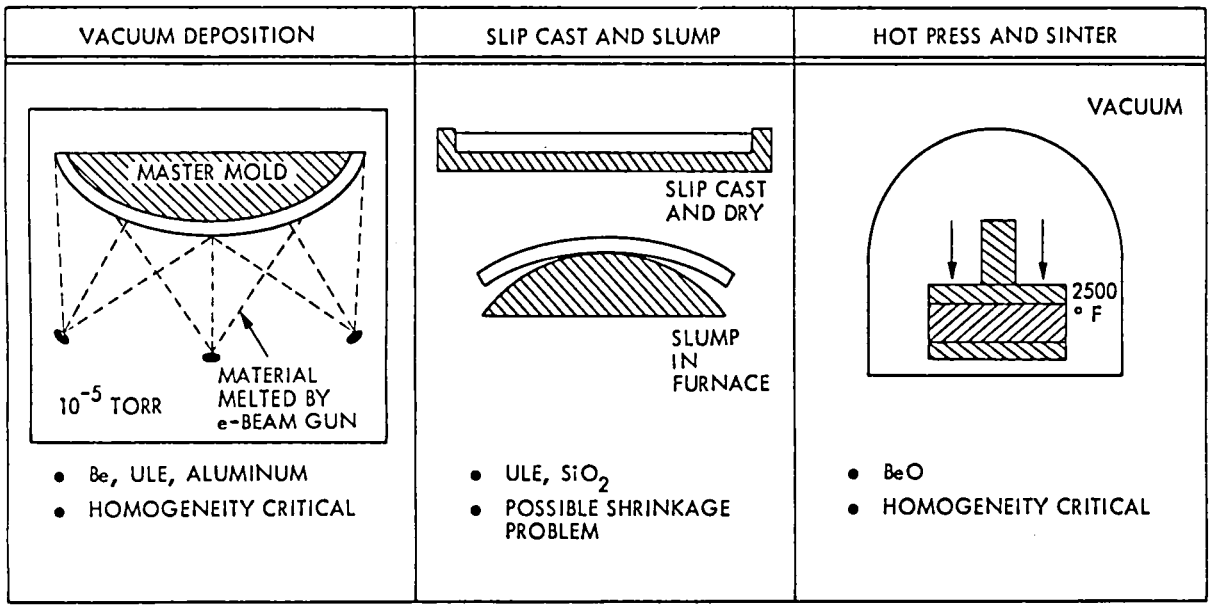

Fig. 6-6 Fabrication of 4-m Solid Mirrors

provides maximum utilization of the raw material - not possible with conventional techniques. A possible segment design is shown in Fig. 6-7. The area density is 24 kg/m^2.

Slumping has been successfuly carried out for solid as well as lightweight segments made of ULE or fused silica. Continuous cores allow the face sheet to be polished at a higher pressure than egg-crated cores, with a consequently lower polishing time. Slumping is a risky process, and in some cases machining the core to shape rather than slumping may be preferable.

Several promising designs for mirror segments using different materials for plate and core (and possibly several different materials in the core itself) are in development at LMSC and elsewhere. As an example, we mention here the concept by General Dynamics Co. (Convair Division). It has a composite base layer which as a 5-dimension carbon fiber weave impregnated with a resin that is

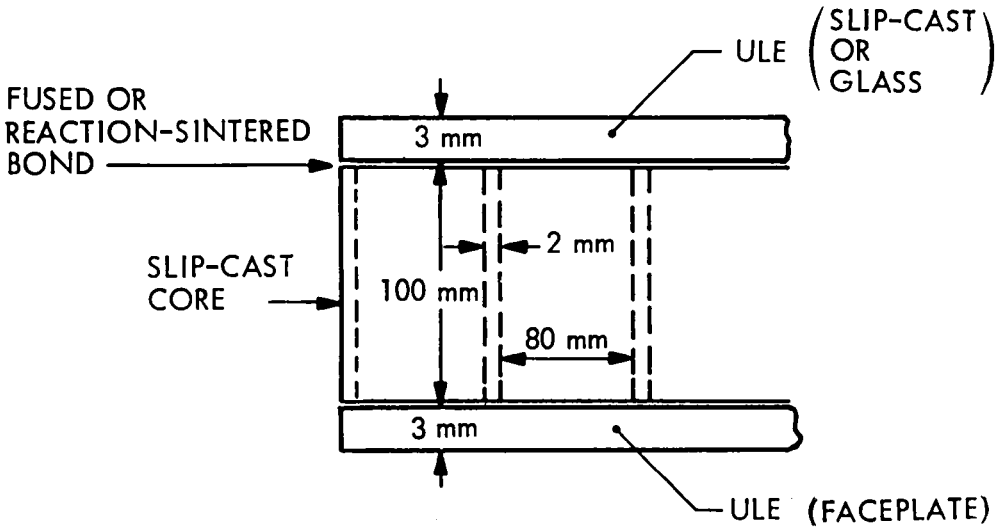

Fig. 6-7 LMSC Slip-Cast ULE Mirror Design Concept

carbonized in a furnace. Above it is a 1-mil amorphous graphite layer, a 1-mil Si layer, and finally, a ULE face sheet. Current samples are, however, small (25-cm diameter) and suffer still from carbon fiber print-through. The areal density is 22 kg/m^2 (Fig. 6-8).

6.6 CONCLUSION

Several materials and fabrication methods exist for making segments and mirror support structures which satisfy the LDR requirements for stiffness and performance. The mirror support structure will be made of graphite/magnesium, and the segments of either solid beryllium sheets, or of lightweight glass. Aluminum (Hexcel) mirrors may be adequate for a small (10-m-diameter) passive mirror working at near-millimeter wavelengths. As a raw material, it is inexpensive and easily machined. Low-expansion glasses and ceramics are expensive and require

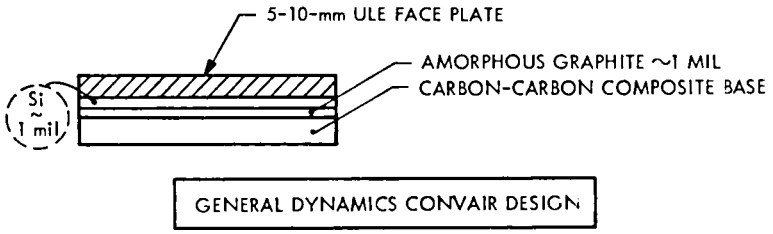

- PURPOSE OF DARPA PROGRAM IS TO DEMONSTRATE LARGEST NONADAPTIVE MIRROR SEGMENT POSSIBLE
- ALSO DEMONSTRATE STABILITY OF GRAPHITE CARBON COMPOSITE MATERIAL
- CURRENT DESIGN SUFFERS SOMEWHAT FROM CARBON FIBER PRINT-THROUGH ONTO MIRROR SURFACE
- $\gtrsim$ 0.25-m DIAMETER HAS BEEN DEMONSTRATED
- 22 kg/m^2 AREAL DENSITY, CTE ONLY 2X THAT OF ULE's, CONDUCTIVITY SUPERIOR TO ALUMINUMS
- CARBON-CARBON COMPOSITE BASE IS A 5-DIMENSIONAL CARBON FIBER WEAVE IMPREGNATED WITH A RESIN THAT IS CARBONIZED IN A FURNACE

Fig. 6-8 General Dynamics Lightweight Carbon-Carbon Technology

complex fabrication, handling, and testing procedures. (One difficulty is to fabricate large, thin face sheets.) Glass mirrors should be lightweighted also. By contrast, beryllium mirrors for LDR can be solid. As a raw material, beryllium is expensive (12 times the cost of the glasses), and although it has excellent thermal and mechanical properties, it requires substantial facilities and methods development.

Section 7
COSTING

7.1 SUMMARY

The cost basis for LDR are algorithms developed at LMSC for systems of various diameters and operating wavelengths, reasonably confirmed by several previous point designs. A 10-m-diameter system is estimated to cost $250 M, excluding Shuttle, special facilities, and operating costs. We find no significant breakpoints in the cost as a function of diameter or operating wavelength.

7.2 COST BASIS AND RESULTS

Preliminary cost estimates for conceptual systems can be developed from several different bases relating to weight, size, complexity, and previous costing experience. At a more advanced design stage of LDR, the costing effort must involve detail costing of the individual components, while for this study estimating the cost from existing, validated algorithms is appropriate. All estimates are made for one flight unit without focal plane, Shuttle flight and integration, special facilities, and operating costs.

The algorithms have been developed at LMSC as a function of aperture size, for visible and near-infrared as well as millimeter and microwave systems. The majority of these systems are about 1 m in diameter. Anticipated Space Telescope costs verify the algorithms at 2.4 m diameter. The algorithms are probably reasonably accurate out to 4-m diameter, where segmentation of the LDR primary mirror is required. Data for the 4-m optics elements were broken out of the algorithms and used as a basis of 4-m segment cost for larger apertures. Typical spacecraft costs were added to the optics cost to yield an all-up cost.

Unfortunately, no hard data exist for a system operating in the far-IR to sub-mm wavelength region, which is of primary interest to LDR. We therefore have interpolated the cost as a function of wavelength between the visible and mm-wave portions of the spectrum. The result is shown in Fig. 7-1. The approximate cost as a function of wavelength is shown separately for the telescope alone and for an entire system, i.e., satellite.

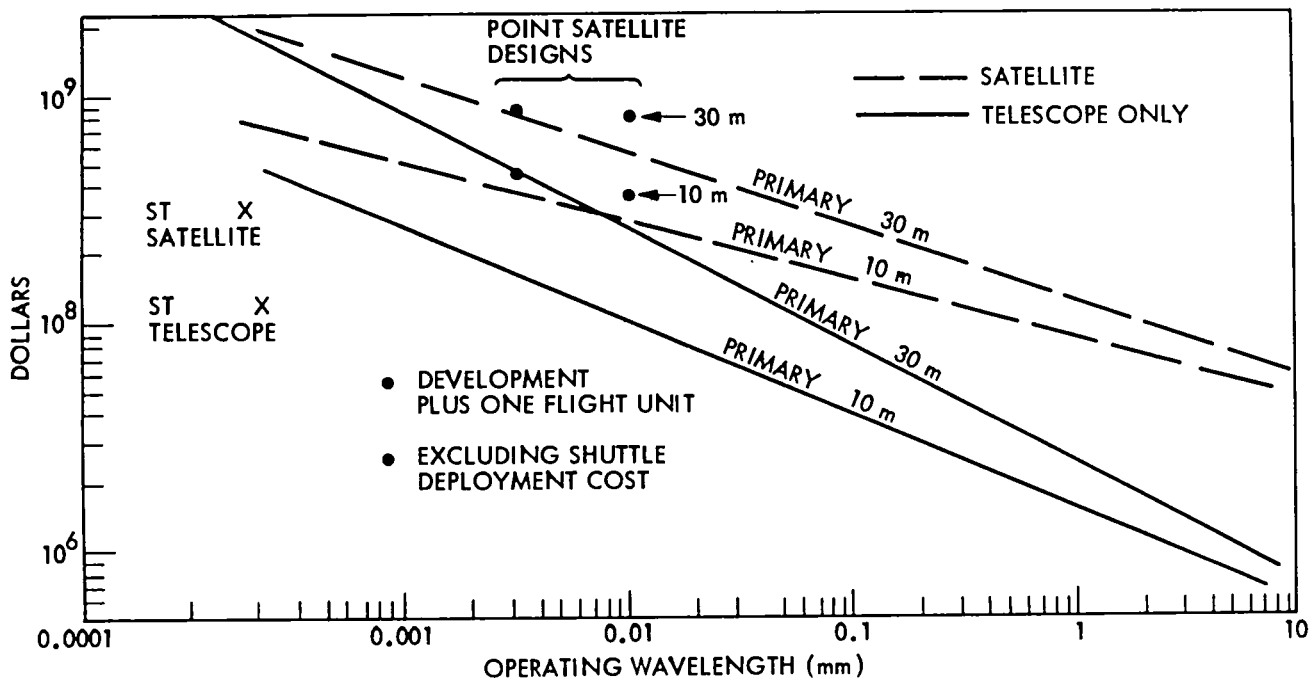

Fig. 7-1 Estimated Cost (1980 Dollars)

These estimates are of course only very approximate. However, LMSC costing of several previous 30-m-diameter point designs, shown as data points in Fig. 7-1, agree with the interpolation reasonably well. The cost of an LDR operating to 30 μm can therefore be read off Fig. 7-1 with reasonable confidence. The satellite cost for a 10-m-diameter system is \$250M and for 30-m-diameter it is \$500M. Note that the cost for a 10-m LDR is not much greater than for the 2.4-m Space Telescope; that is because the LDR is diffraction limited at 30 μm, rather than 0.6 μm, and LDR therefore has much less stringent fabrication tolerances than the ST.

There are no apparent cost breakpoints as a function of diameter or wavelength. Naturally, this is a result of the above described costing method. However, it is also unlikely that such breaks exist, for the following reason: While subsystem costs may vary among different designs and as a function of size or wavelength, its effect on the total system cost is probably small.

Section 8
CONCLUSIONS

8.1 SUMMARY

It is feasible to deploy in the early 1990's a large, ambient temperature, orbiting astronomical telescope (LDR), with a minimum primary mirror diameter of 10 m and an operating wavelength of 30 μm. Much of the critical technology for its fabrication and deployment already exists, but some is in an early, yet vigorous state of development.

8.2 BASIC STRUCTURE

The requirements for size and for Shuttle delivery determine the level of the lightweight mirror technology required for LDR, in terms of the maximum reflector mass/area ratio. This ratio depends on reflector diameter. A 10-m reflector requires only Space Telescope technology ($m/A \approx 200$ kg/m^2), whereas for a 30-m telescope, ultralightweight mirror technology is required ($m/A \approx 25$ kg/m^2).

Among current lightweight space reflector concepts, only those with rigid segments on a thermally highly inert support structure show promise for LDR. Self-deployable reflectors of this type are limited from 10 to 12 m in diameter because of their inefficient packaging capability. Without active alignment of the segments, the minimum operating wavelength of such reflectors is near 1 mm. This limit is due to limits on the accuracy of the initial deployment and subsequent reflector shape accuracy under the severest thermal loads of LDR.

A practical limit for the maximum size of a reflector which is deployed by placing the mirror segments on a previously unfolded support structure (an assembled mirror) is near 30 m. This limit is due to the fact that the required maximum

reflector mass/ratio (areal density) is about 25 kg/m^2, which is presently considered a lower limit achievable in the LDR time frame. Assembled reflectors can be much large than self-deployable ones because the mirror segments can be packaged in the Shuttle with greater volume efficiency.

8.3 OPTICAL FORM AND CONTROL

The preferred optical form of LDR is a two-mirror Cassegrain, with a f/0.5 parabolic primary mirror. (For operations down to 2 μm, the f/ratio needs to be reexamined). Other possible forms are either unnecessarily complex - and thereby more risky in terms of deployment and control - or they do not satisfy the performance requirements. Field-of-view scanning by secondary mirror chopping at 10 Hz is feasible, except the performance of LDR may be compromised at wavelengths lower than the required 30 μm and for large secondary mirror diameters.

Several techniques exist for alignment, i.e., on-orbit sensing and control of the positions of the mirror segments on the support structure. Such alignment is required for diffraction-limited performance at 30 μm. Curvature control of the segments is not required except for aluminum segments at wavelengths below 0.5 mm and for glass or Be segments operating below about 2 μm. A wavelength limit of 2 μm of LDR would be desirable but would stress the capabilities of current sensors. The point is worth reexamining.

Pointing and slewing requirements of LDR do not stress the state-of-the-art. The excitation of structural vibrations by control systems (CMGs are preferred for LDR) and by the secondary mirror oscillation may present difficult but probably not insurmountable problems in LDR design.

LDR does not require a sun shield to keep the background noise in the focal plane below that created by the thermal emission of the ambient temperature optics. However, for the purpose of thermal control, by which the requirements for the thermal stability of the mirror segments may be lessened, the need of a sun shield should be reexamined.

8.4 MATERIALS

A preliminary analysis was conducted of the response of various candidate materials for LDR mirror segments and support structure (truss), to the thermal and inertial constant loads. The time-varying loads were not studied and must be considered in the future. The analysis showed that only lightweight glass (ULE, CerVit), properly doped, or solid beryllium segments satisfy the performance requirements. The preferred material for the mirror support structure is graphite/magnesium.

Aluminum segments of the type used in the Leighton 10-m, millimeter antennas are limited to operations above about 0.5 mm. Yet, aluminum is inexpensive and segment construction is, as the Cal Tech dishes show, well advanced in technique. Therefore, a passive (no on-orbit segment alignment), 10 to 12-m diameter, self-deployable LDR operating at near-millimeter wavelengths has been proposed as a possible LDR baseline concept (Table 1-2). However, the total cost (including Shuttle, special facilities development, and operational costs) of a 10-m telescope of this type is probably not substantially lower than a 10-m telescope with better segments and active alignment. Considering that the science potential of a telescope working to the near-infrared rather than near-millimeter wavelengths is considerably greater, a passive 10-m aluminum LDR may ultimately be rejected as a nonviable concept.

Lightweight glass mirror technology now in development, such as the FRIT technology, promises to satisfy the m/A requirement for a 30-m-diameter LDR. The alternate technology, using solid beryllium segments made with vacuum deposition techniques, is yet in early stages of development. To meet the LDR time frame, substantial advance in terms of facilities and development is needed.

8.5 COST

Parametric costing of a telescope like LDR is presently only feasible using costing algorithms which were previously developed for either optical or microwave reflectors, and by interpolating between these wavelength regions. Several known

point designs confirm the reasonable accuracy of such a method. The unit cost for a 10-m reflector, excluding Shuttle and facilities development costs, is about $250M; for a 30-m-diameter reflector, it is about $500M. No significant cost breakpoints, as function of diameter or minimum operating wavelength, were determined.

8.6 SYSTEMS BREAKPOINTS

This study offers three distinct LDR baseline concepts which may be considered in further studies; they are given in Table 1-2. They reflect the existence of several breakpoints in the conceptual design of LDR.

(1) In terms of the operating wavelength, breaks occur near 1 mm and 2 μm. A near-mm wavelength telescope requires no active segment alignment and can even be built with inexpensive aluminum hexel segments. (However, a thermally inert support structure is still needed, such as made of Gr/Mg.) At lower wavelengths, actively aligned glass or beryllium segments are required. Below about 2 μm, segment figure control is required in addition to segment alignment. Operation to 2 μm may exceed the accuracy of alignment sensors, but operation to 30 μm will not.

(2) In terms of maximum reflector diameter that is possible if, as required for this study, only one Shuttle load is allowed for LDR deployment, the breakpoints are near 12 m and 30 m, respectively. The first point represents a change, from self-deployable to assembled reflector concepts. The second represents a lower, probable, limit to the reflector mass/area ratio achievable in the LDR time frame.

The locations of these breakpoints are, of course, not exact and represent best engineering judgment.

Our results are summarized in Fig. 8-1 which ranks various LDR concepts in terms of cost, but without a definite cost scale since such a scale cannot be derived at this time. The bottom line of the results can be expressed as follows: A 10-m

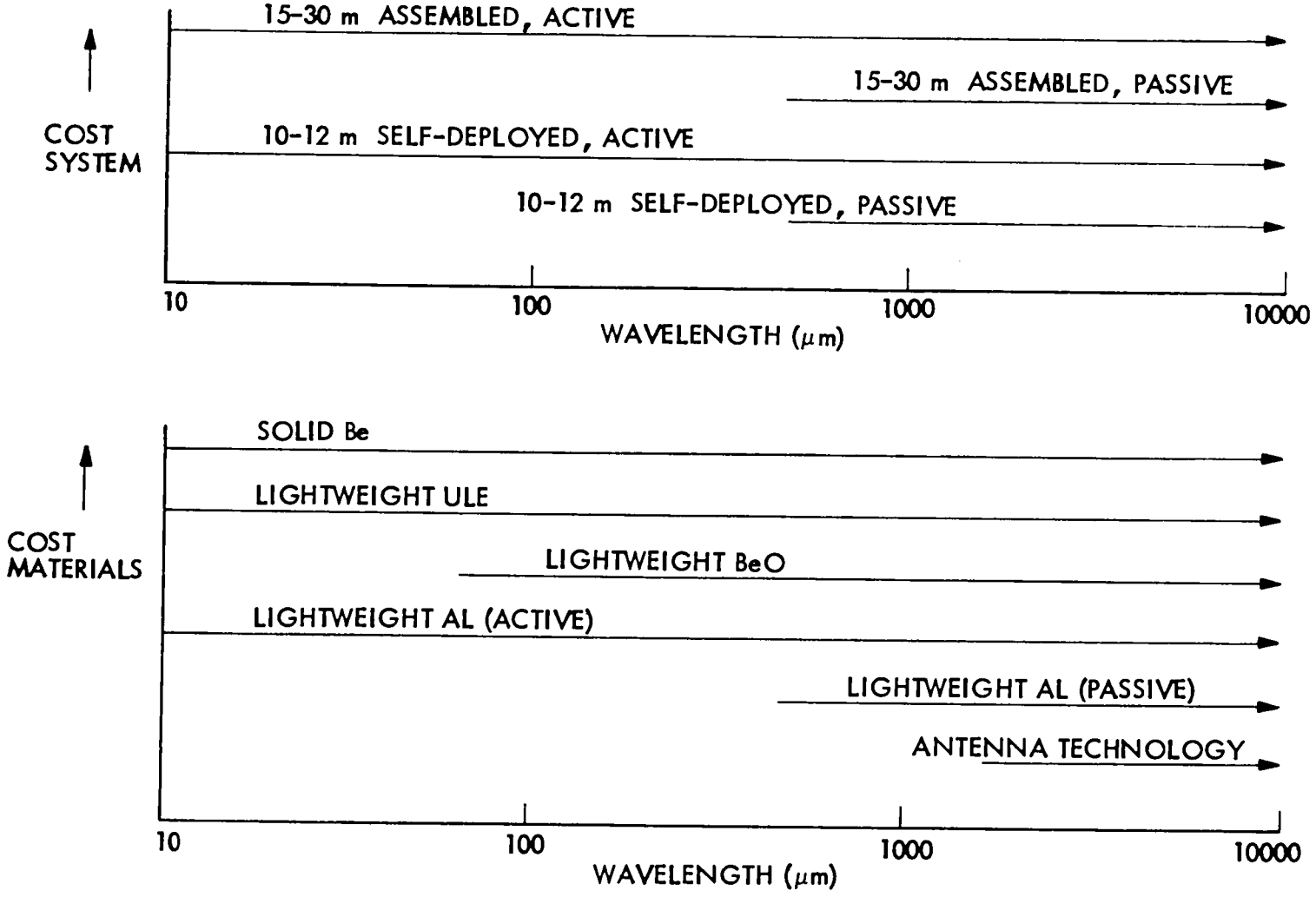

Fig. 8-1 LDR Technology, Performance, and Cost

diameter, self-deployable reflector can be built with present technology. A 30-m-diameter reflector requires technology, some of which is yet in the state of development but which probably meets the LDR time frame requirements.

Appendix A

LDR Background Limited Sensitivity

A.1 Introduction

LDR sensitivity is limited by noise in the radiation on the focal plane, due to various internal and external sources which may be inside or outside the detector field of view (FOV). If the power on a detector from this background is $dP(\lambda)$ in the wavelength interval $d\lambda$, then the noise power per $\sqrt{H_z}$ is

$$\frac{NEP}{(W/\sqrt{H_z})} = \left\{ \int h\nu \left[1 + \frac{1}{e^{h\nu/kT} - 1} \right] dP \right\}^{\frac{1}{2}} \qquad (1)$$

where T the temperature of the noise source, $\nu = c/\lambda$ the frequency, c the speed of light, h Planck constant and k Boltzmann's constant. For unit optical efficiency

$$dP = A_p \Omega_d \frac{2hc^2}{\lambda^5} \varepsilon \frac{d\lambda}{e^{h\nu/kT} - 1} \qquad (2)$$

where A_p the area of the primary mirror ($= \pi D^2/4$), Ω_d the solid angle of the detector $= (2.44\lambda/D)^2$, ε the source emissivity. For $\Delta\lambda/\lambda \ll 1$ (we assume $\Delta\lambda/\lambda = 0.1$),

$$\frac{NEP}{(W/\sqrt{H_z}} = 1.05 \times 10^{-11} \frac{e^{7.2 \times 10^3/\lambda T}}{e^{1.44 \times 10^4/\lambda T} - 1} \sqrt{\frac{\varepsilon}{\lambda^3} \frac{\Delta\lambda}{\lambda}} \qquad (3)$$

A.2 Sky Background

Important background sources are interplanetary and interstellar dust, and the 3°K background. Atmospheric (continuum) radiation above a typical LDR orbit (600-700 km) is negligible. Values of ε/λ and T are given in Table A-1 for these sources, and the NEP's for these sources are plotted in Fig. A-1. (The visible and ir zodiacal light are given for 60° solar elongation in the ecliptic plane as well as for the ecliptic poles, where the zodiacal light is minimum, because the minimum solar elongation specified for LDR by the SOW is 60°). Note that the background NEP is typically 10^{-18} to 10^{-17} $W/\sqrt{H_z}$ independent of D, and, on average, increases with increasing wavelength.

Table A-1

Diffuse Sky Above Atmosphere

Source	Emissivity, ε	Temperature, T (K)
Interplanetary dust:		
Zodiacal Light [+] (visible)	3.7×10^{-14}	(same as Sun)
Thermal (ir)	$1.2 \times 10^{-7} / \lambda_{\mu m}$	300
Galactic dust [++]	$10 / \lambda^2_{\mu m}$	10-15
Cosmic background	1	2.7

+ scattered sun light

++ galactic poles

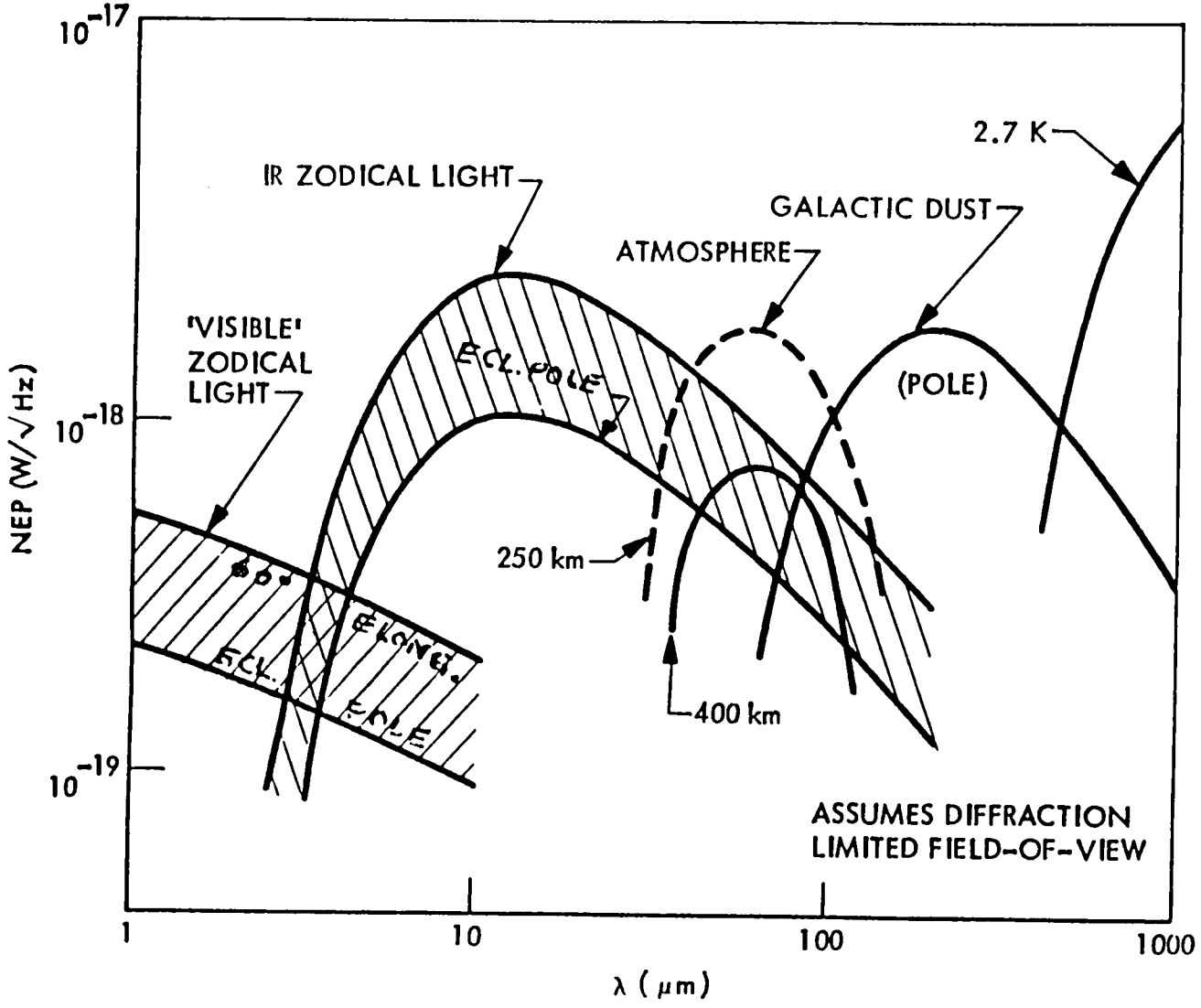

Fig. A.1 Celestial Background Limited Sensitivity

A.3 Thermal Emission from LDR Optics and Structure

We consider the following important sources of thermal radiation

- Mirrors at ambient temperature (primary, secondary, relay)
- Structure (secondary support, spider)
- Segment gaps
- Dust on mirrors
- Filter (detector cavity)

Their contribution to the instrumental noise increases with their relative area, A/A_p, as well as with T and ε.

Table A-2

Instrument Background Emission

	A/A_p	T	$\varepsilon(\lambda)$
Mirror(s)	1	150-300	0.02-0.1
Structure	$6\ t/\pi D$	same	0.02-1
Segment gaps	$2\ w/d$	same	0.02-1
Dust	10^{-3}	same	≤ 1
Filter	1	see text	≤ 1

For the support structure of the secondary mirror we assume a projected area of $3(D/2)t$, where t the average width of a truss member; hence $A/A_p = (3/2) D \cdot t/(\pi D^2/4)$. For a nominal range t =10 to 30 cm, A/A_p =.006 to .06.

For segment gaps, the total area is approximately $A = (N/2)\ \pi dw$, where N is the number of mirror segments, d the average diameter, w the gap width. Since $N = A_p/(\pi D^2/4) = D^2/d^2$, we have $A/A_p = 2\ w/d$.

For dust on mirror surfaces we assume a Class 300 dust distribution, achievable by assembly in a Class 100,000 Clean Room. For that distribution, $A/A_p = \int \pi a^2 dN(a) \approx 10^{-3}$, where dN(a) is the number of dust particles with radii between a and (a+da).

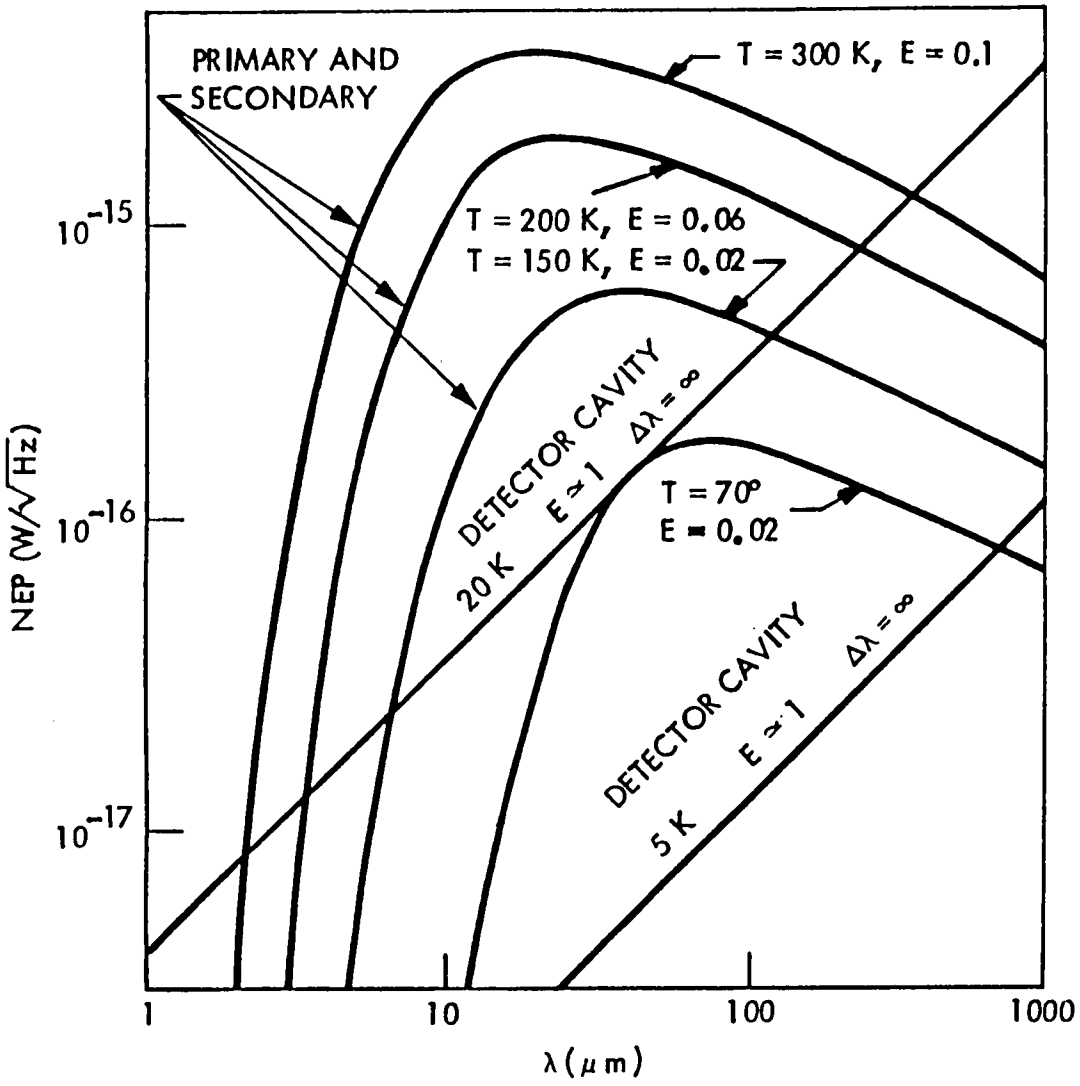

Fig. A.2 Telescope Background Limited Sensitivity

For the above instrumental background sources we assume the same temperatures as the primary mirror, T = 150 - 250 K. Filters are expected to be cryogenically cooled, some to as low as ℓHe temperatures. A filter radiates to the detector at all wavelengths with efficiency $\varepsilon \approx 1$, except in the spectral range $\Delta\lambda$. The filter NEP is calculated from Eqs. (1) and (2) by integrating our all wavelengths (neglecting the transparency of the filter at λ), which gives

$$\frac{NEP}{(W/\sqrt{H_z}} \approx 2.2 \times 10^{-15} T^{5/2} \lambda_{\mu m} \qquad (4)$$

Fig. 2 shows the results of the above calculation for nominal values of the system parameters discussed above. Comparison with Fig. 1 shows that instrumental thermal emission is much larger than the sky background at all but the shortest possible operational wavelengths of LDR.

A.4 Stray Light from Sources Near the FOV

Bright star in or near the FOV can raise the background radiation in the focal plane (FP) appreciably. The power on the focal plane is:

$$dP = \frac{2hc^2}{\lambda^5} \frac{d\lambda}{e^{h\nu/kT_s} - 1} \Omega_s A \qquad (5)$$

where T the stellar temperature, Ω_s the solid angle of the stellar disk subtended at the telescope, and A the area of instrumental surface scattering or diffracting the stellar power into the FOV of a detector. The power on the detector is $\Delta P \cdot S_\Theta(\lambda) \cdot \Omega_d$ where $S_\Theta(\lambda)$ the scattering function (units: sr^{-1}), discussed below for various types of scattering. By comparison on Eq. (2) and Eq. (5) we see that to calculate the corresponding NEP from Eq. (1), we need to replace ε in Eq. (2) by the quantity $\Omega_s \cdot S_\Theta \cdot (\lambda) \cdot A/A_p$.

For small angles Θ, the dominant scattering mode is (forward) diffraction - by the primary aperture and the spider. Minor contributions to the NEP are made by scattering from mirror roughness (BRDF) and dust. The appropriate functions are listed in Table A.2. For a solar-type star of magnitude m_V,

$$\Omega_s \approx 1.3 \times 10^{-(15 + 0.4 m_v)} \ (sr^{-1}) \qquad (6)$$

Table A-3

Scattering Functions ($\Theta << 1$)

Scattering Surface Mechanism	$S_\Theta(\lambda)$	A/A_p
Mirror Diffraction	$\lambda/D\pi^3\Theta^3$	1
Spider (cross) Diffraction	$D/2\pi t\Theta^2$, $\Theta\pi t >> \lambda$ $Dt/2\lambda^2$, $\Theta\pi t >> \lambda$	$\frac{\pi}{8}\, t/D$
Dust (Class 300) Diffraction	$< 1.2 \times 10^{-9}(\pi/\lambda)^2$	10^{-3}
Mirror (ULE*) Scatter	$\frac{3 \times 10^{-18}}{\lambda^2} \cdot \frac{1}{\Theta^2 + 3.8 \times 10^{12}\lambda^2}$	1

*) Adapted from ITEK 75-9507-1

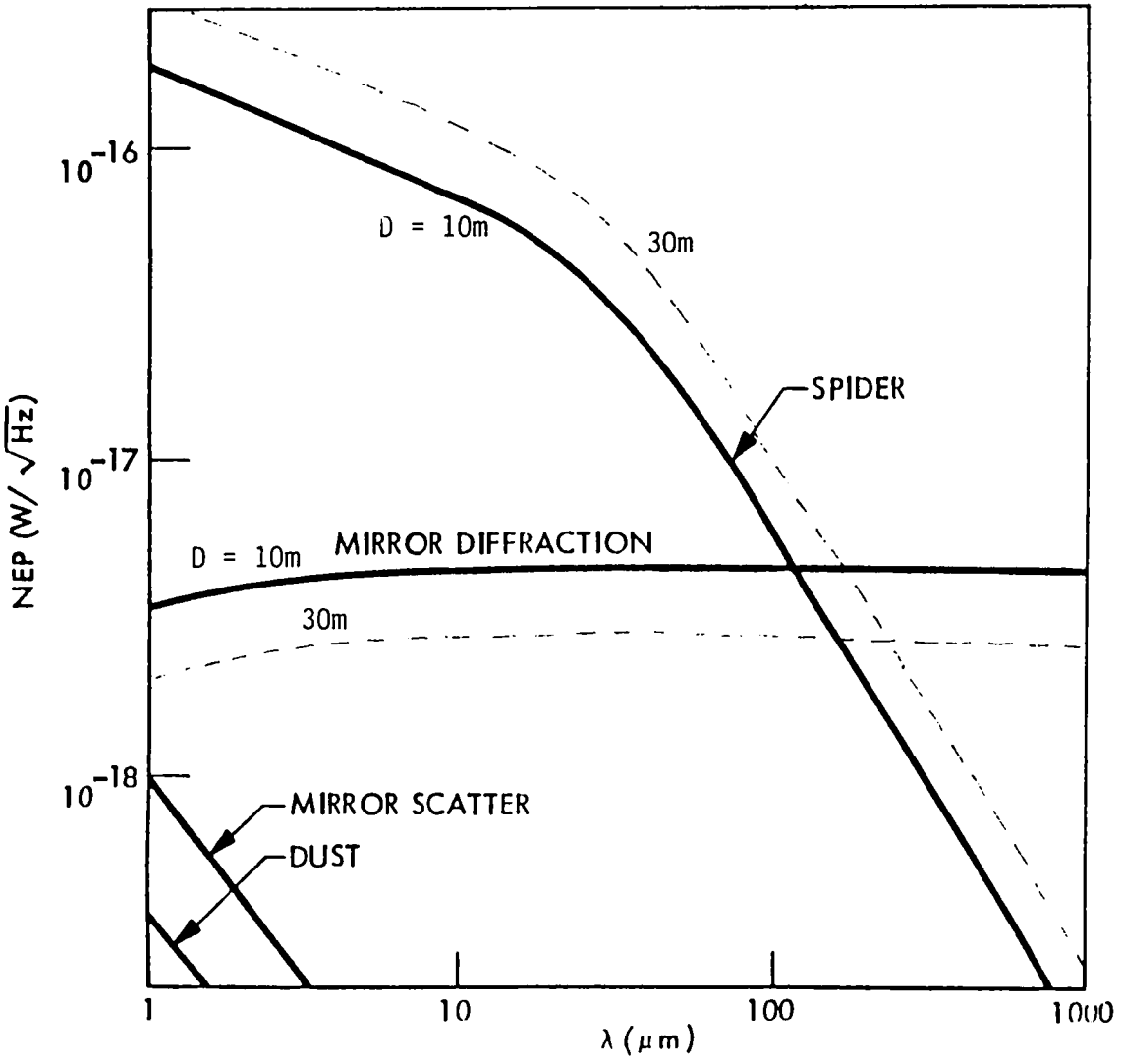

Fig. A.3 Sensitivity Limits Due to Off Axis m_V(G2V) = 0 Star

Results for D=10m, t=.1m are shown in Fig. A.3 for a m_V(G2V)=0 star off-axis by 15$\hat{s}$. Spider diffraction is important at $\lambda < 100\mu m$, and mirror diffraction at longer wavelengths.

A.5 Sun at 60° Elongation

For a 60° elongation angle, we can treat the sun as a point. The scattering mechanism is diffuse scattering rather than diffraction as in Sec. 1.4. Important scattering surfaces are gaps between segments, dust on the mirror, and mirror roughness (BRDF). For the first three we assume Lambertian scattering for the last we take $S_\Theta(\lambda)$ as given in Table A3. The results are shown in Fig. A.4 for a range of values of the relative gap area (A/A_p = 2 w/d).

A.6 Earth Albedo and Earth Shine

For scattering of radiation from an extended source outside the FOV, like the earth's limb, the function $S_\Theta(\lambda)$ must be summed over all applicable scattering angles Θ:

$$\overline{S}(\lambda) = \int_{\Omega_E} S_\Theta(\lambda) \cos\Theta \, d\Omega_E \qquad (7)$$

For order-of-magnitude estimates it is sufficiently accurate to replace $\cos\Theta$ by unity since the major contribution to the NEP comes from scattering through small angles. This gives the results shown in Table A.4 and the NEPs shown in Fig. A.5. The solid lines represent albedo contributions; the dotted lines earth shine.

Table A.4

Integrated Scattering

Surface	Mechanism	$\int S_\Theta(\lambda) d\Omega_E$
Mirror	Diffraction	$2\lambda/D\pi^2\Theta$
"	BRDF	$(6\pi \times 10^{-18}/\lambda^2)\sin\Theta$
Spider	Diffraction	$\lambda/\pi^3 D\Theta$
Gaps	Scattering	Θ^2
Dust	Diffraction	$1.2 \times 10^{-8}\pi\Theta^2/\lambda^2$

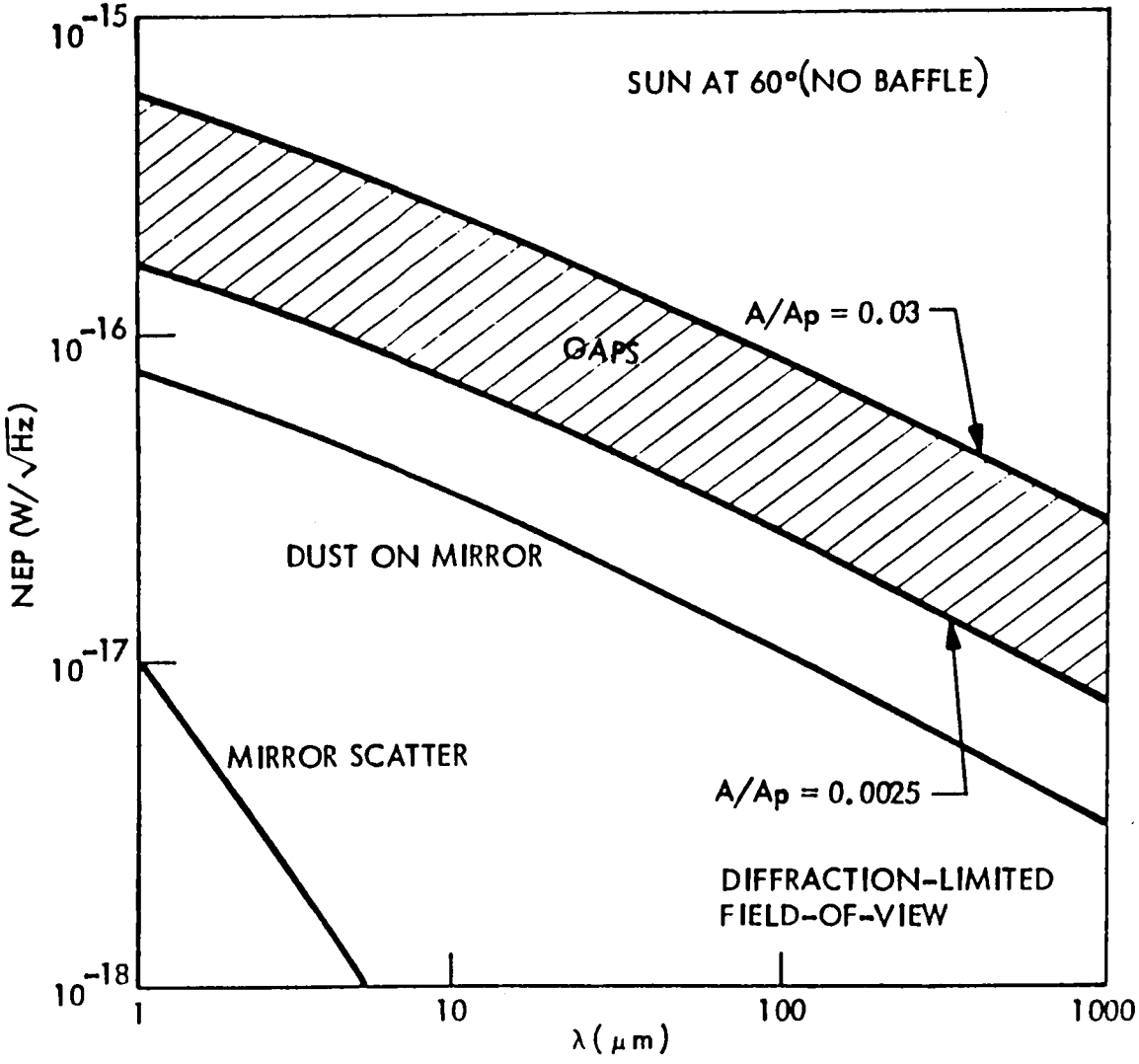

Fig. A.4 Solar Stray Light Limited Sensitivity

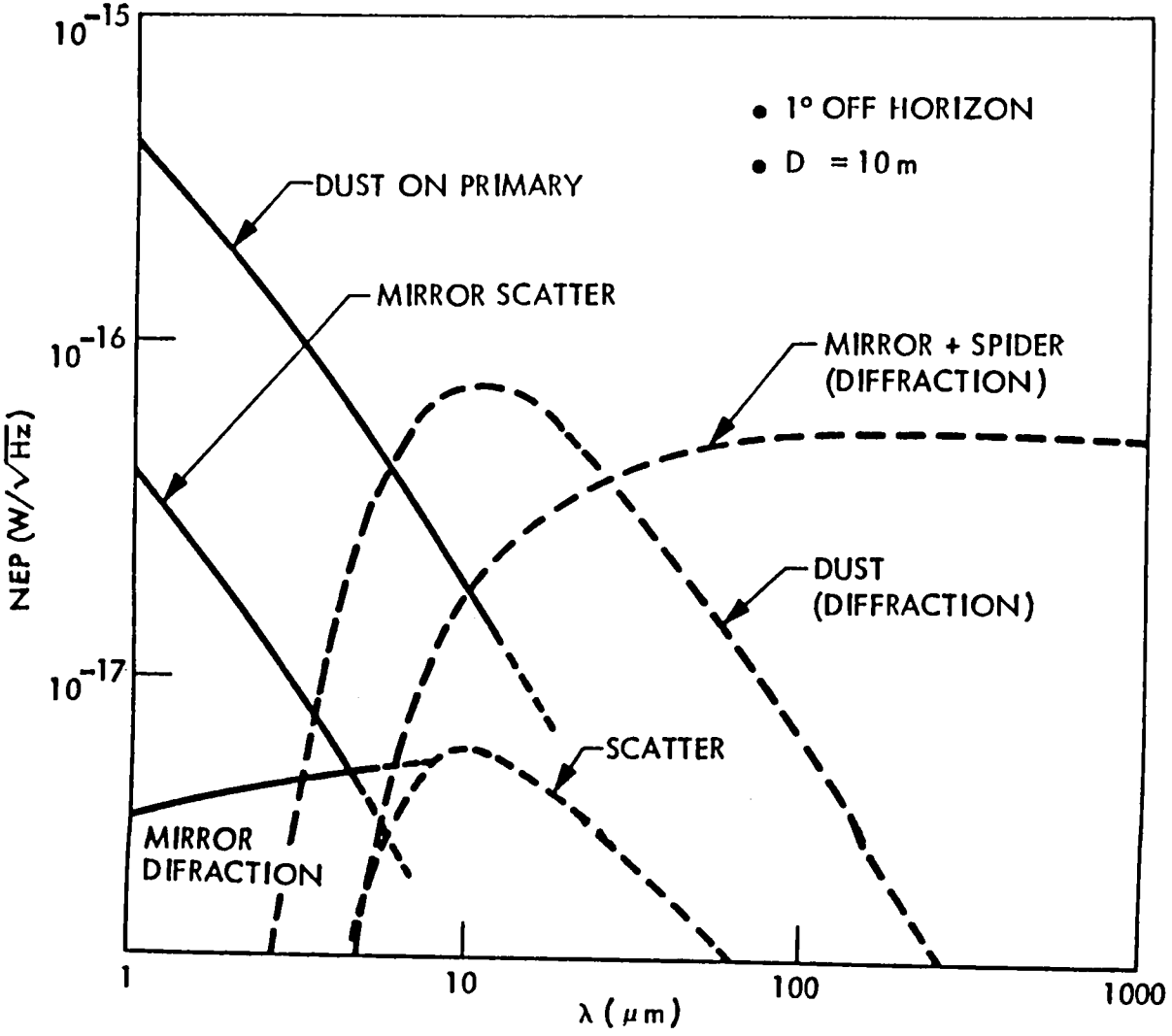

Fig. A.5 Earth Background Limited Sensitivity

Appendix B

Image Quality of Two-Mirror Telescopes

Summary:

This appendix derives expressions for the third order field aberrations of coma and astigmatism for the following optical designs:

A) Ritchey Chrètien
B) Parabolic Primary
C) Tilted Aplanat
D) Spherical Primary

The third order aberrations of the above systems are useful for estimating telescope field of view (FOV) as a function of primary diameter, D, primary focal ratio, F, and field angle α to determine whether the requirements of the SOW can be met. These requirements are:

1) Diffraction limited performance (OPD $\leq \lambda/10$ rms) at λ = 2 μm over the center 30 sec of field.

2) Diffraction limited performance over 10 x the beam width (24.4 λ/D) for 100 μm $\leq \lambda \leq 10^{-3}$ meter.

Implied in the above is that the telescope optics and focal plane must be physically large enough to provide an unvignetted imaging capability at $\alpha = 1.22 \times 10^{-2}/D$ off of the optical axis. The derived expressions lead directly to the selection of the parabolic primary design for the LDR telescope.

Discussion:

The starting points of this analysis are the expressions for third order aberrations in reference 1.

The telescope principle focal plane is assumed to be located at the vertex of the primary mirror. This assumption allows considerable simplification of the algebra without obscuring the general trends. The assumption is conservative in that an increase in back working distance to accommodate a recessed focal plane should, if anything, reduce the field aberrations.

According to equations 11, 12 of reference 1, the total angular aberration in the focal plane of the telescope is given by

$$\eta = A_1 \left(\frac{a}{f}\right)^3 \rho^3 \cos\Theta + A_2 \left(\frac{a}{f}\right)^2 \alpha\rho^2(2 + \cos 2\Theta) + (2A_3 + A_4)\cdot \quad (1)$$
$$\cdot\left(\frac{a}{f}\right)\alpha^2\rho \cos\Theta + A_5\alpha^3$$

$$\xi = A_1 \left(\frac{a}{f}\right)^3 \rho^3 \sin\Theta + A_2 \left(\frac{a}{f}\right)^2 \alpha\rho^2 \sin 2\Theta + A_4\left(\frac{a}{f}\right)\alpha^2\rho \sin\Theta \; . \quad (2)$$

The aberration coefficients $A_1 \cdot A_5$ are spherical aberration, coma, astigmatism, sagital curvature and distortion, respectively. These coefficients depend on the telescope design. Parameters ρ and Θ are aperture coordinates of radius (ρ = 1 at aperture edge) and angle, respectively. The primary mirror aperture radius is a; the λ telescope effective focal length is f. Angular coordinates η (the Θ = 0 direction) and ξ represent the deviation from an ideal point image in the focal plane of parallel rays passing through the telescope aperture at (ρ,Θ). The deviation is given in units of angle in object space.

Angular error in object space can be related to wavefront error at the telescope input aperture $\Delta(\rho,d)$ by the relations[2]

$$\eta = \frac{1}{a}\left(\cos\Theta\frac{\delta\Delta}{\delta\rho} - \frac{\sin\Theta}{\rho}\frac{\delta\Delta}{\delta\rho}\right) \quad (3)$$

$$\xi = \frac{1}{a}\left(\sin\Theta\frac{\delta\Delta}{\delta\rho} + \frac{\cos\Theta}{\rho}\frac{\delta\Delta}{\delta\rho}\right) \quad (4)$$

where

$$\Delta(\rho,\Theta) = W_{20}\rho^2 + W_{40}\rho^4 + W_{01}\rho\cos\Theta + W_{02}\rho^2\cos^2\Theta + W_{21}\rho^3\cos\Theta \; . \quad (5)$$

The terms in this expression correspond to focus, spherical aberration, tilt, astigmatism and coma.

Performing the indicated partial differentiation, we can relate the A and W coefficients as:

$$W_{20} = \frac{a^2 A_4 \alpha^2}{2f} \qquad \text{Sagital defocus} \qquad (6)$$

$$W_{40} = \frac{a^4 A_1}{4f^3} \qquad \text{Spherical aberration} \qquad (7)$$

$$W_{02} = \frac{a^2 A_3 \alpha^2}{f} \qquad \text{Astigmatism} \qquad (8)$$

$$W_{21} = \frac{a^3 A_2 \alpha}{f^2} \qquad \text{Coma} \qquad (9)$$

$$W_{01} = a A_5 \alpha^3 \qquad \text{Distortion} \qquad (10)$$

Mean curvature of field (image defocus at the image plane as a function of field angle) is

$$\frac{W_{02}}{2} + W_{20} = (A_3 + A_4) \frac{a^2 \alpha^2}{2f} \qquad (11)$$

Distortion (A_5) does not degrade a point source image but produces a slight displacement of the image in the focal plane.

We can now use Table III of reference 1 to calculate wavefront error. In the quoted expressions, the quantity s = +1 because of the assumption of a back working distance of zero. $A_1 = 0$ for all of these systems (i.e. zero third order spherical aberration).[1] The quantity m is secondary magnification; i.e.

$$m = f/DF \qquad (12)$$

A) Ritchey Chrétien Design

Coma: $A_2 = 0$

Ritchey Chrétien telescopes have no third order coma

Astigmatism:

$$A_3 = -\left[\frac{m + s - \frac{1}{2}}{2s}\right] \overset{s = 1}{=} -\left[\frac{m + \frac{1}{2}}{2}\right] \tag{13}$$

Hence,

$$W_{02} = \frac{-(2m + 1) D \alpha^2}{16mF} \tag{14}$$

(OPD at aperture edge)

The rms wavefront of astigmatism and defocus is [3] eq. 15 divided by $\sqrt{24}$.

$$\omega = \frac{(2m + 1) D \alpha^2}{32\sqrt{6}\, m\lambda F} \quad \text{(rms waves)} \tag{16}$$

The effects of curvature of field and distortion are ignored in this appendix since it is assumed that the image detectors lie on the image surface of optimum focus and that distortion can be completely removed by image processing.

B) Parabolic Primary Design

Coma:

$$A_2 = -\frac{1}{4} \tag{17}$$

$$W_{21} = \frac{-\left(\frac{1}{4}\right) D \alpha}{8 m^2 F^2} \quad \text{(OPD at aperture edge)} \tag{18}$$

Conversion to rms wavefront error requires a division by 3 to remove the tilt inherent in the comatic form $\rho^3 \cos \phi$ and a further division by $\sqrt{8}$ to convert from aperture edge error to rms error, yielding

$$\omega = \frac{D\alpha}{96\sqrt{8}\, m^2 \lambda F^2} \quad \text{(rms waves)} \tag{19}$$

Astigmatism:

$$A_3 = -\left[\frac{m + s - 1}{2s}\right] \overset{s = 1}{=} -\left(\frac{m}{2}\right) \tag{20}$$

Hence,

$$\omega = \frac{D\alpha^2}{16\sqrt{6}\,\lambda F} \qquad \text{(rms waves)} \qquad (21)$$

C) Tilted Aplanatic System

Coma: (from P 2967 of Ref 1)

$$A_2 = \frac{1}{8}(m^2 - 1) \qquad \text{(field aberration away from the focal plane center)} \qquad (22)$$

Hence,

$$W_{21} = \frac{(m^2 - 1)\, D\alpha'}{64\, m^2 F^2} \qquad \text{(OPD at aperture edge)} \qquad (23)$$

where α' is the look angle separation of the object from the off-axis object lying at focal plane center.

$$\omega = \frac{(m^2 - 1)\, D\alpha'}{192\sqrt{8}\, m^2 \lambda F^2} \qquad \text{(rms waves)} \qquad (24)$$

Field coma in this system is $m^2/2$ times that existing in the parabolic system. In addition, the tilted aplanat telescope has significant amounts of both astigmatism and spherical aberration even in the image centered in the focal plane.

Astigmatism:

$$A_3 = -\frac{1}{8}\left[(3m + 1) + \left(\frac{2m^2 + m - 1}{8s}\right)\right]^{s=1} = -\frac{1}{4}\, m(m + 2) \quad . \qquad (25)$$

Hence,

$$W_{02} = -\frac{1}{16}(m + 2)\,\frac{D\alpha^2}{F} \qquad \text{(OPD at aperture edge)} \qquad (26)$$

where α is the angle between the primary optical axis and the object centered at the focal plane by secondary mirror tilt.

$$\omega = \frac{(m + 2)\, D\alpha^2}{32\sqrt{6}\,\lambda F} \qquad (27)$$

Therefore, astigmatism is $\frac{m+2}{2}$ times that of the Parabolic System.

D) Spherical Primary System

The aberration coefficients, $A_1 \ldots A_5$ for spherical primary two-mirror telescopes are not calculated in reference 1 and must be derived here using Table 1. The condition that spherical aberration, $A_1=0$, requires that, with $e_1 = 1$ (a sphere),

$$a_1 = \frac{m^3}{8\gamma} = \frac{m^3(m+1)}{8} \tag{28}$$

since for $s = 1$, $t = \gamma = (m+1)^{-1}$.

(Parameters t, γ are defined in reference 1)

Coma:

$$A_2 = -\frac{1}{4}m^2 - \frac{m^3}{8} + \frac{1}{4}m^2 - \frac{1}{4} = -\frac{1}{8}(m^3+2) \tag{29}$$

$$W_{21} = -\frac{1}{64}\left(\frac{m^3+2}{m^2}\right)\frac{D\alpha}{F} \qquad \text{(OPD at aperture edge)} \tag{30}$$

or

$$\omega = \frac{(m^3+2)\,D\alpha}{192\sqrt{8}\,m^2\lambda F^2} \qquad \text{(rms waves)} \tag{31}$$

Astigmatism:

$$A_3 = +\frac{1}{8}m\left[m^2-4\right] \tag{33}$$

$$W_{02} = \frac{\left[m^2-4\right]D\alpha^2}{32F} \qquad \text{(OPD at aperture edge)} \tag{34}$$

Hence,

$$\omega = \frac{(m^2-4)\,D\alpha^2}{64\sqrt{6}\,\lambda F} \qquad \text{(rms waves)} \tag{35}$$

These results are summarized in Table 4.1 in the section on Optical Configuration.

Reference

1) Third Order Aberrations in Cassegrain-type Telescopes and Coma Correction in Servo-Stabilized Images", M. Bottema & R. A. Woodruff Applied Optics/Vol. 10, No. 2/February 1971. P300.
(See also Applied Optics, Vol. II, No. 12/December 1972, P2965)

2) "Introduction to Statistical Optics", Edward O'Niell, Addison Wesley (1963) P50.

3) "The Use of Image Quality Criteria in Designing a Diffraction Limited Large Space Telescope", William B. Wetherell. Vol. 28 Proceedings SPIE "Instrumentation in Astronomy" P65.
(See also Applied Optics/Vol. 11, No. 12, P2851)

Appendix C

Alignment System Sensor Modeling Technique

A. Introduction

In this appendix, a technique for converting alignment sensor measurements and alignment system geometry (i.e., sensor type and location) into misalignment parameters is developed. The technique can be implemented by a computer program into a high speed, linear operation converting sensor measurements into parameters suitable for input to the segment alignment control system. The technique is applied to two different types of misalignment sensors. In additio a simple error analysis is performed and is used as a design tool and to provide insight of measurement error propagation.

This analysis assumes that each segment position, as defined by an attached reference plane, may be determined by measurement of the location of at least three points in the reference plane. These points are called reference points. Physically, they are corner cubes, centroid detectors, scratches in the mirror surfaces - any device which provides a reference and is fixed in (or near to) the reference plane. Measurement of the location of each reference plane of each segment in a common alignment coordinate system constitutes a segment alignment measurement since segment misalignment is a segment position error relative to the other segments.

The mirror segment is assumed to be a rigid body (i.e., it does not bend or expand). The rigid body assumption may be relaxed at the expense of additional modeling complexity and additional measurement (reference) points. The assumption that the measurement points are located in a reference plane, as described above, is an idealization having, for small deviations, a negligible effect on the alignment model; any deviations in reference point positions from the ideal may be calibrated during initial measurements.

The problem addressed here is how well can we determine the position and orientation of the reference plane using measurement data made from realistic sensors in a specified geometric configuration.

Two basic alignment system types are considered; the Single Axis Concept and the Trilateration Concept.

B. The Single Axis Alignment Concept

In the Single Axis concept, measurement of a vector from a single alignment system source point to each of the three reference points (RP) per segment

is performed. The measured vector will generally be close to but (because of misalignment) different from the ideal vector expected from an aligned system. The vector length from source to each RP is measured by the Optical Position Sensor (OPS), a two color interferometer. The vector cross range errors from the ideal is measured by a Lateral Position Sensor (LPS). Together these two sensors allow the measurement of the location of each RP in the coordinate system.

The alignment system source point is located near the prime focus and is supported by the secondary mirror support structure. For our purposes, we assume without loss of generality that it is at the prime focus (although it would, in that case, be blocked from a view of the primary by the secondary). This system is illustrated in Figure C.1. Nine measurements are made (three vectors of three components each) for each reference plane.

C. The Trilateration Concept

OPS measurements (length only) are made to each RFP from at least three separated source points in a plane nominally containing the prime focus and perpendicular to the optical axis. The source points form an equilateral triangle about the optical axis. The concept is shown in Figure C.2. Again, nine measurements are made (3 length measurements per RP) for each reference plane.

D. Measurements Required for Reference Plane Definition

Complete specification of Reference Plane location requires at least six measurements - one for each degree of freedom. However, the six measurements must be independent. For example, measurement of the (x,y,z) location of two points on the reference plane provides six parameters, but since the separation of the two points in a rigid body is fixed, one of the six parameters is not independent. The additional parameter might be the range to a third point on the reference plane. Selection of the appropriate independent measurement parameters depends on the alignment system concept.

A minimum of three points is required to define the location of the reference plane; hence nine measurements per 3 RP segment are obtained in each alignment concept. Instead of discarding three of the nine measurements, we include the extra data to reduce measurement error.

E. Reference Plane Position Measurement: Single Axis Concept

This problem is to measure the reference plane position by OPS and LPS located at the prime focus. The following procedure is used. First, the vectors from the prime focus to the RP defining the aligned reference plane are determined, i.e. the vectors from the prime focus to the three reference points located at $(x + p_i, y + q_i)$, $i = 1, 2, 3$ where the subaperture center is at (x,y). These vectors, $\vec{M}_i$, are the sum of the vector $\vec{M}_0$ to the reference plane center and $\vec{U}_i$ from the reference plane center to each RP. The misalignment vector, $\vec{\Delta}$, a

function of the misalignment parameters and RP coordinates are determined and added to the "ideal" vectors, $\vec{M}_i$ defined above. If a segment is misaligned, the vector $\vec{M}_i$ is changed to $\vec{M}_i + \vec{\Delta}_i$.

The change in M_i is measured by the OPS and LPS sensors with each sensor measuring the appropriate component to determine changes. The result is nine linear equations (the sensor measurements, G) in six unknowns (the misalignment parameters, P) or in the matrix equation.

$$G = AP \quad . \quad \text{Then}$$

$$A^T G = A^T A P \quad .$$

The least square solution is

$$P = [A^T A]^{-1} A^T G$$

where A^T is the transpose matrix of A and $[A^T A]^{-1}$ denotes the inverse of $[A^T A]$. This approach is valid for small misalignment amplitudes since, as will be seen, second order terms will be dropped. The solution is a set of linear equations which relate the sensor measurements directly to misalignment parameters. The matrix inversion depends only on the alignment system geometry and hence need only be performed once. Thereafter, a simple summing of measurements yield each misalignment parameter.

Error propagation from G to P is also determined easily.

$$\frac{\partial P_i}{\partial G_j} = \left\{ [A^T A]^{-1} \; A^T \right\}_{ij} \equiv B_{ij}$$

Hence, for random independent sensor errors, the variance of the parameter, P_i

$$\langle P_i^2 \rangle = \sum_j \left(B_{ij}^2 \langle G_j^2 \rangle \right) \quad .$$

We now proceed to the modeling details.

The surface of the primary mirror is given by

$$Z = \frac{x^2 + y^2}{2R}$$

where R is the radius of mirror curvature. The z axis lies along the optical axis with the origin at the vertex. We define unit vectors $\vec{i}$, $\vec{j}$, $\vec{k}$ to lie in the s, y, z directions respectively.

A segment is centered at (x_o, y_o). Three reference points are located at $(x_o + p_n, y_o + q_n)$ $(n = 1,2,3)$ in a reference plane tangent to the segment center. Measurement of reference point positions by the single axis OPS-LPS

constitute the input data. Output data consists of complete knowledge of the position of the reference plane (one per segment). Henceforth the subscripts of (x_o, y_o) will be suppressed since we are dealing with only a single segment; alignment of other segments will be treated by the same techniques.

Segments are assumed to be rigid bodies; they do not warp or expand.

The unit normal to the segment center is

$$\vec{N} \equiv \vec{N}(x,y) = \frac{1}{|\vec{N}|} \left(-\frac{x}{R}\,i - \frac{Y}{R}\vec{j} + \vec{k}\right)$$

The vector from the segment center to the reference points in the reference plane is

$$\vec{U}_n \equiv \vec{U}(x,y,p_n,q_n) = p_n\vec{i} + q_n\vec{j} + \frac{xp_n + yq_n}{R}\vec{k}$$

Vector $\vec{U}_n$ is defined by the condition (since $\vec{U}_n$ as in the reference plane)

$$\vec{N} \cdot \vec{U}_n = 0$$

The vector from the prime focus to the subaperture center is

$$M_o \equiv \vec{M}_o(x,y) = x\vec{i} + y\vec{j} - \frac{R^2 - (x^2 + y^2)}{2R}\vec{k} \quad .$$

The vector from the prime focus to the nth reference point is

$$M_n \equiv M_n(x,y,p_n,q_n) = \vec{M}_o + \vec{U}_n$$

In the absence of misalignment, the measurement of the vector to the reference points made by the single axis OPS-LPS is called $\vec{M}_n$. The definition of the misalignment vector, $\vec{\Delta}$ follows.

Piston Error, S. Piston error is segment error displacement along the normal. The misalignment vector due to piston error is $\vec{S} = S\vec{N}$, where S is the piston error parameter.

Out of Plane Tilt Error, ϕ_S, ϕ_T. Tilt of the reference plane by ϕ_S perpendicular to the plane of incidence (i.e., about a unit rotation vector axis which is both in the reference plane and perpendicular to the plane of incidence) clockwise looking along the rotation vector is called Sagittal Tilt. The misalignment vector is

$$\vec{\phi}_{sn} = \phi_S \left[\frac{\vec{N} \times \vec{k}}{|\vec{N} \times \vec{k}|}\right] \times \vec{U}_n \quad ,$$

where ϕ_S is the misalignment parameter, and "x" denotes a cross product.

Tilt of the reference plane by ϕ_T in the plane of incidence (i.e., about a unit rotation vector which is both in the reference plane and in the plane of incidence) clockwise looking along the rotation vector is called Tangential Tilt. The misalignment vector is

$$\vec{\phi}_{Tn} = \phi_T \left[\frac{(\vec{N} \times \vec{k}) \times \vec{N}}{|(\vec{N} \times \vec{k})|} \right] \times \vec{U}_n \quad ,$$

where ϕ_T is the misalignment parameter.

In Plane Segment Rotation, α. In plane rotation is rotation of the reference plane about the segment center normal by α. The rotation is positive if the segment turns clockwise as seen looking along $\vec{N}$. The misalignment vector is

$$\vec{\alpha}_n = \alpha \{ \vec{N} \times \vec{U}_n \}$$

where α is the misalignment parameter.

In Plane Displacement, , . In plane sagittal displacement is displacement of the reference plane in a direction perpendicular to the plane of incidence (i.e., along the unit sagittal rotation vector). The misalignment vector is

$$\vec{\varepsilon}_S = \varepsilon_S \left[\frac{\vec{N} \times \vec{k}}{|\vec{N} \times \vec{k}|} \right]$$

where ε_S is the misalignment parameter. As defined, this is motion in the clockwise direction about the vertex as seen when looking along the $\vec{k}$ vector.

In plane tangential rotation is displacement of the reference plane away from the vertex (along the tangential vector). The misalignment vector is

$$\vec{\varepsilon}_T = \varepsilon_T \frac{(\vec{N} \times \vec{k}) \times \vec{N}}{(\vec{N} \times \vec{k})}$$

where ε_T is the misalignment parameter.

Alignment System Measurement Characteristics. The single axis OPS-LPS measures the vector $\vec{M}_n + \vec{\Delta}_n$ from the prime focus to each reference point.

The misalignment vectors defined above are summed to form $\vec{\Delta}$. This vector gives the displacement of the nth reference point due to the misalignment parameters; i.e.

$$\vec{\Delta}_n = S\vec{N} + \vec{\phi}_{sn} + \vec{\phi}_{Tn} + \vec{\alpha}_n + \vec{\varepsilon}_S + \vec{\varepsilon}_T \quad .$$

The first three terms are out of plane motion (i.e. along $\vec{N}$); the second three terms are nearly inplane motion.

The vector $\vec{M}_n + \vec{\Delta}_n$, resolved into range and cross range components is measured by the OPS and LPS. The OPS measures the length of $M_n + \Delta_n$

$$|\vec{M}_n + \vec{\Delta}_n| \approx |M_n| \left\{ 1 + \frac{\vec{\Delta}_n \cdot \vec{M}_n}{\vec{M}_n \cdot \vec{M}_n} \right\}$$

where terms on the order of $\vec{\Delta} \cdot \vec{\Delta}$ have been omitted. Three such measurements are provided. The quantitites

$$\frac{\vec{\Delta}_n \cdot \vec{M}_n}{|\vec{M}_n|} = |\vec{M}_n + \vec{\Delta}_n| - |\vec{M}_n| = (OPS)_n$$

are linear in the misalignment parameters and provide three equations in six unknowns.

The cross range measurements made by the LPS system are in two orthogonal directions and are best characterized by angular deviations in the radial and cross radial (sagittal) direction. The unit vector in the cross radial direction is

$$\vec{M}_{sn} = \frac{(\vec{M}_n + \vec{\Delta}_n) \times \vec{k}}{|(\vec{M}_n + \vec{\Delta}_n) \times \vec{k}|} \approx \frac{\vec{M}_n \times \vec{k}}{|\vec{M}_n \times \vec{k}|}$$

The angular deviations are

$$(LPS)_{sn} = \frac{\vec{\Delta}_n \cdot \vec{M}_{sn}}{|\vec{M}_n|}$$

providing three more equations in six unknowns.

Likewise, the unit vector in the radial (tangential) direction is

$$\vec{M}_{Tn} = \frac{\vec{M}_{sn} \times \vec{M}_n}{|\vec{M}_{sn} \times \vec{M}_n|}$$

The angular deviations are

$$(LPS)_{Tn} = \frac{\vec{\Delta}_n \cdot \vec{M}_{Tn}}{|\vec{M}_n|}$$

providing three more equations in six unknowns. Totaled, there are nine linear equations in six unknowns as given below

$$\vec{\Delta}_n \cdot \frac{\vec{M}_n}{|\vec{M}_n|} = (OPS)_n \qquad n = 1, 2, 3$$

$$\vec{\Delta}_n \cdot \frac{\vec{M}_{sn}}{|\vec{M}_n|} = (LPS)_{sn} \qquad n = 1, 2, 3$$

$$\vec{\Delta}_n \cdot \frac{\vec{M}_{Tn}}{|\vec{M}_n|} = (LPS)_{Tn} \qquad n = 1, 2, 3$$

These nine equations solved as outlined above yield under rigid body constraints, the various misalignment parameters denoting the segment misalignment from its ideal position established during alignment calibrations. Since the system geometry is contained in $\vec{M}_n$ and $\vec{\Delta}_n$ (exclusive of the parameters), the inversion process need be performed only once. Thereafter, the misalignment parameters can be expressed as the sum of nine products of which the measured quantity is one component. This increases the speed of the algorithm.

Each segment may be treated as outlined above. There will be combinations of misalignment parameters from segment to segment which indicate a displacement of the alignment sensor rather than the segments. If necessary these "coherent" displacements may be extracted from the data prior to control system input.

For small misalignments, the wavefront error introduced by one type of misalignment may be nearly cancelled by a second misalingment. For example, a sagital segment out of plane tilt can nearly cancel the aberration from a tangential segment inplane translation. Hence, is is probably sufficient to control only segment out of plane tilt and piston error and assume that the segment inplane motions are small enough so that residual errors from correction of one misalignment by another are negligible.

The errors in measurement of reference plane position are given below in terms of sensor measurement noise. Variance of the misalignment parameter in terms of sensor measurement noise are presented and random errors are assumed. The parameter θ is the angle of incidence of the incident ray to segment normal.

$$\langle S^2 \rangle = \langle \phi_s^2 \rangle = \langle \phi_T^2 \rangle = \cos^2\theta \langle \delta(OPS)^2 \rangle + \sin^2\theta \langle \delta(LPS)^2 \rangle_T;$$

$$\langle \varepsilon_T^2 \rangle = \sin^2\theta \langle \delta(OPS)^2 \rangle + \cos^2\theta \langle \delta(LPS)^2 \rangle_T;$$

$$\langle \varepsilon_s^2 \rangle = \langle \delta(LPS)^2 \rangle_s;$$

where $\langle\delta(OPS)^2\rangle$, $\langle\delta(LPS)^2\rangle_T$ and $\langle\delta(LPS)^2\rangle$ are the measurement variances of the OPS, tangential LPS and sagittal LPS, respectively.

F. Reference Plane Position Measurement: OPS Triangulation

The preceding section has outlined the technique as applied to the Single Axis Concept. Except for changes in geometry and the different way the misalignment vectors are resolved, the results apply to OPS triangulation as shown in the paragraphs to follow.

The OPS triangulation concept consists of several OPS source points symmetrically located about the optical axis in the plane of the prime focus. No LPS is used. Location of each reference point is accomplished by range measurements only.

The first item to be determined is how many source points are required. One source point is not sufficient (except if it is located at the center of curvature of a spherical mirror) since the alignment system could not detect segment rotation about the source point. It can be shown by similar arguments and by reference to Figure C.3 that a two source OPS triangulation concept cannot provide an accurate measurement of the position of a reference point along a particular vector (a function of reference point-alignment system geometry). Therefore, the system to be modeled next will be a three source OPS triangulation concept shown in Figure C.2.

Before the modeling specifics are addressed, the accuracy of the two source OPS triangulation concept in the most favorable direction - RP displacement in the plane containing the OPS source points is derived.

Displacement of the nth RP in the incident plane is resolved into inplane ($\perp$ to $\vec{N}$) and out of plane ($\parallel$ to $\vec{N}$) displacements. Let these component displacements be S and ε_T respectively.

The question is how well can the two source OPS triangulation concept resolve $\vec{\Delta}_n$ into the appropriate components.

The two OPS measurements can provide ($\vec{r}_{ic}$ is the expected distance for an aligned system)

$$(OPS)_1 = |\vec{r}_1| - |\vec{r}_{1c}| = -S\cos\theta_1 + \varepsilon_T \sin\theta_1$$

$$(OPS)_2 = |\vec{r}_2| - |\vec{r}_{2c}| = -S\cos\theta_2 + \varepsilon_T \sin\theta_2$$

Hence

$$S = \frac{(OPS)_2 \sin\theta_1 - (OPS)_1 . \sin\theta_2}{\sin(\theta_2 - \theta_1)}$$

If the OPS sources are separated from the optical axis by $\pm L$ and are in the plane F meters from the primary vertex and perpendicular to the optical axis

$$S \approx \frac{(OPS)_2 \sin \theta_1 - (OPS)_1 \sin \theta_2}{\sin (2\frac{L}{F} \cos 2\theta)}$$

where $\theta = (\theta_1 + \theta_2)/2$. The variance in S is

$$\langle S^2 \rangle = \frac{\langle (OPS)_1^2 \rangle \sin^2 \theta_2 + \langle (OPS)_2^2 \rangle \sin^2 \theta_1}{\sin^2(\frac{2L}{F} \cos 2\theta)}$$

For L = 0.5 m, F = 10 m, $\theta = 10^o$, and $\langle (OPS)^2 \rangle^{\frac{1}{2}} = 0.01$ μm, $\theta_1 = 7.3^o$, $\theta_2 = 12.7^o$ and $\langle S^2 \rangle^{\frac{1}{2}} \approx 0.027$ μm.

This shows that for the above parameters the measurement error of piston displacement is approximately three times the sensor measurement error. This is due to the fact that the OPS measurements are not along $\vec{N}$.

A similar analysis furnishes ε_T and its variance

$$\langle \varepsilon_T 2 \rangle = \frac{\langle (OPS)_1^2 \rangle \cos^2 \theta_2 + \langle (OPS)_2^2 \rangle \cos^2 \theta_1}{\sin^2(\frac{2L}{F} \cos 2\theta)}$$

which for the above parameters yield

$$\langle (\delta \varepsilon_T)^2 \rangle^{\frac{1}{2}} = 0.15 \text{ μm}$$

Fortunately the tolerance to inplane displacement is greater than tolerance to piston error. A more detailed analysis of error propagation is provided by the components of the inverted matrix as outlined in the previous section. The specifics of the three source OPS Trilateration concept are now given.

The three source OPS Trilateration Concept shown in Figure C.2 consists of three source points positioned in an equilateral triangle included in a circle of radius L and centered on the projector optical axis. As before, there are three reference points per segment and all reference points are illuminated by all OPS sources.

The vector, $\vec{\Delta}$, describing the misalignment motion of each reference point has been derived previously. This vector is determined by resolving it onto three non orthogonal axes - the vectors from each of the three OPS points.

The measurement of the mth OPS on the nth reference point is denoted by

$$(OPS)_{mm} = \frac{\vec{\Delta}_n \cdot \vec{M}_{mn}}{|\vec{M}_{mn}|} = |\vec{M}_{mn} + \vec{\Delta}_n| - |\vec{M}_{mn}|$$

where $\vec{\Delta}_n$ is the vector motion of the nth RP due to misalignment and

$\vec{M}_{mn}$ is the vector from the mth OPS to the nth reference point in an aligned system

Since m and n = 1,2,3; the system is nine equations in six unknowns and is solved by matrix algebra as indicated in the previous section.

The above technique has been implemented by a computer algorithm. Conversion from measurement parameter to misalignment parameter by a summation of linear terms has been demonstrated.

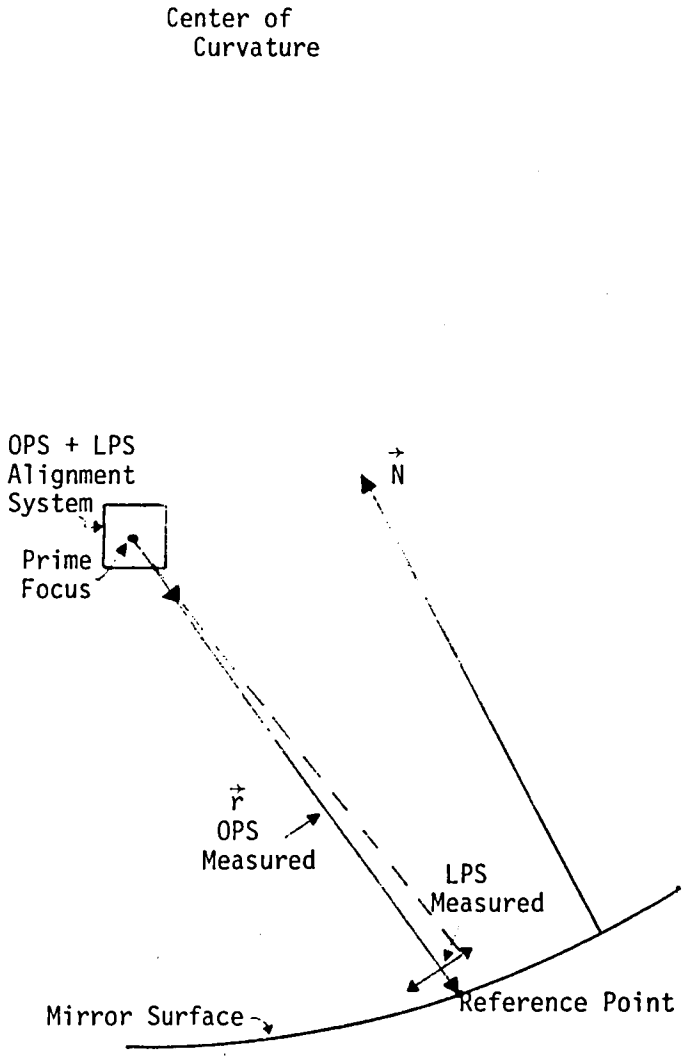

Fig. C.1 Single Axis OPS + LPS Concept

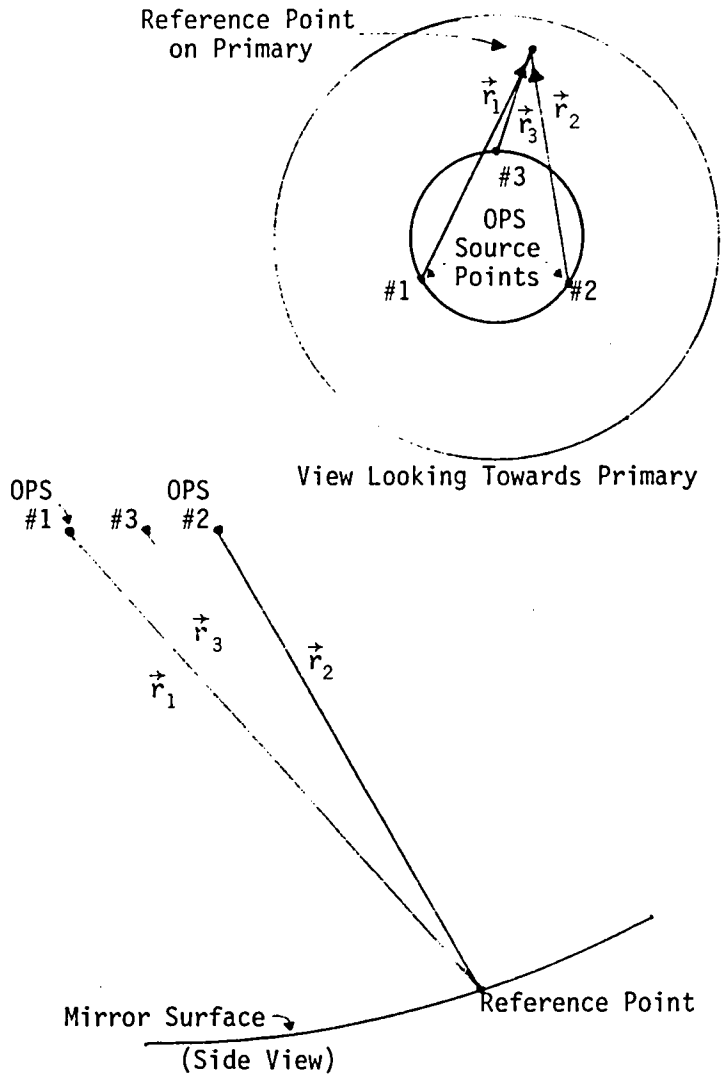

Fig. C.2 OPS Triangulation Concept

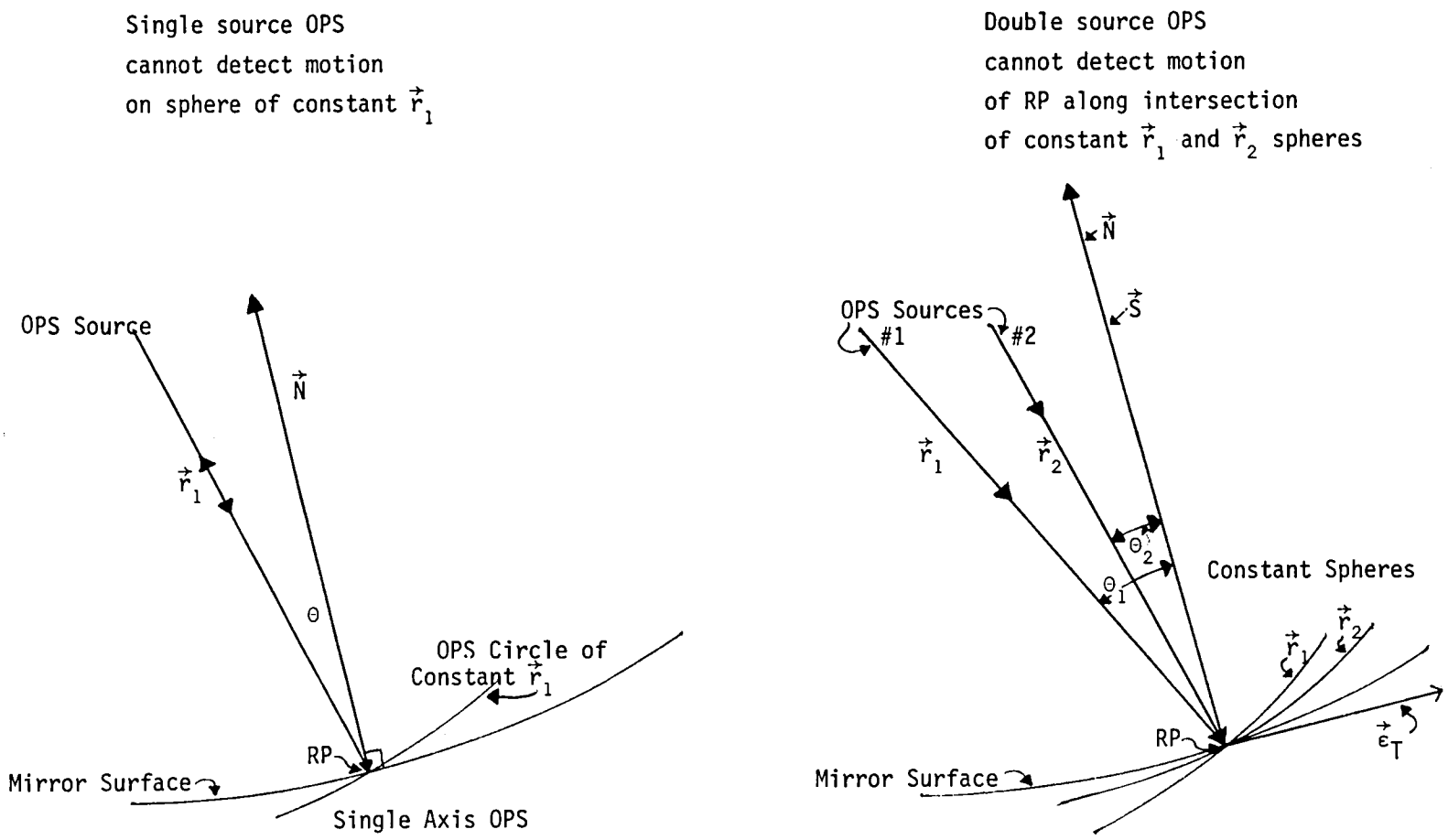

Fig. C.3 OPS Triangulation Measurement Ambiguity

LIGHTWEIGHT SEGMENTED GLASS MIRRORS

For a number of years, Kodak has been successfully involved in the design, fabrication, assembly, and test of complex, high reliability, state-of-the-art, diffraction-limited optical systems. Current and future needs for optical systems extend into the areas of energy, communications, weapons systems, and telescope observation systems. These applications share common needs for lightweight, stable, mirror structures.

The design of a lightweight mirror is governed by three basic features--weight, optical figure and rigidity. Weight is of primary importance in the total system design since launch margins and optical figuring are critical. Weight (mass and moment of inertia) is also a prime driver in the dynamics of slewing, tracking, and dynamic beam control. Rigidity is the relationship between mirror deformation and mirror loadings, and is one of the factors that influences the design of the optical test support and mirror. A systematic trade analysis must be made considering all these factors, thereby providing guidance for selection of mirror substrate dimensions and mounting concepts. The resulting design includes constraints on the mirror by blank manufacturing in a gravity environment, by processing and testing in gravity and acoustic load environments, by launch and by operating in a zero gravity environment. It must be emphasized that the following data is for a simply supported mirror, with no particular mirror mounting arrangement or optical system configuration being considered.

Lightweight glass mirror blanks are currently manufactured for high reliability, diffraction-limited optics using a high temperature, fusion welding process. A "honeycomb" core, a faceplate, and a backplate are separately fabricated, the faceplate is bonded to the plano-plano core, and the whole assembly is inverted and slumped over a form to the desired curvature. In this process, distortions are inevitably introduced into the faceplate, backplate, and core struts. Such distortions can be reduced by preshaping the core and plates before fusion bonding. Since the core and plates must be heated to the softening point, some distortion is unavoidable. The mirror blank must be designed with the mirror blank manufacturing constraints in mind. A typical fusion welded mirror, which was designed, processed, and tested at Kodak, is shown in Figure 1.

Optimizing a simply supported mirror for weight (i.e., solving a simultaneous set of partial derivative equations to determine blank parameters such as core height, core web spacing, core web thickness, etc.) yields a fusion welded mirror design, as shown in Figure 2. An optimized 1.4-meter diameter mirror intended for visible light applications, with an aspect ratio of 7 to 1, would have a simply supported mirror deflection of a few waves. In order to keep the deflection of a 10-meter monolithic mirror to a level of less than 100 waves (at λ = 0.6328 microns) the aspect ratio is forced to 4 to 1, thus causing an "extremely heavy" mirror. The second curve, shown in Figure 2, was calculated for an aspect ratio of 20 to 1, reducing the weight at the expense of the inherent structural rigidity. *(Note: The deflection is approximately 600 waves at 10 meters, which might be tolerated at far IR and microwave operational wavelengths.)*

FUSION-WELDED LIGHTWEIGHT MIRROR

Figure 1

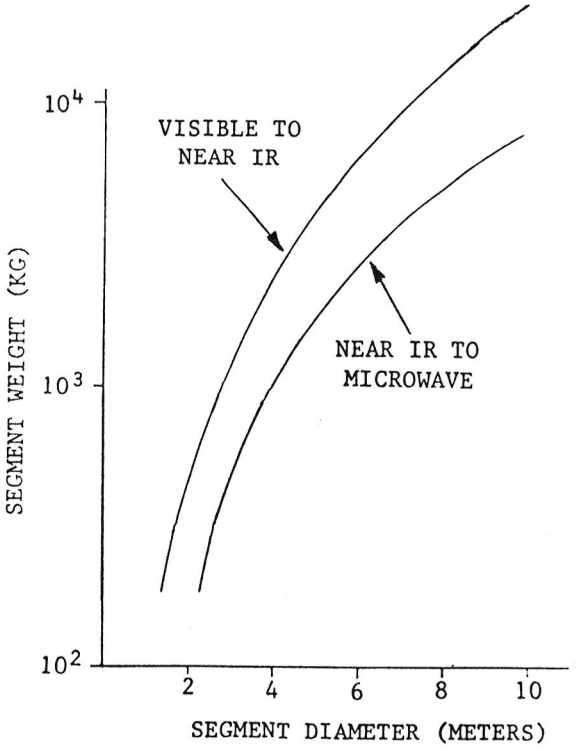

FUSION WELDED LIGHTWEIGHT MIRROR (SEGMENT WEIGHT VS SEGMENT DIAMETER)

Figure 2

If it is assumed that the Large Deployable Reflector is made up of phased segments, each segment can be designed as a separate mirror. The weight of a 10-meter telescope, with mirror segments of a fixed diameter, is shown in Figure 3. The arbitrary lower limit is a telescope made up of sixty-one 1.4-meter diameter mirrors.

A conventional aspect ratio of 7 to 1 yields a reasonable mirror deflection for a near IR operational wavelength. An aspect ratio of 20 to 1 on each segment yields a larger deflection which might be tolerated during manufacture for a microwave operational wavelength. The overall aspect ratio of the 10-meter telescope, using this diameter segment, is about 180 to 1. (The upper limit on these curves is a one segment, 10-meter diameter mirror and should be used for reference purposes only since facility and transportation issues preclude the use of this size segment.)

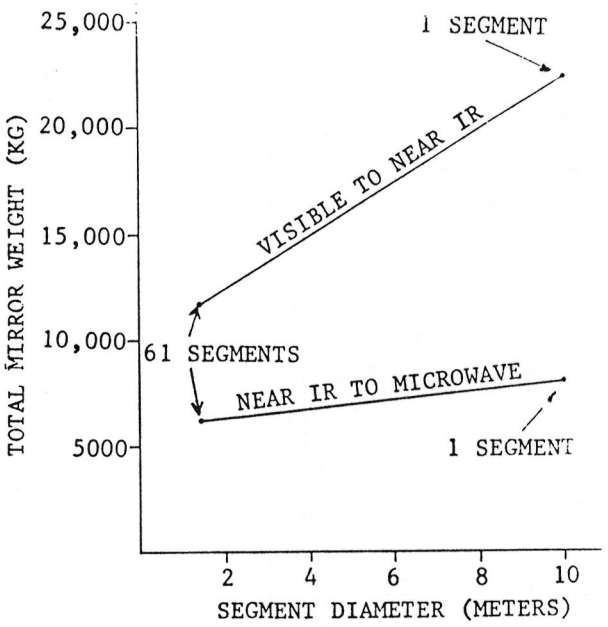

10-METER DIAMETER FUSION WELDED LIGHTWEIGHT MIRROR (MIRROR WEIGHT VS SEGMENT DIAMETER)

Figure 3

The high temperature process to achieve plate-to-core bonding in the fusion-welded mirror places a constraint on the mirror design and, in effect, limits the amount of lightweighting that can be achieved. A manufacturing process called frit bonding avoids the high temperature, fusion welding technique, thus relieving the mirror blank manufacturing weight constraint. In frit bonding the glass mirror blank is manufactured by using a glass adhesive system, eliminating the high temperature fusion step while maintaining the balance of the conventional mirror manufacturing process. In 1978 the 0.5-meter diameter, ULE™, frit-bonded mirror (shown in Figure 4) was designed and polished by Kodak and fabricated by Corning Glass Works as part of a Kodak-funded program.

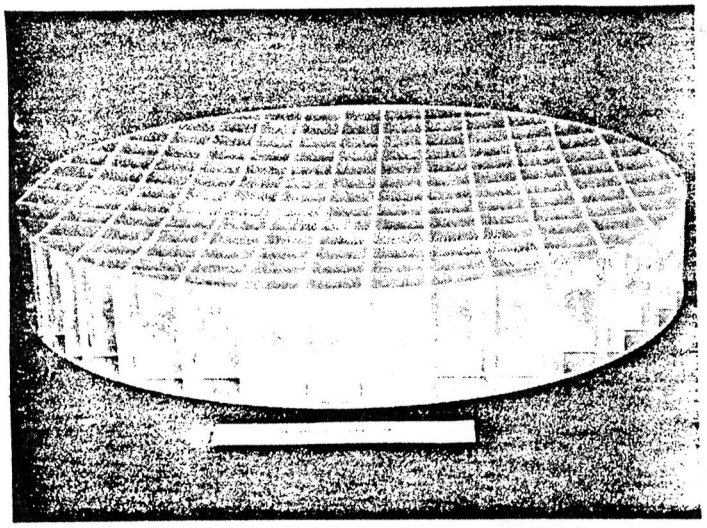

FRIT-BONDED LIGHTWEIGHT MIRROR

Figure 4

Optimizing a simply supported mirror yields a frit-bonded mirror design relationship as shown in Figure 5. The deflection criteria used in Figure 2 have also been used in Figure 5. The weight of a 10-meter, frit-bonded mirror, made up of various size segments, is shown in Figure 6, utilizing the same deflection criteria as Figure 3. Predicted mirror weight area ratios for lightweight glass mirrors are shown in Figure 7. Based on a preliminary analysis of a simply supported, unmounted mirror design, the technology associated with a segmented, frit-bonded mirror is approaching a mirror goal of 25 kg/m^2.

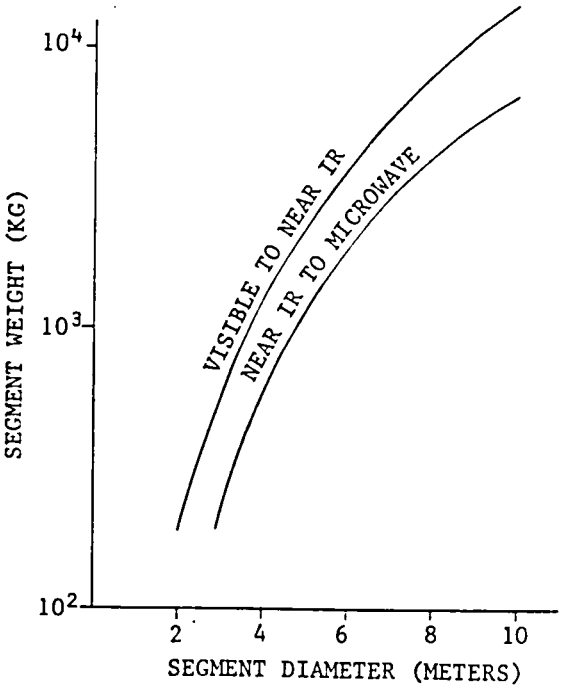

FRIT BONDED LIGHTWEIGHT MIRROR (SEGMENT WEIGHT VS SEGMENT DIAMETER)

Figure 5

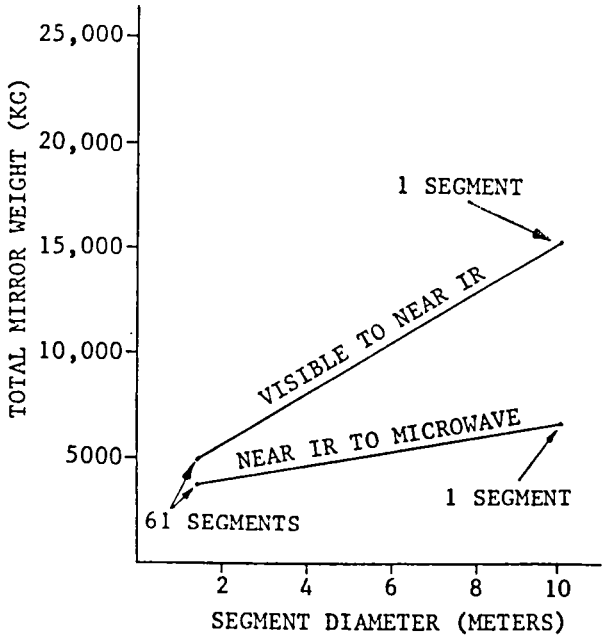

10-METER DIAMETER FRIT BONDED LIGHTWEIGHT MIRROR (MIRROR WEIGHT VS SEGMENT DIAMETER)

Figure 6

Additional work is needed in the following areas to substantiate these preliminary results:

1. Mounted mirror design
2. Segmented mirror fabrication and testing

In addition, studies should be performed to identify methods for phasing and aligning the segments, both in the factory for acceptance testing and on-orbit for operation. Weights associated with the mirror mounting, phasing and aligning equipment should be added to the mirror segment weight in comparing design approaches.

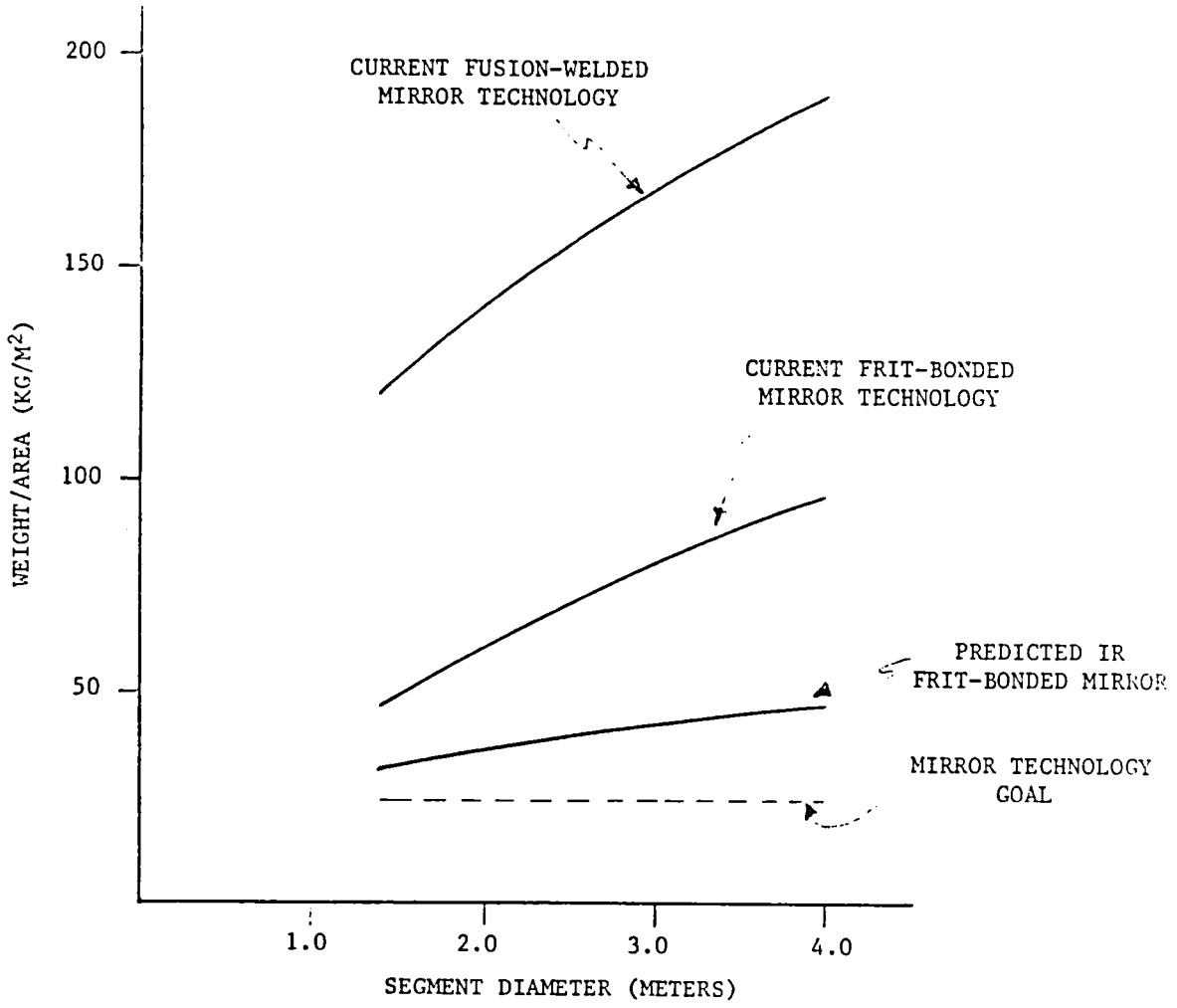

PREDICTED MIRROR WEIGHT/AREA

Figure 7

APPENDIX E

DESIGN CONSIDERATIONS

Problem: What are plausible and practical conceptual designs for LDR sun shades?

Approach: Select shade configurations of simple geometry and relatively easy deployment. Compare relative advantages and disadvantages of these concepts. Estimate weight requirements. Scope the dynamics impact of adding a sun shade on LDR and estimate the associated weight penalty due to additional dynamical control of LDR.

Findings: Simple shade designs are: balloon, umbrella, scoop, and cylinder (extension of the scoop design). Balloon and umbrella can provide shading of the telescope backstructure and the spacecraft in addition to shielding the primary. They must be re-oriented with re-orientation of the telescope. They potentially incur substantial solar torques which must be compensated for (weight penalty for LDR) and provide no shielding from the earth. The scoop is a minimum-area design, and several different deployment options exist, of varying complexity. It provides no earth shielding. The cylinder is considered the most likely LDR shade concept, primarily because it provides some shielding against the earth. This is important for keeping temperature gradients and variations with time low. It provides no backstructure or spacecraft shielding (unless extended below the primary mirror) and has the largest weight. All designs involve no known material or deployment difficulties. The weights are low compared to the total systems weight. Because of the low weight, excitation of low vibration modes of the mirror, which could affect figure control, is unlikely. Solar torques (rotation of the system) can be compensated for by CMGs, and the associated weight penalty is small (less than 1000 lb for a 30 m LDR)

The simplest sun shade is an inflatable plastic (Mylar or Kapton membranes) balloon, which is sized and positioned such that its sun shadow covers the face of the primary mirror. A larger balloon, shown in the figure, can cover the secondary and its support structure, the spacecraft (minus solar panels) and the mirror support structure. Advantages of this concept are simplicity and low weight. Disadvantages are vulnerability to meteoroid penetration and consequent loss of pressure (which can be maintained with a small supply of gas but adds complexity to the system), and large solar torques. The vibration frequencies of the balloon are relatively low, but because of a low overall weight, the effect by coupling these modes to the mirror is unimportant. The minimum balloon diameter is about D/2, where D the primary mirror diameter. This value gives very low total weights for this concept and unimportant solar torque effects. However, it is doubtful, if this concept is used, that the advantage of backstructure and spacecraft shielding will not be utilized. These advantages can be derived from larger balloon diameters giving larger masses and torques.

SUNSHADE CONCEPT I: BALLOON

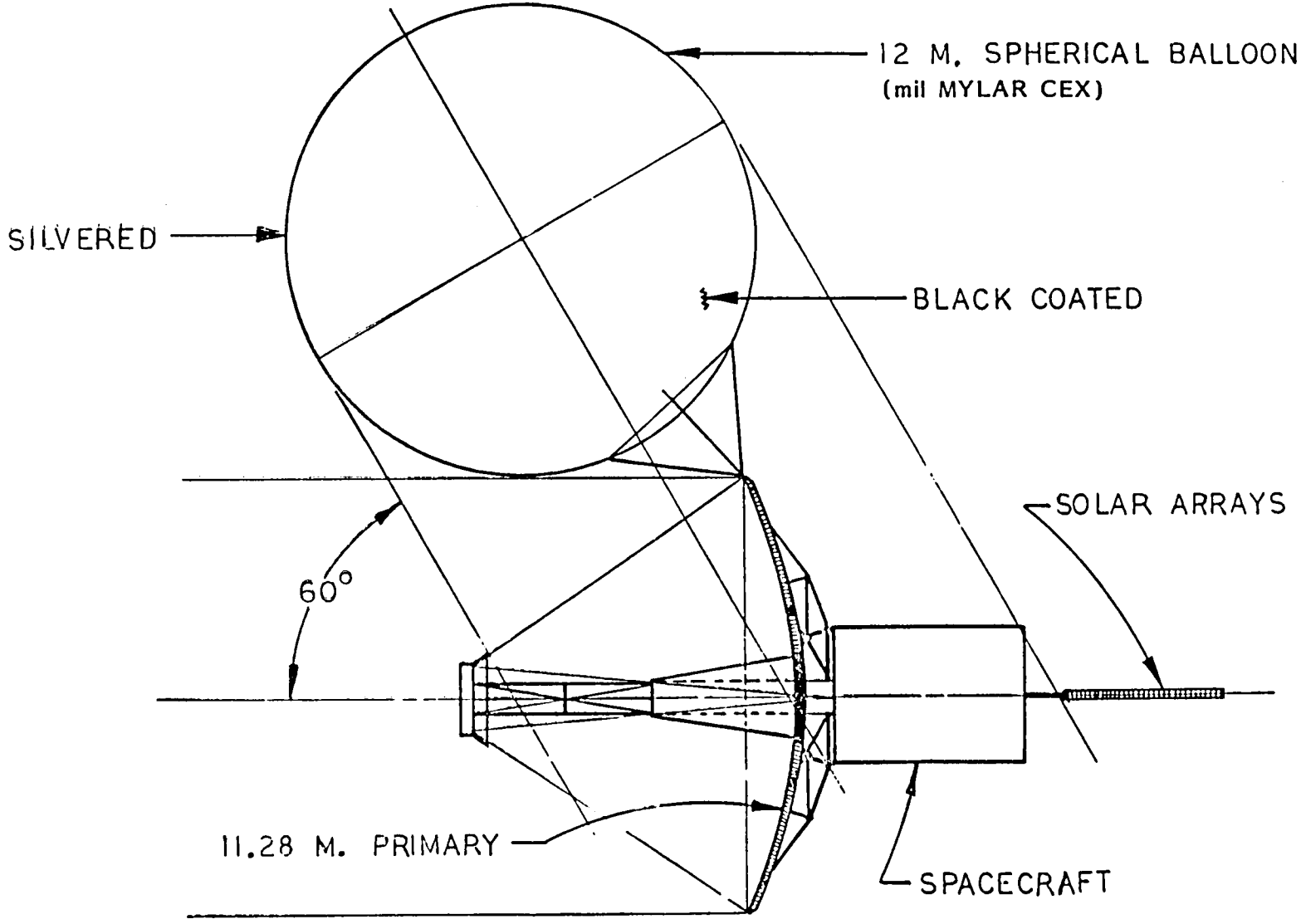

This concept is a large umbrella of conventional design. It involves multiple folding ribs, a central boom structure attached to the outer edge of the primary mirror, and a web of thin plastic (Mylar or Kapton, or other strong, space-compatible materials). As in the case of the balloon, the umbrella orientation must be changed with telescope re-orientation so that its shadow will cover the proper portions of the mirror, spacecraft and secondary support structure. Advantages of the umbrella concept are: simple deployment, non-vulnerability to meteoroid puncture, light weight and smaller area than the balloon. Again, as in case of the balloon, a minimum-size umbrella would cover only the primary mirror, but the advantage in having a lower mass, which is small to begin with, may not be traded against the advantage in additional shielding provided by the larger size shown in the figure. The umbrella is more difficult to store for launch - a disadvantage which becomes more severe the more folding joints are used in a design. The (large) umbrella involves the largest solar torques (tending to rotate the spacecraft in orbit) of all designs, and therefore the largest weight penalty associated with correcting for those torques.

SUNSHADE CONCEPT II: UMBRELLA

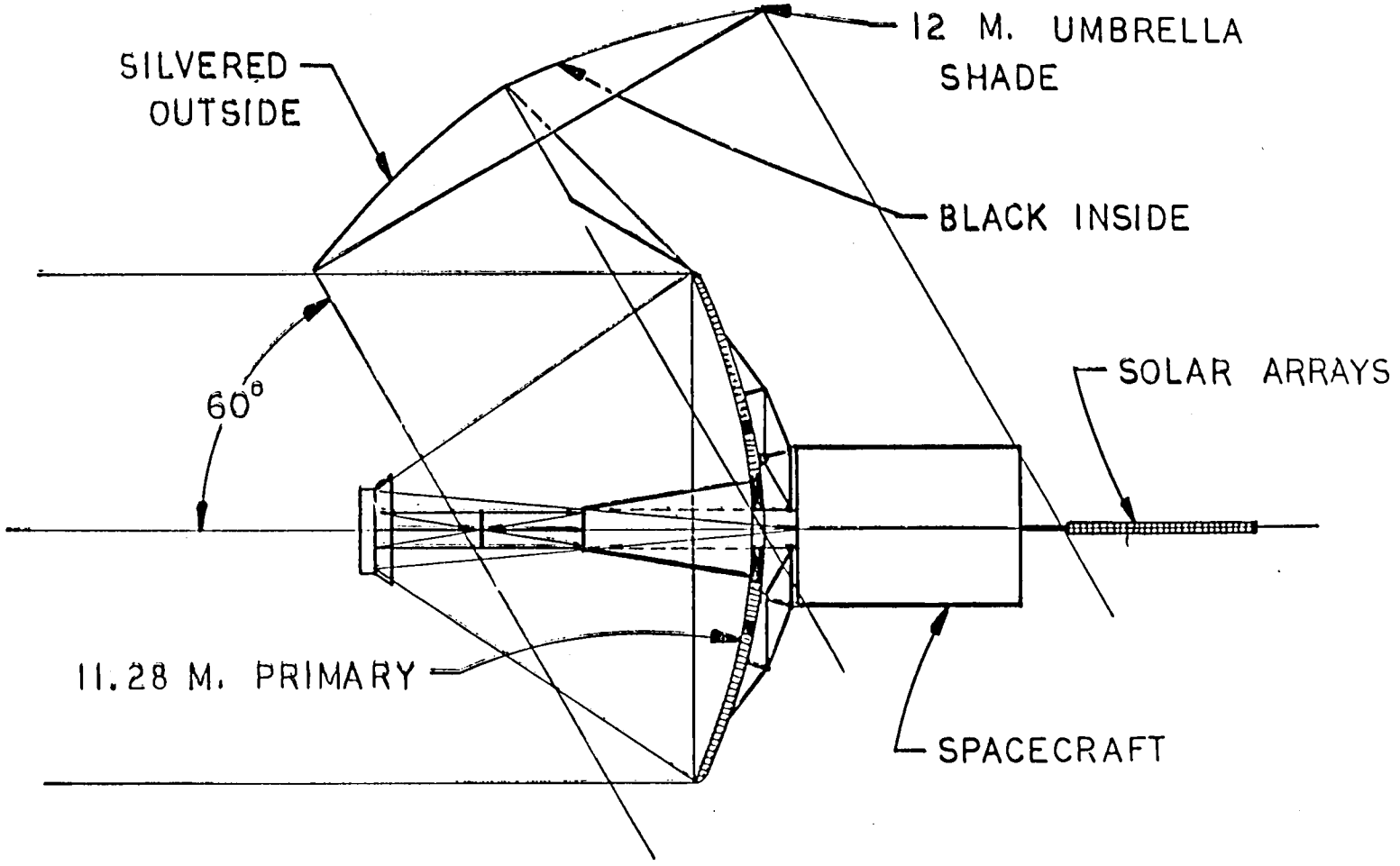

The scoop is a cutaway semi-cylinder which shadows only the primary cylinder. It obtains its name from the resemblence to a sugar scoop when attached to the sunward outer rim of the primary mirror support structure. The shade fabric may be Mylar or Kapton or a thin sheet of Graphite-epoxy (in case of the designs involving rolling it up for stowage), with a number of stiffening and support ribs (also Graphite-epoxy or Graphite-metal). The advantages of the scoop are: minimum surface area and the possible extension around the mirror periphery which results in the conventional barrel-type cylinder sun shade. The barrel provides shielding from the earth as well as from the sun. Shielding from the earth is important since the heat load from the albedo is of the same order as from the sun at a 60^{o} illumination angle. Furthermore, the albedo, for a low earth orbit, varies with time (i.e. over the orbit) due to varying cloud cover and terrain. These variations translate into temperature fluctuations for the mirror which need to be kept at a minimum value. The main disadvantage of the scoop design (and the cylinder or barrel) is the complexity of folding and deploying, whether automatic of sem-automatic.

In the following 3 foils, three different deployment concepts are shown: (i) the roll-out flexrib; (ii) the fold-out hingerib: and (iii) the wrap-around or roll-up.

SUNSHADE CONCEPTS III TO V: SCOOP

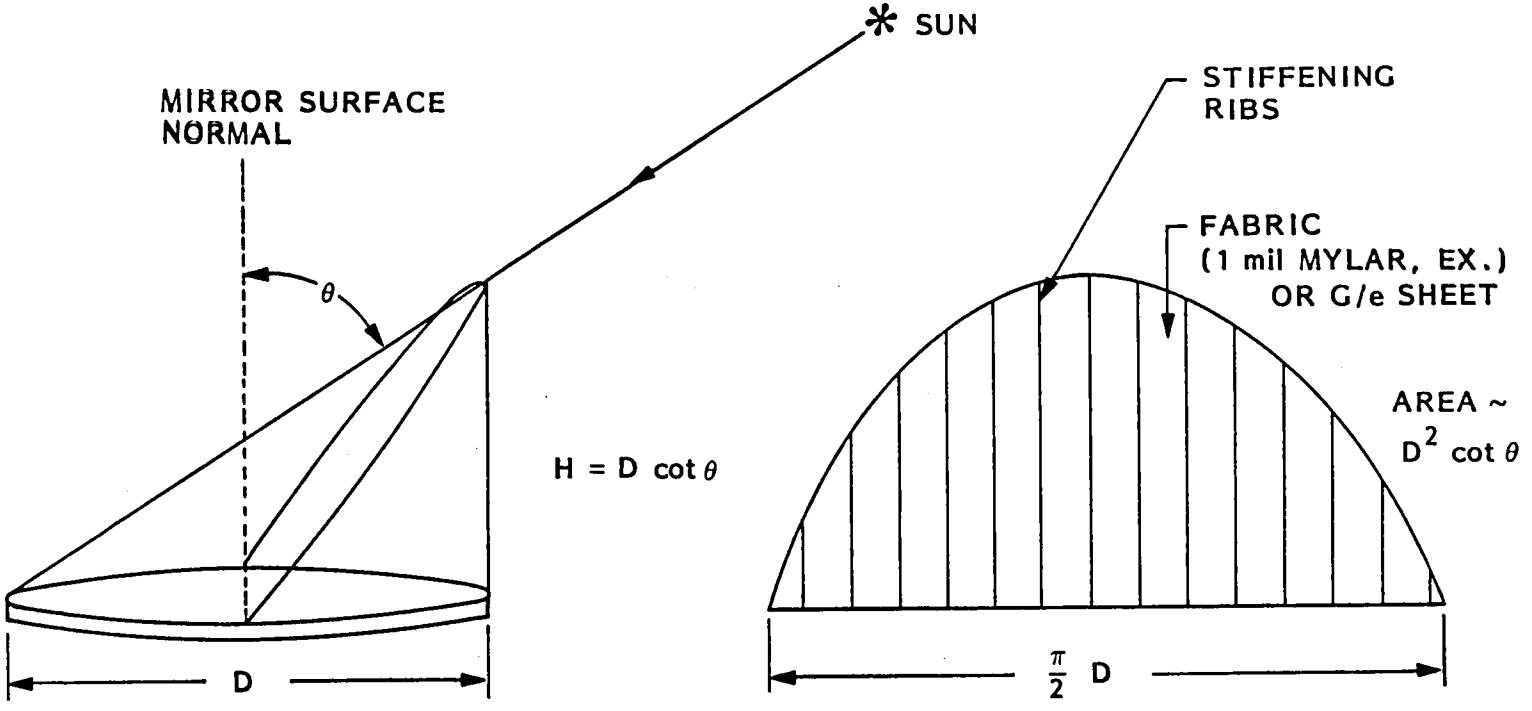

In the stowed configuration, the roll-out scoop is rolled up inside a cylindrical cannister positioned at the edge of one of the primary mirror segments. Longitudonal deployed stiffness is derived from the curvature of the outer edge of the primary mirror segments. The ribs are made of thin metal resembling "stem" masts or large-scale versions of the familiar pull rule steel tape, and they are stowed on spools in the same canister as the shade material (Mylar or Kapton web). The sunshade is deployed as a unit using spring motors or electric drives.

SUNSHADE CONCEPT III: SCOOP (ROLL-OUT)

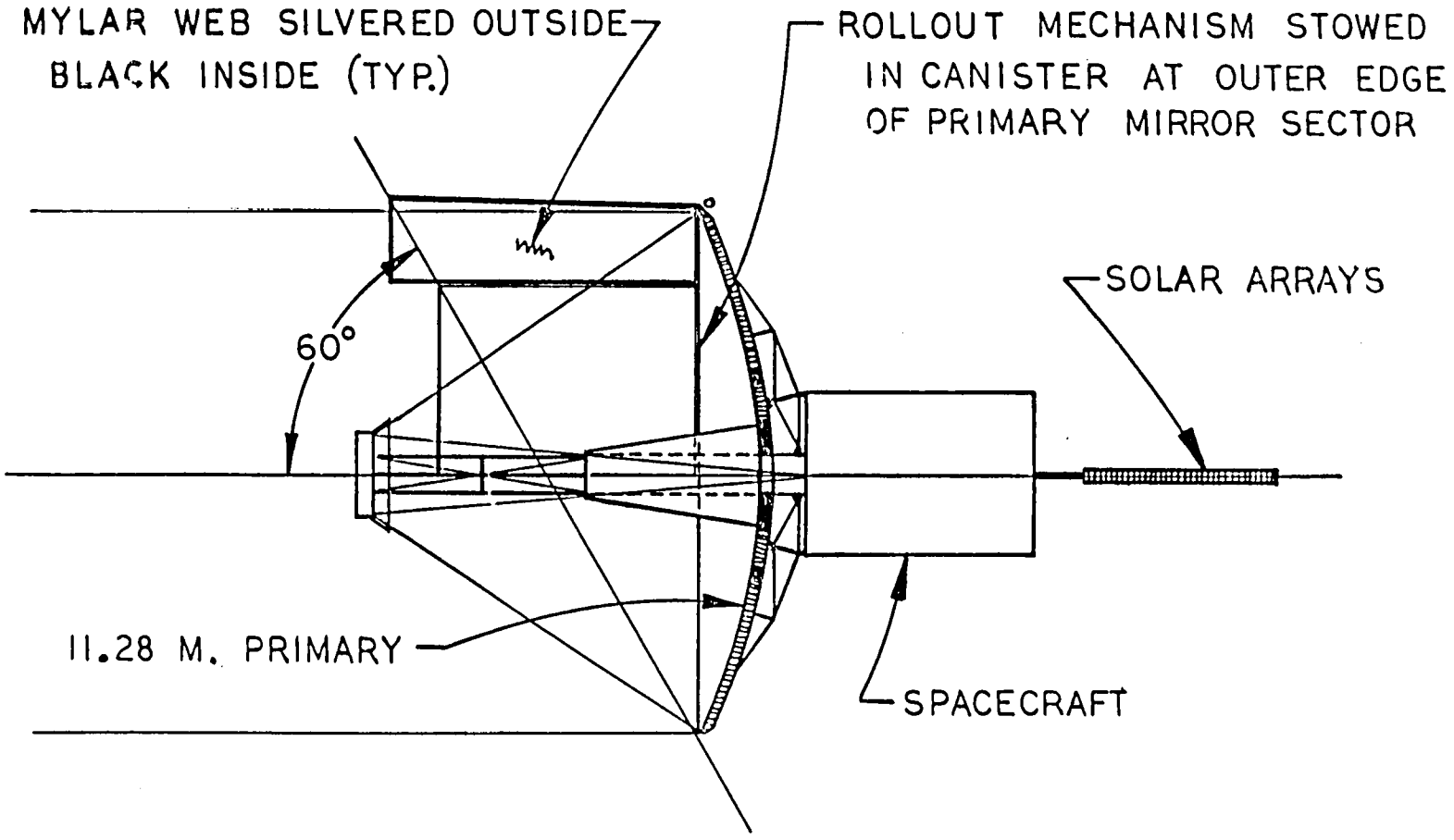

In this scoop concept no canister is used. The ribs are rigid (except for folds) and for stowage fold against the faces of the primary mirror segments, on which they are mounted.

SUNSHADE CONCEPT IV: SCOOP (FOLD-OUT)

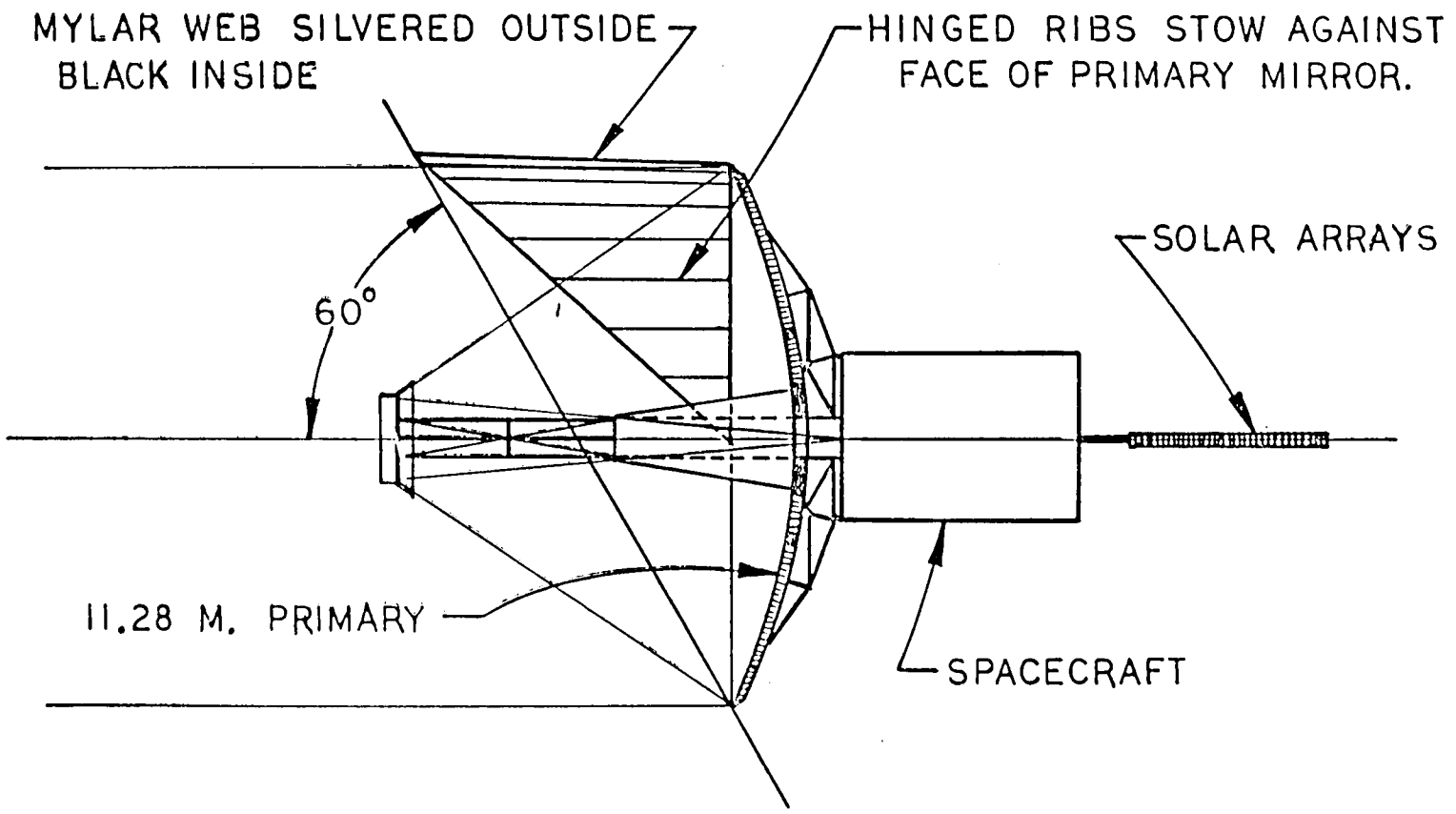

For this concept a more rigid plastic or thin metal web is used with or without longitudonal ribs, depending on the web thickness and its inherent stiffness. The web rolls up into the longitudonal direction relative to the optical axis. For stowage the entire roll is hinged so that it lies alongside the folded primary mirror segments in the STS bay. Deployment is accomplished by hinging the roll-out to its proper longitudonal position and then unrolling it around the periphery of the primary mirror, using cords or some similar means of actuation.

SUNSHADE CONCEPT V: SCOOP (ROLL-UP)

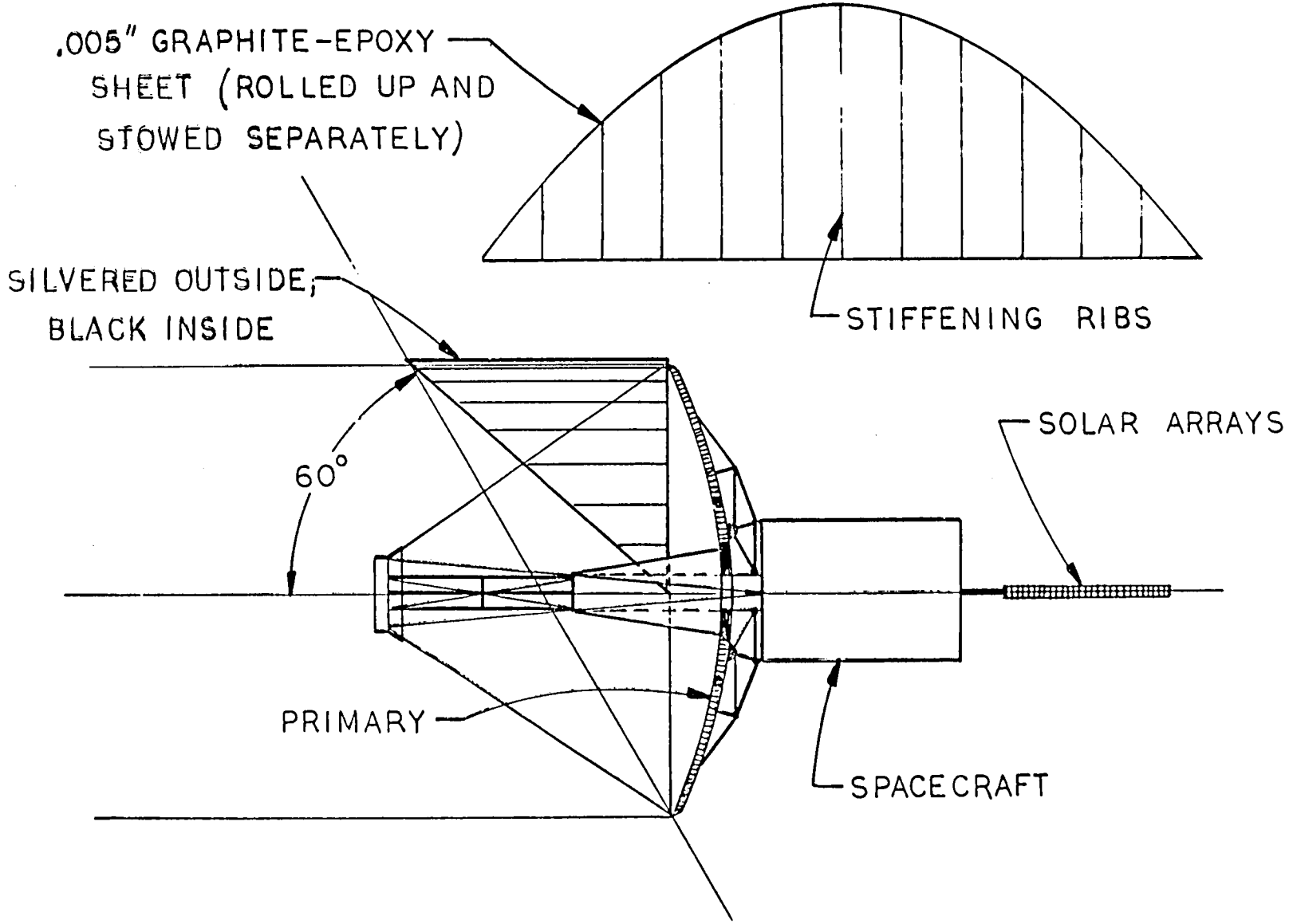

This foil is self-explanatory. The balloon and umbrella diameters were chosen for some spacecraft and backup structure (and secondary mirror and support structure) shielding rather than their minimum values (applicable to shielding of the primary only, for 60° solar incidence relative to the mirror normal), which would be smaller by a factor 2, hence the surface area smaller by a factor 4. The total weights for the two concepts would be, if only shielding of the primary is required, even smaller than given in the table. Since also the solar torque is reduced (next foil) and the therewith associated weight penalty, the balloon and umbrella concept would therefore be associated with the smallest overall weights.

The numbers in parentheses in the last column of entries refer to a graphite/epoxy fabric.

WEIGHT ESTIMATES – 11 M LDR

SUNSHADE TYPE	SURFACE AREA (m^2)	WEIGHTS (kg)			
		FABRIC		SUPPORT AND MECHANISMS	TOTAL*
		1 mil MYLAR	5 mil Gr/e		
BALLOON	πD^2	23	NA	15**	38
UMBRELLA	$\pi D^2/4$	6	NA	20	26
SCOOP	$D^2/1.7$	4	(20)	20	24 (40)
CYLINDER	$\pi D^2/1.7$	12	(48)'	40	52(88)

* MECHANISMS FOR DYNAMIC EFFECTS COMPENSATION MUST BE ADDED TO ABOVE (CF. NEXT FOIL)

** INCLUDES GAS AND VENTING MECHANISM

Atmospheric drag depends on spacecraft altitude, configuration and attitude. For a circular, minimum inclination orbit at 400 n.mi. altitude, the drag per cross-sectional area is about 10^{-9} lb/ft^2, depending on solar conditions. For a 12-m diameter sunshade facing in the flight direction, the resulting force is about 10^{-6} lb, about a factor 200 lower than the force due to solar radiation pressure. Hence the torque on the satellite (trying to rotate it about the center of mass) may be neglected compared with the solar-induced torque discussed below. The atmospheric drag on the satellite (tending to slow it) is increased by about a factor 2 by adding a sun shade (maximum factor). At the nominal altitude of LDR the required adjustment in initial orbit is, however, quite small, since the atmospheric density decreases very rapidly with increasing altitude.

Solar radiation pressure on a silvered sun-facing surface (assumed flat) is about 2×10^{-7} lb/ft^2 For a 12-m diameter surface the resulting force is about 2×10^{-4} lb (for a spherical surface a factor 2 lower). The typical center-of-mass offset for LDR (i.e. the torque arm) is about 2 ft nominally, giving a torque of 5×10^{-4} lb.ft., and for a 1/4 orbit the torque results in an angular momentum change of 0.7 lb.ft.sec. For LDR, the change is non-cyclical i.e. does not reverse during the orbit, and it results in a total change J = 20 lb.ft.sec. per day. This change is non-trivial and must be compensated for. Over a period of 2 years (re-furbishing interval of LDR), a total of 15,000 ft.lb.sec must be compensated for at most. The compensation can be done using the CMGs, which must be unloaded periodically, or using gas jets or magnetic torquers. If hydrazine jets are used, and if a nominal torque arm of 15 ft is used, the required amount of hydrazine is about 5 lb. We add a safety factor of 3 and a factor of 2 for the deployment mechanism, thus giving a total weight penalty of about 30 lb, certainly less than 50 lb. (Cold gas, with a much lower specific impulse than hydrazine, gives a penalty about 4 times larger). These penalties scale approximately with the square of the mirror diameter. The penalty for a 30 m LDR would thus be less than 500 lb. - If magnetic torquers are used to unload the CMGs, the weight penalty is about the same.

SUNSHADE: DYNAMICS EFFECTS

- VIBRATION
  - LOW NATURAL FREQUENCY
  - LOW MASS
  - INSIGNIFICANT INPUT TO TELESCOPE STRUCTURE
- ATMOSPHERIC DRAG
  - MAY DOUBLE
  - ADJUSTMENT IN ORBITAL ALTITUDE SMALL AT 700 + km
- ATMOSPHERIC TORQUE
  - SMALL COMPARED WITH SOLAR
  - TYPICALLY CYCLICAL
- SOLAR TORQUE (RADIATION PRESSURE)
  - TYPICALLY NONCYCLICAL, MUST BE COMPENSATED FOR (CMGs)
  - $\Delta G \approx 20$ lb. ft.s/day FOR 11 m LDR
  - UNLOAD CMGs WITH GAS JETS OR MAGNETIC TORQUERS
  - WEIGHT PENALTY ~ 50 + lb FOR 11 m LDR
    ~ 500 - lb FOR 30 m LDR

THERMAL BENEFITS

Problem: To which extent does adding a sun shade to LDR help controlling thermal gradients and their time variations across and through the primary mirror? Are contraints on mirror segment design relaxed by the sun shade so that, for example, a light-weight ALuminum mirror can work at much lower wavelengths than 500 μm (original estimate for without a sun shade; maximum sun soak) and thus become a viable LDR concept?

Approach: Thermal deformation calculations carried out earlier in the study were made for worst-case steady state sun-soak, ignoring radiation transfer effects and also orbiting "smoothing" effects. Consider these first. If effects due to radiation transfer or smoothing are significant, carry out thermal calculations for a "dynamical " case: calculate temperature gradients across and through the mirror and time variations for a specific mirror model of an LDR mirror. Estimate reduction in thermal bending as a consequence of adding a sun shade.

Findings: Radiation transfer effects inside the mirror core are significant only for glass segments, not Alumnimum. Orbital "smoothing" also is significant only for glass. For Aluminum mirrors, therefore, the only reduction in gradients and their time-variations, derives from the reduced heat loads and the reduced variations in heat loads. Calculations for a 20 m diameter, F/0.5 mirror, with total segment height 10 cm, a mass/area ratio of 20 kg/m^2, gives reductions in thermal gradients, for a 20 m long cylindrical sun shade, across the mirror of a factor 5 to 10, and a maximum temperature difference of less than 10 ^{o}K. Orbital variations of surface temperature are reduced by factors greater than 2 (at worst), and the thermal distortion (due to reduction in the front-to-back temperature gradient by about a factor 6. This would set the minimum operational wavelength of the aluminum mirror at about 100 μm.

Thermal bending of a mirror segment is roughly proportional to the front-to-back temperature difference. The difference is smaller if, in addition to heat conduction, heat transfer by radiation is operative, as is possible with mirrors with a hollowed-out core (core cells). We assume that the walls are perfectly reflecting (they are silvered). In the steady state case where all radiation absorbed by the front of the mirror is radiated by the back, and there is no heat input to the back (optimum case), then for heat transfer by radiation

$$T_f - T_b = (\sqrt{2} - 1)\ T_b$$

while for conduction

$$T_f - T_b = Qhr/\kappa$$

where Q the absorbed heat rate (W/m^2), h the mirror total thickness, κ the thermal conductivity of the mirror material, and r the ratio of cross sectional area: mirror surface:mirror core:

$$r = \frac{(m/A)/(\rho\, h) - 2t/h}{1 - 2t/h}$$

m/A the mass/area ratio of the segments, ρ the density of mirror material, t the front and back plate thickness. For sun soak at 60^o to the mirror surface normal, and 5% absorption, $Q=37.5\ W/m^2$, and $T_b=160\ ^oK$. The next two foils give the values of $\Delta T = T_f - T_b$ for Aluminum and ULE, respectively, and for m/A = 20 kg/m^2 and 45 kg/m^2, and a mirror segment height of 10 cm - all values used in earlier LDR thermal calculations. ΔT is plotted against t/h. Increasing this ratio increases the plate thickness and decreases the amount of material in the core, thereby reducing conduction through the core. In both cases, Aluminum and ULE, orbital effects are ignored. The calculations are for steady sun-soak (37.5 W/m^2 absorbed).

FRONT-TO-BACK TEMPERATURE DIFFERENCE

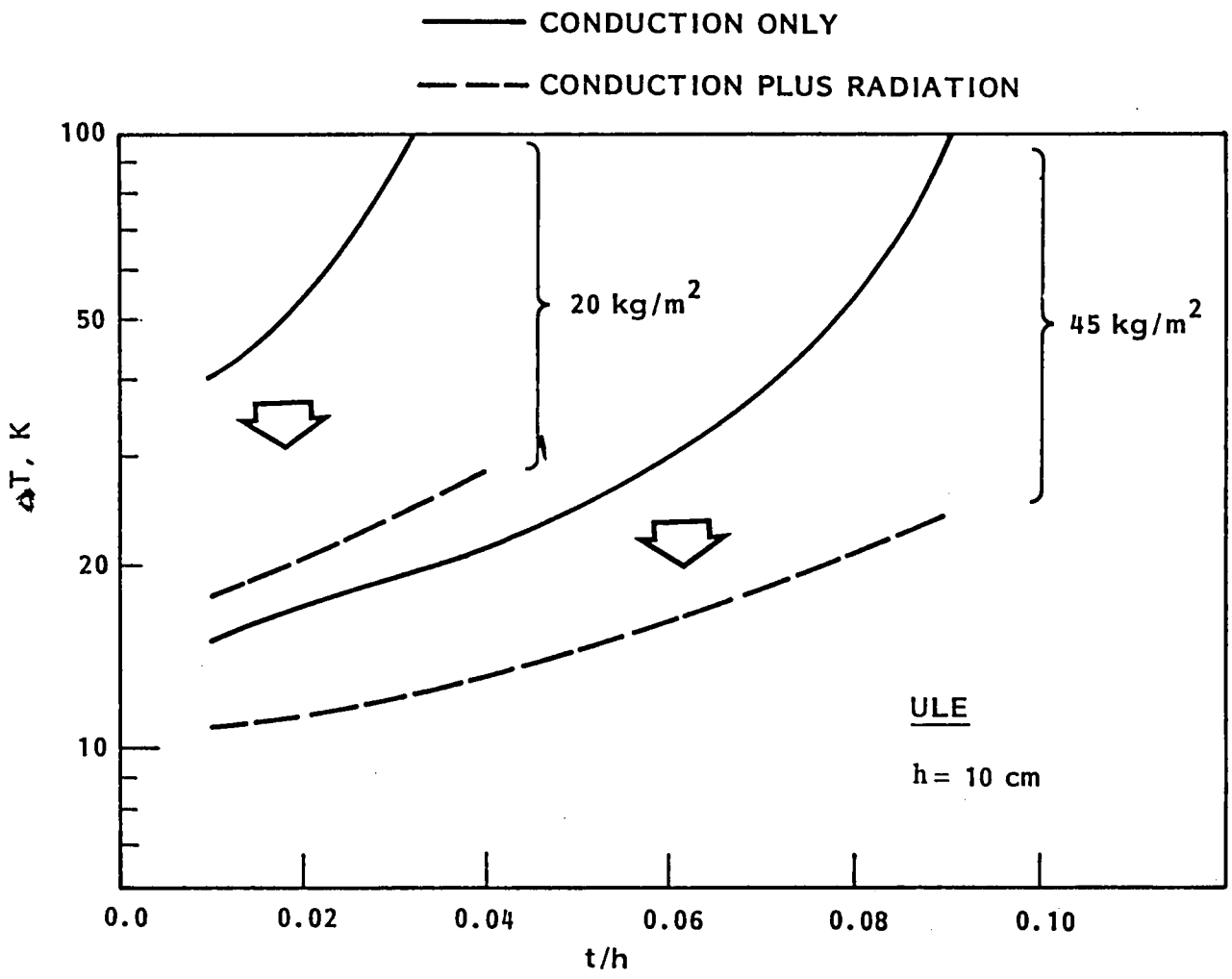

Unlike the case of ULE, where radiation from top to bottom of cells in the mirror core effectively reduces the ΔT - value by a factor 2 (typically), there is negligible effect for Aluminum. The reason is simple: the radiation transfer is effective (important) only for relatively large ΔT, whereas for Aluminum, ΔT is of the order of a degree or less. We conclude that for Aluminmum, ignoring radiation is inconsequential, whereas for ULE mirrors, the thermal bending is reduced, and by a factor 2, typically.

FRONT-TO-BACK TEMPERATURE DIFFERENCE

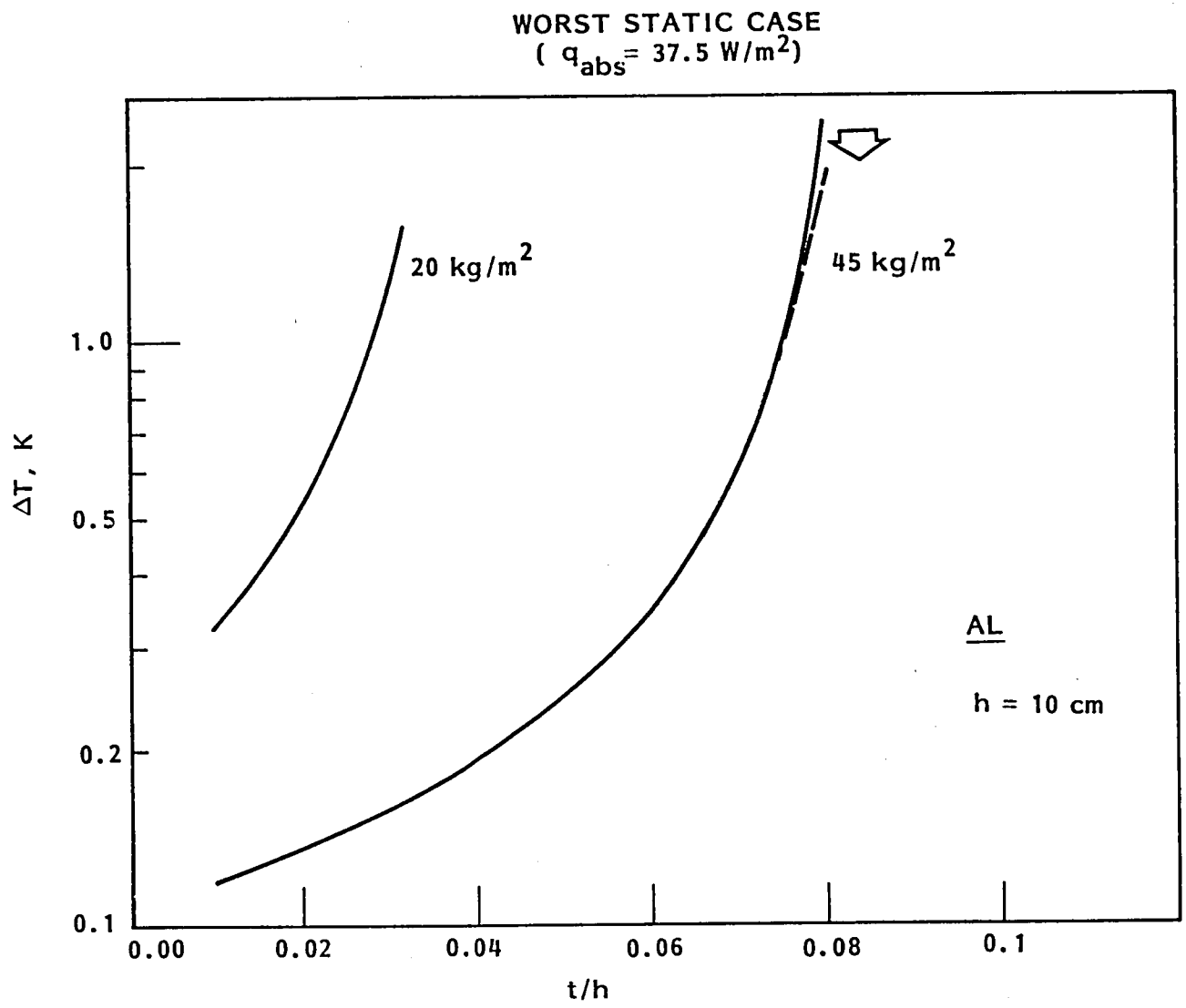

This foil shows the actual reduction in thermal bending of ULE segments* when radiation transfer in the core cells is efficient. There is negligible effect for corresponding Aluminum segments. The effects increase with increasing value of t/h because conduction through the core decreases, thereby making the radiation effect increasingly important.

---

*Arrow indicates reduction in bending

MAXIMUM MIRROR DEFLECTION

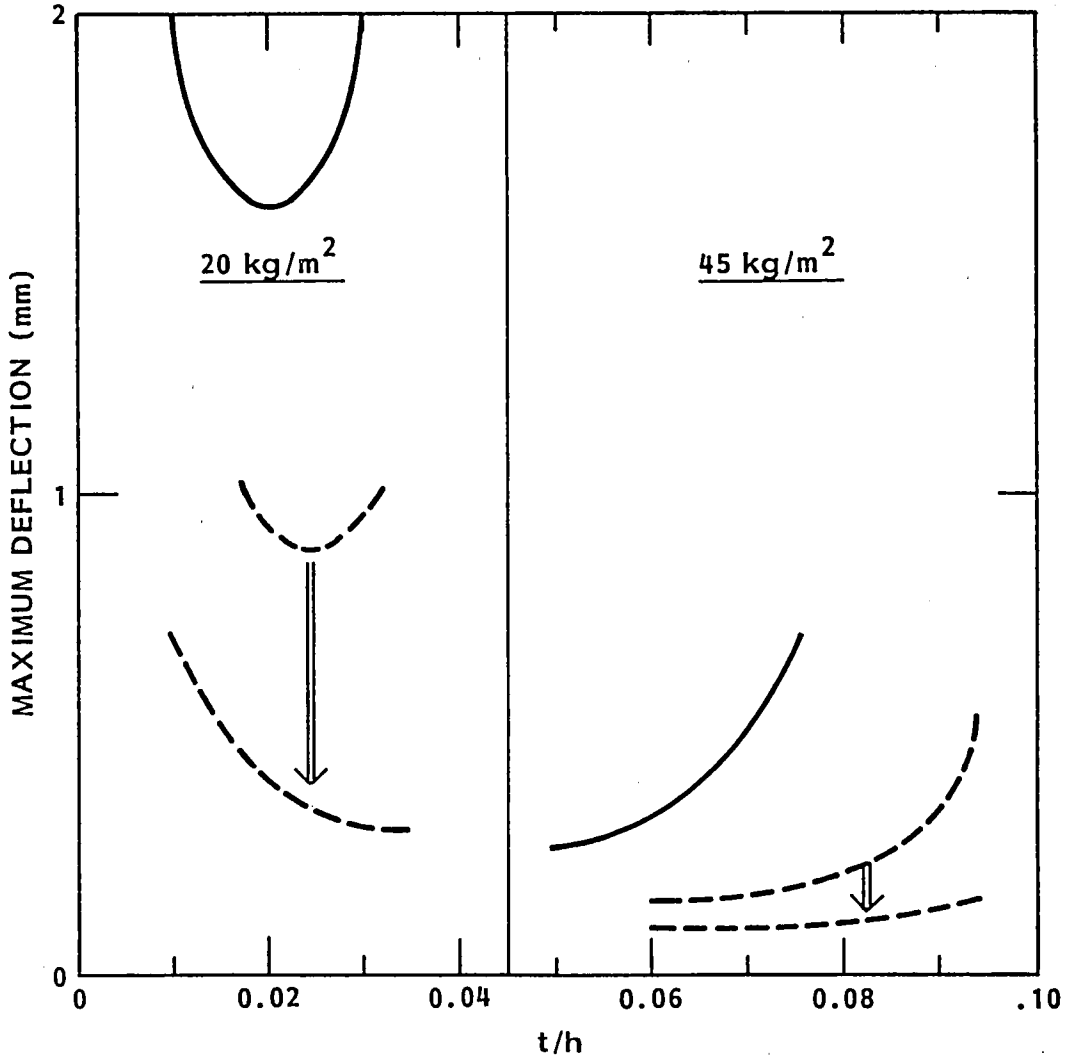

- WORST STATIC CASE
- $q = 37.5\ W/m^2$
- h = 10 cm
- ALUMINUM: ——— NEGIGIBLE EFFECT
- ULE – – – – SIGNIFICANT DECREASE IN DEFORMATION

Smoothing effects (due to orbital motion of LDR) on the temperature gradients depend on the thermal relaxation time for heat transfer. The next two foils look at the relaxation time from front-to-back, for the same types of mirror segments studied earlier. We define the relaxation time as

$$\tau = \frac{\text{transferrable heat per } {}^{o}K \text{ of } \Delta T}{\text{rate of transfer per } {}^{o}K \text{ of } \Delta T}$$

We assume that the transferrable heat is all stored in the front plate (this model certainly should be refined in future studies) and that the plates have negligible temperature gradients (compared to ΔT), and that the temperature across the plates is constant. For thermal conduction only, $\tau = \tau_c$, where

$$\tau_c = 0.5\ th\rho cr/K$$

(all qnatities defined earlier). For radiation only, $\tau = \tau_r$, where

$$\tau_r = 0.5t\rho\ c/4\sigma h \cdot T^3$$

where σ is Stefan's constant, and $T \approx T_b \approx T_f$ ($\ll T$ always true). For T we assumed the value 160 ^{o}K referring to worst-sun soak conditions. This assumption underestimates the radiative relaxation time, since the average temperature T during an orbit is lower than as assumed. Our definition of τ_c probably underestimates the relaxation time for low values of t/h by ignoring the heat stored in the core material.

THERMAL RELAXATION TIME

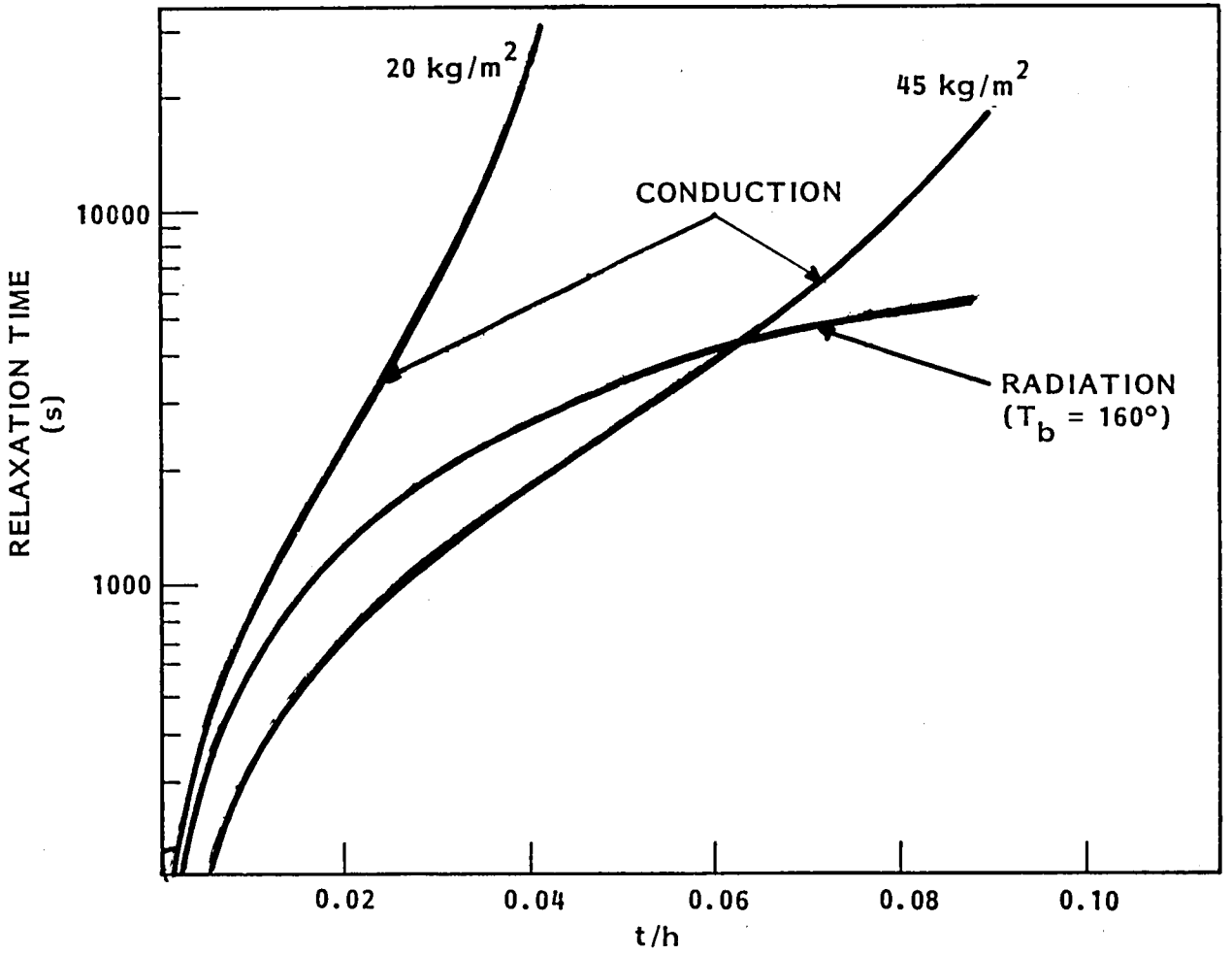

- ULE
- h = 10 cm

The orbital period of LDR (400 n.mi. nominal altitude, circular orbit) is 100 minutes. We see that the relaxation time for Aluminum is always less, even much less than the orbital period. Thus Aluminum is in a steady state as far as heat transfer through the core is concerned. Thi is not true for ULE (previous foil). Thus orbital smoothing effects are operative for ULE but not Aluminum. (In effect, for large relaxation times, the back plate of the mirror is at a constant temperature i.e. varies little with time over an orbit).

THERMAL RELAXATION TIME

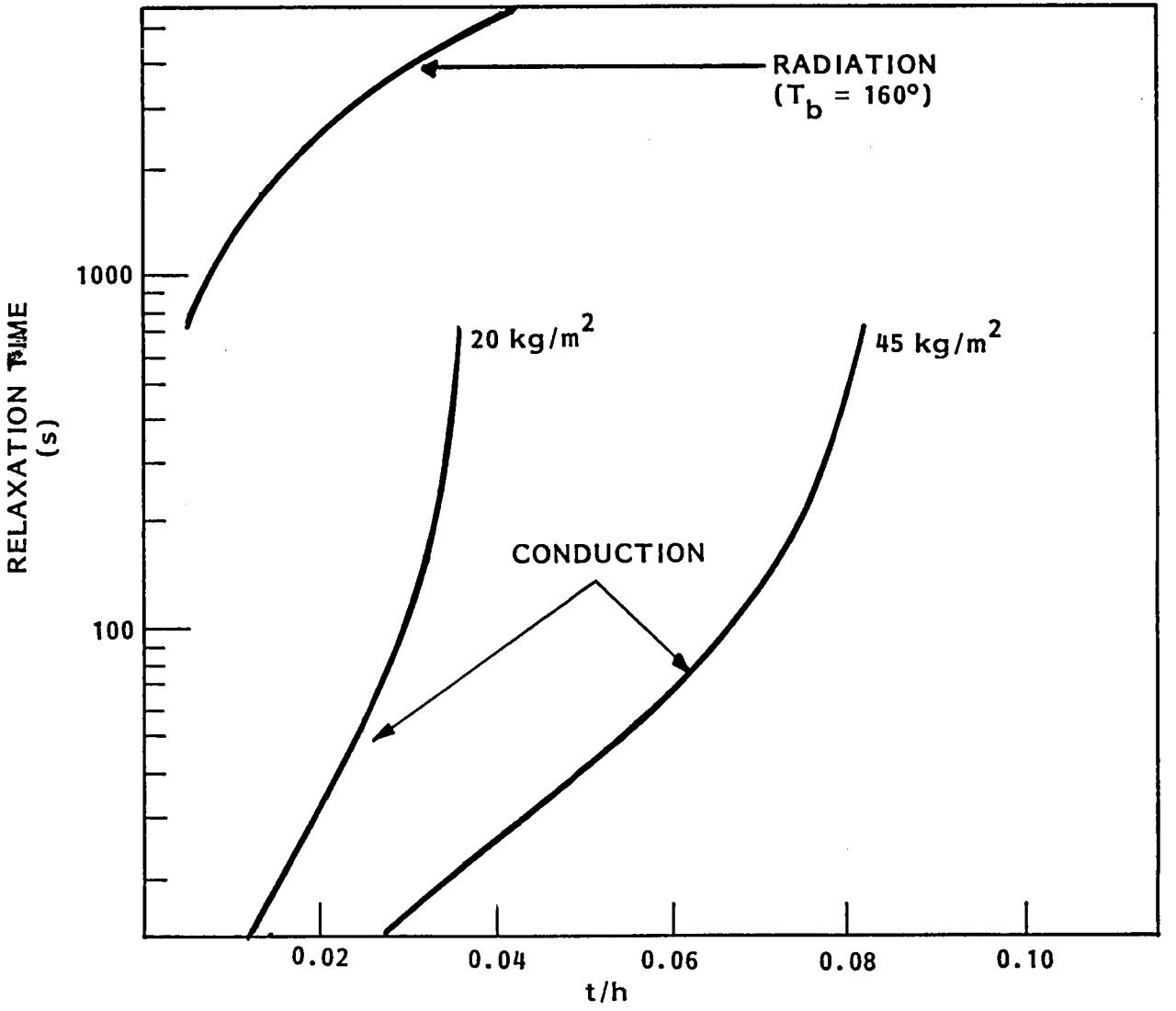

- ALUMINUM
- h = 10 cm

This foil shows the front and back surface temperatures of a ULE segment of h=10 cm height, mass/area ratio m/A=20 kg/m^2, and plate thickness of 2 mm, as a function of orbit time. The orbit is in the plane of the earth orbit, and the segment faces south (i.e. no heat load by the sun on the mirror) As before, there is no heat load assumed on the back plate. Radiation and conduction are taken into consideration. Because of the large time constant, there is a nearly constant back surface temperature

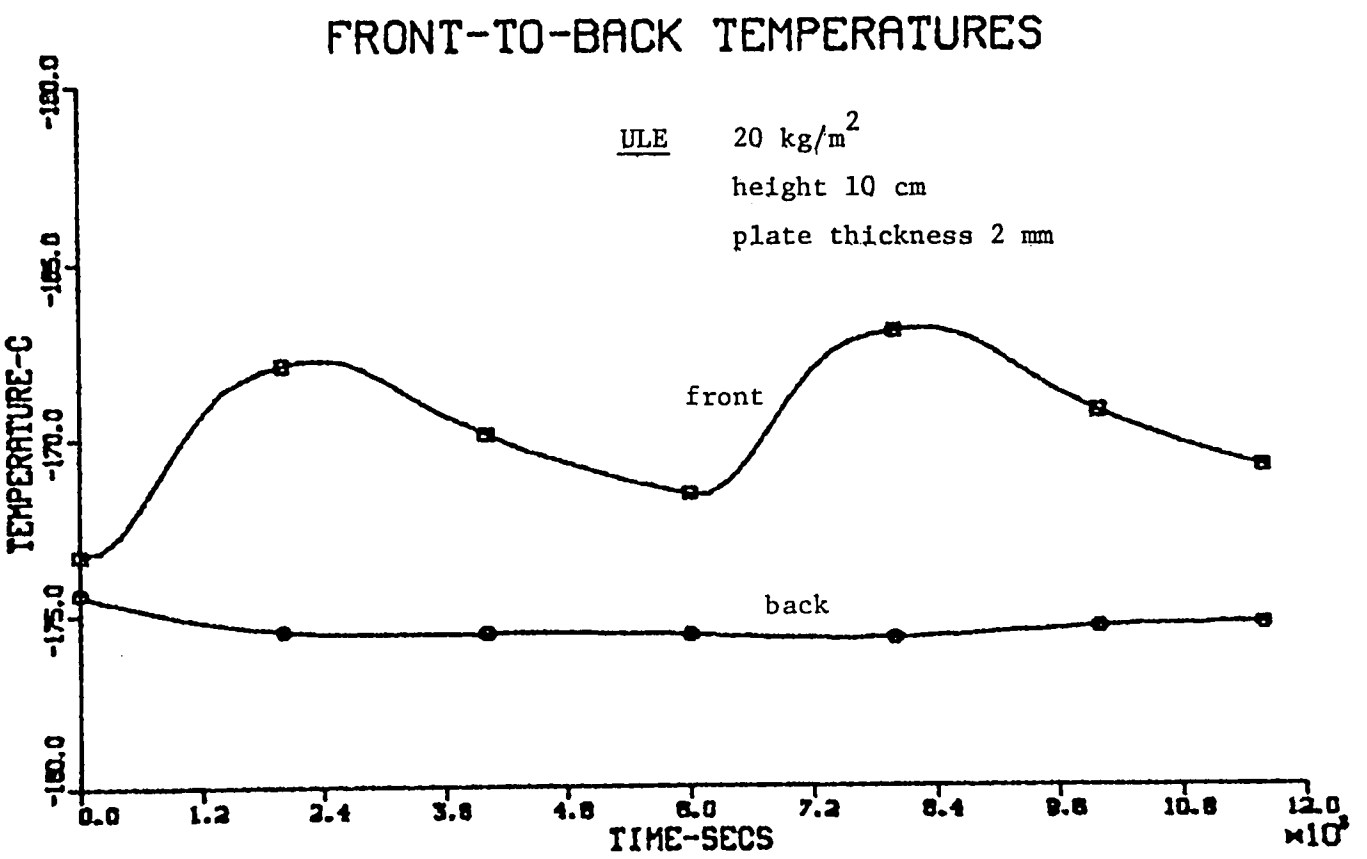
FRONT-TO-BACK TEMPERATURES
ULE
20 kg/m2
height 10 cm
plate thickness 2 mm
front
back
TEMPERATURE-C
-160.0
-165.0
-170.0
-175.0
-180.0
0.0
1.2
2.4
3.6
4.8
6.0
7.2
8.4
9.6
10.8
12.0
TIME-SECS
x10³

In the case of Aluminum, in contrast with ULE segements with the same values of m/A, h and t, and the same orbit as in the previous foil, the back surface varies as much as the front - there is little "smoothing" effect because of the short time constant.

ORBITAL TEMPERATURE VARIATIONS

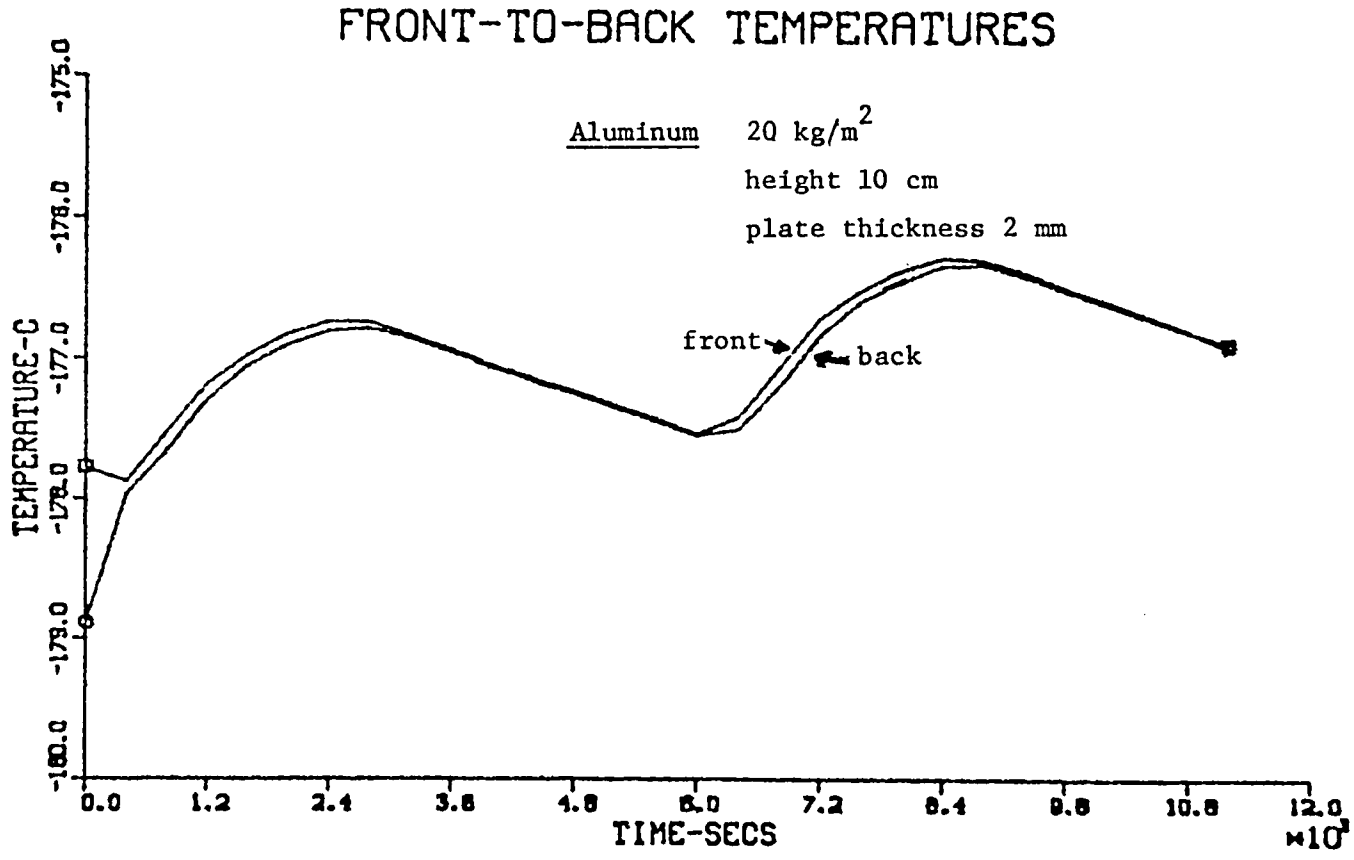

This foil shows that if dynamic effects (i.e. the effect of a finite time constant) are ignored, the change in front-to-back temperature difference during an orbit, per unit change of heat load, Δq, is not only overestimated but also shows a completely different dependence on the plate thickness, t (constant h in this foil, h = 10 cm). Here, only thermal conduction was considered. While for the "static" case (zero time constant assumed)

$$\Delta(\Delta T) \underset{\sim}{\propto} h \Delta q \, r$$

and thus the change in (ΔT) increases with increasing value of t/h (since, for constant h and m/A, the plate/core area ratio increases), for the "dynamic" case (finite time constant),

$$\Delta(\Delta T) \underset{\sim}{\propto} 1/t \cdot \Delta q$$

which decreases with increasing value of t/h because the front-plate heat capacity increases, and changes in q have less and less effect on the plate temperature.

MAX. CHANGE IN FRONT-BACK TEMPERATURE DIFFERENCE

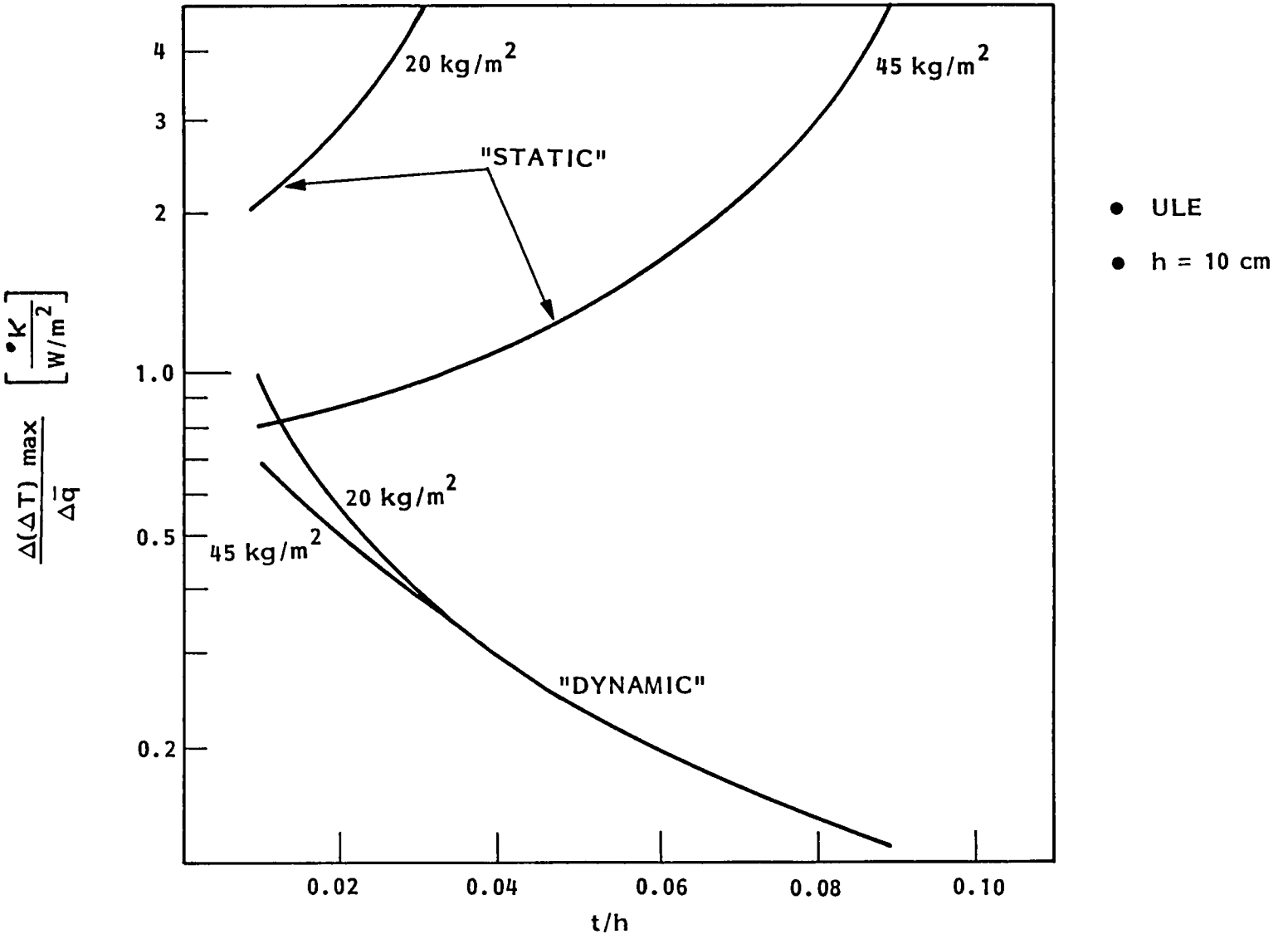

In the remaining foils we show the effects on temperature gradients and their time variation (orbit effects) of adding a 20 m lon cylindrical baffle to a 20 m diameter ULE or Aluminum lightweight mirror. The F/ratio of the mirror is 0.5, the mirror thickness is 10 cm, the plate thickness (front or back) is 2 mm. The front surface has α/ε = 0.05/0.03. The mirror back surface has ε=0.82, and there is no heat input assumed to the back (same as before). The baffle has α'/ε =0.05/0.03 outside and α'/ε =0.88/0.95 inside. The mirror is continuous, so that there is maximum heat transfer across the surface (the surface gradients are therefore underestimated). However, most of the heat transfer is through, rather than across, the mirror. Therefore the simplifying assumption of a continuous, rather than segmented, mirror may be rather inconsequential for our purposes. The surface is divided into 36 thermal nodes.

The results for m/A=20 kg/m^2 and for 45 kg/m^2, respectively, are similar. Of course, the settling times for the heavier mirror are longer. The reductions of thermal gradients and their time variations by the addition of the baffle will be less for shorter baffles, or other types of sun shields, because of the lesser shielding from the earth shine.

MIRROR

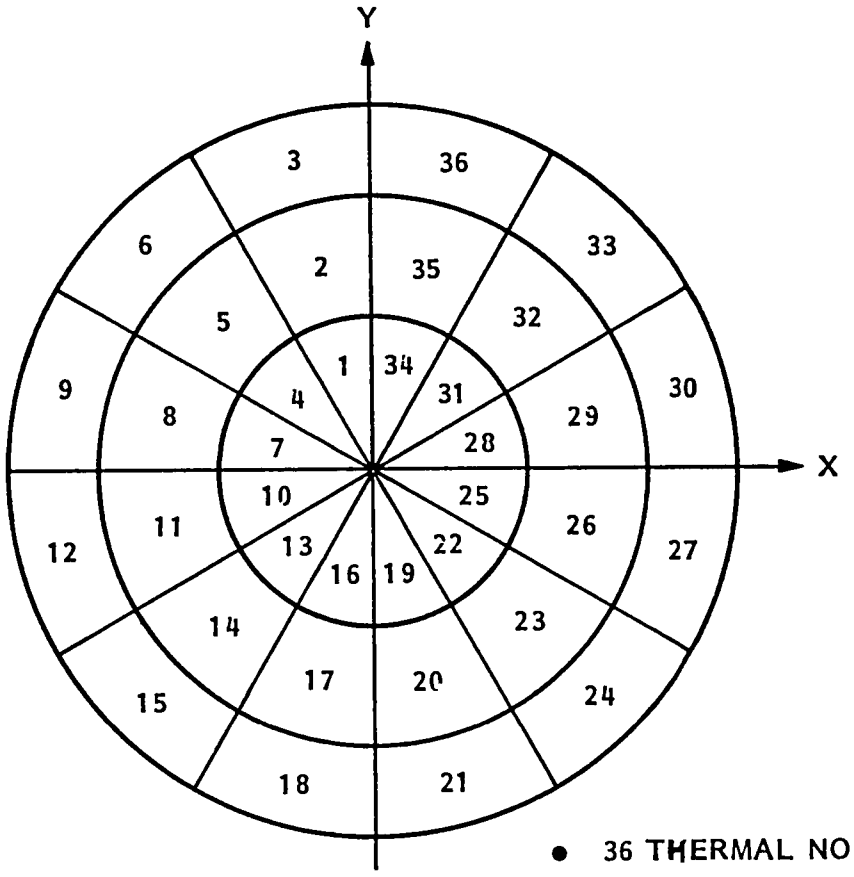

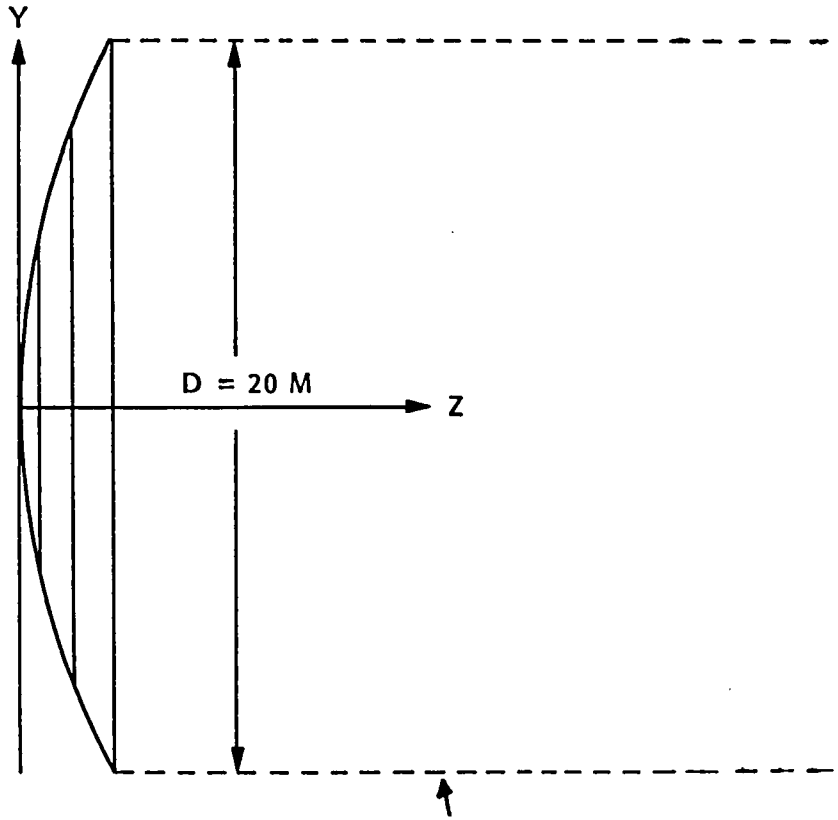

- 36 THERMAL NODES
- F/0.5
- 20 M CYLINDRICAL SUNSHADE

This foil shows the mirror orbit and orientation relative to the orbit, sun and earth. The mirror is approximately 1/3 of the time in the earth's shade.

ORBIT

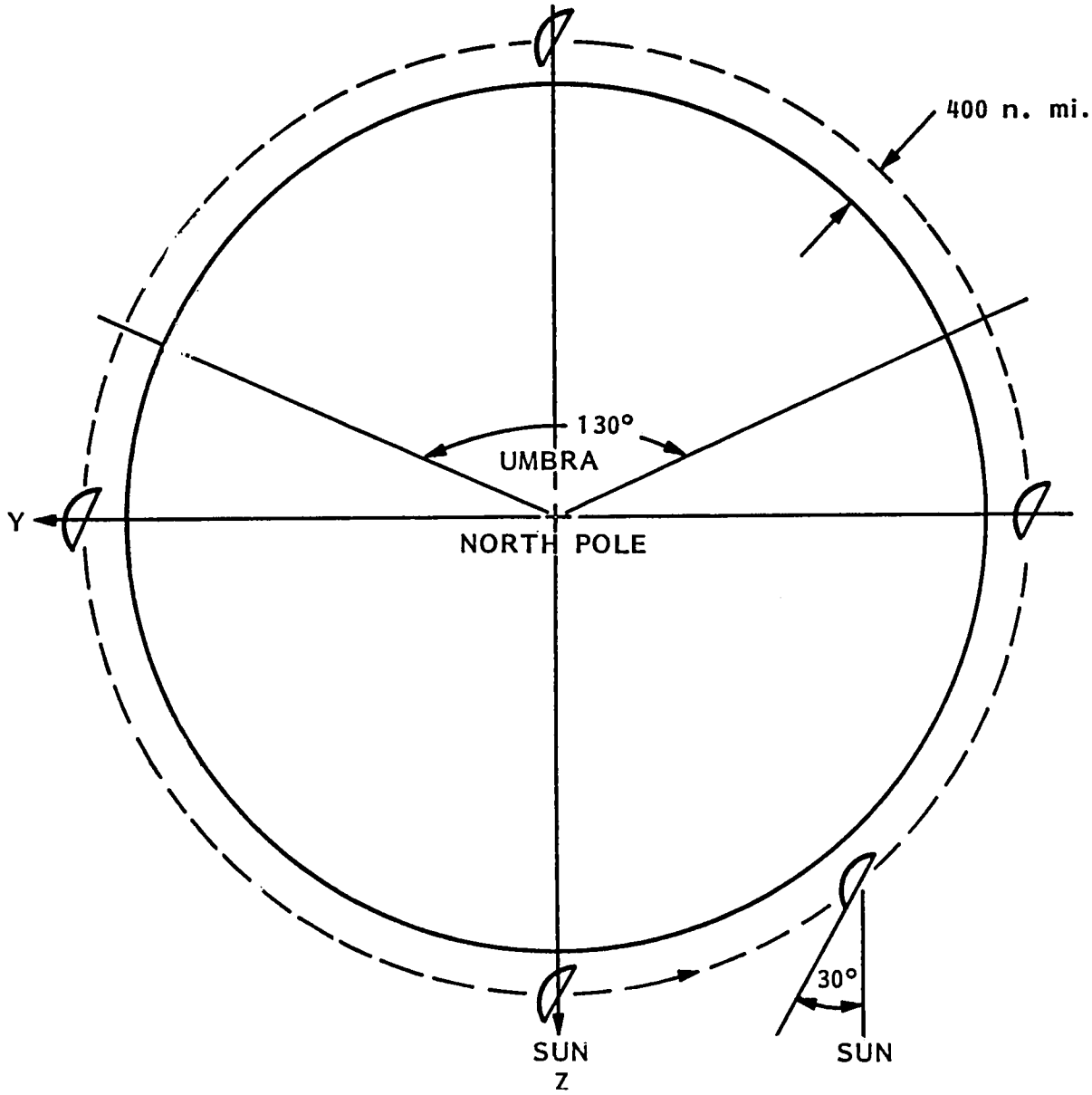

- 400 n. mi. ORBIT CIRCULAR IN S–E ORBIT PLRNE (β = O)
- MIRROR NORMAL 60° FROM S–E LINE

This foil shows the differences between local and average mirror temperature at the sub-solar point for ULE. The maximum difference without the 20 m baffle (unshielded mirror) is 55 ^{o}K, while with a baffle it is reduced to only 7.5 ^{o}K, a factor of 7 reduction.

DEVIATIONS FROM MEAN SURFACE TEMPERATURE (°K)

- SUB-SOLAR PT.
- ULE
- 20 kg/m²

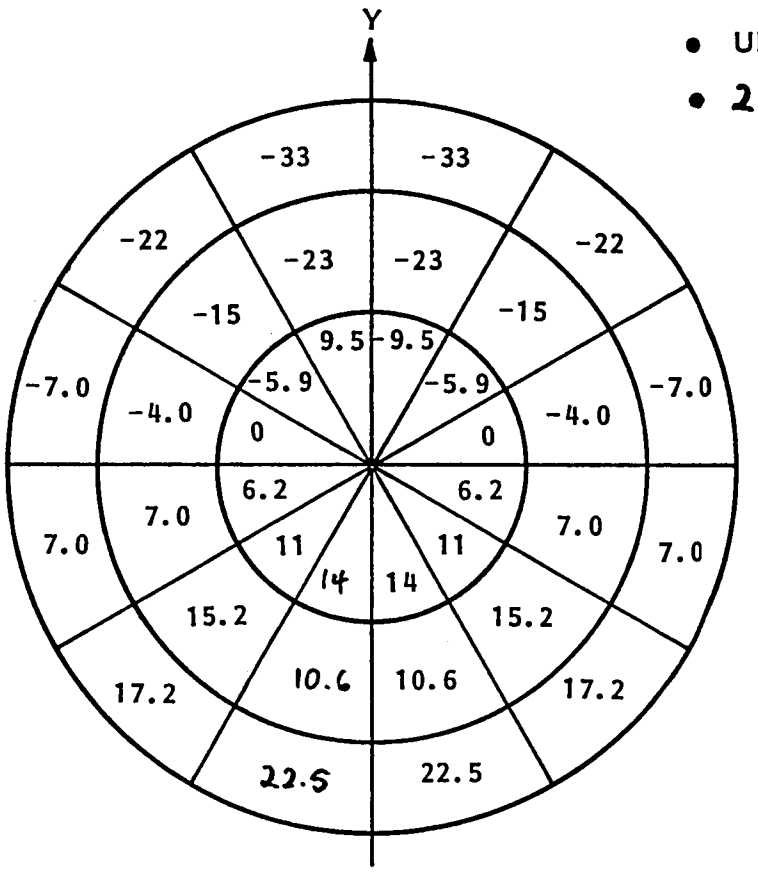

WITHOUT BAFFLE
ΔT_{MAX} = 55°K

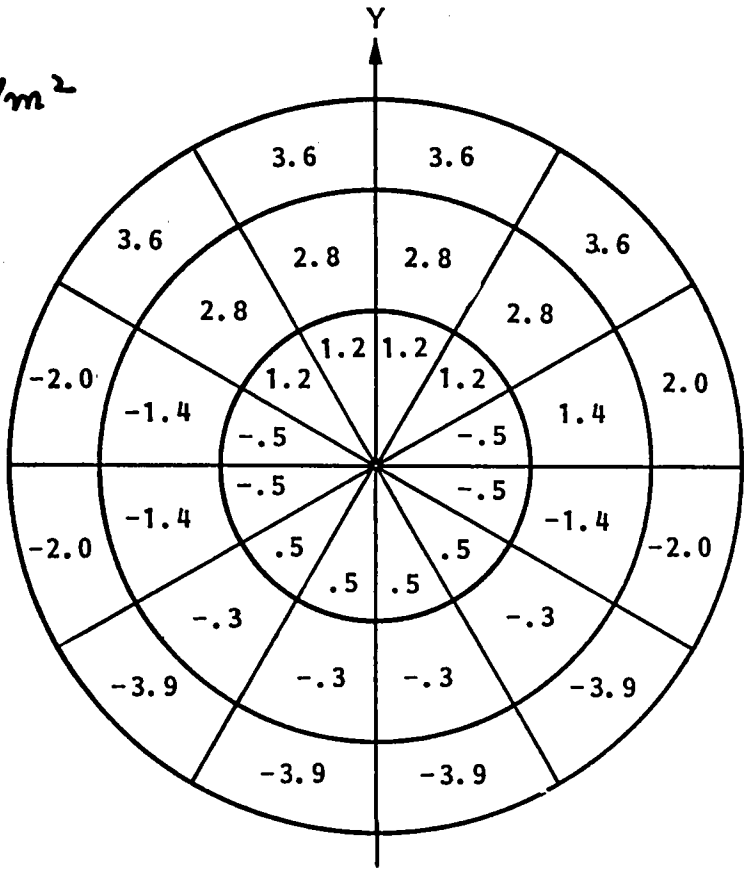

WITH BAFFLE
ΔT_{MAX} = 7.5°K

DEVIATIONS FROM MEAN SURFACE TEMPERATURE (°K)

- ULE
- 45 kg/m^2

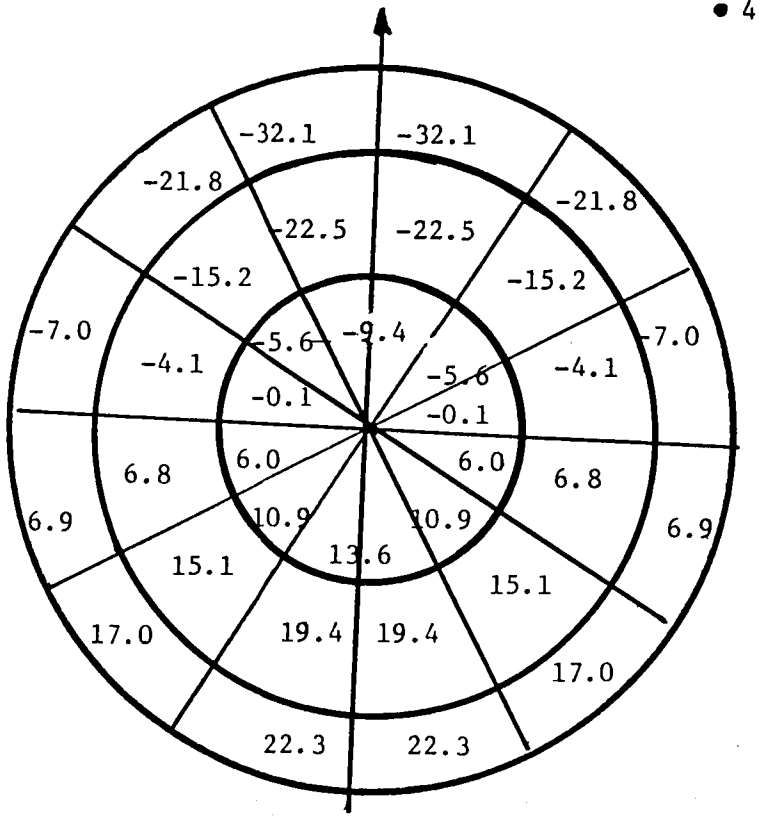

WITHOUT BAFFLE

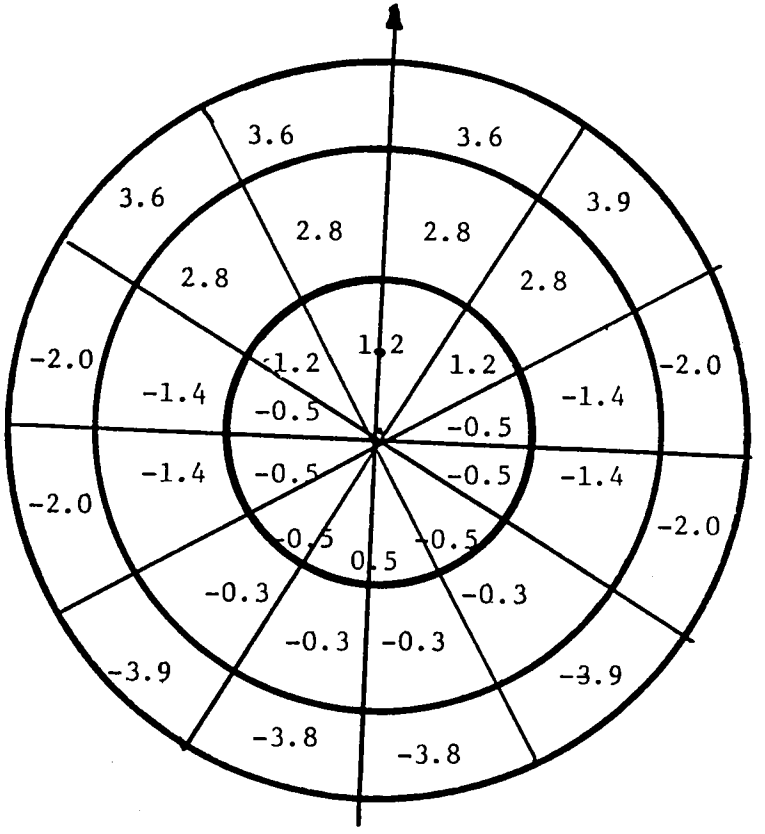

With BAFFLE

For the Aluminmum mirror, the reduction surface temperature gradients by adding the 20 m baffle is somewhat less than for ULE, from 45 ^{o}K to 9.5 ^{o}K, a factor about 5.

DEVIATIONS FROM MEAN SURFACE TEMPERATURE (°K)

- SUB-SOLAR PT.
- ALUMINUM
- 20 kg/m²

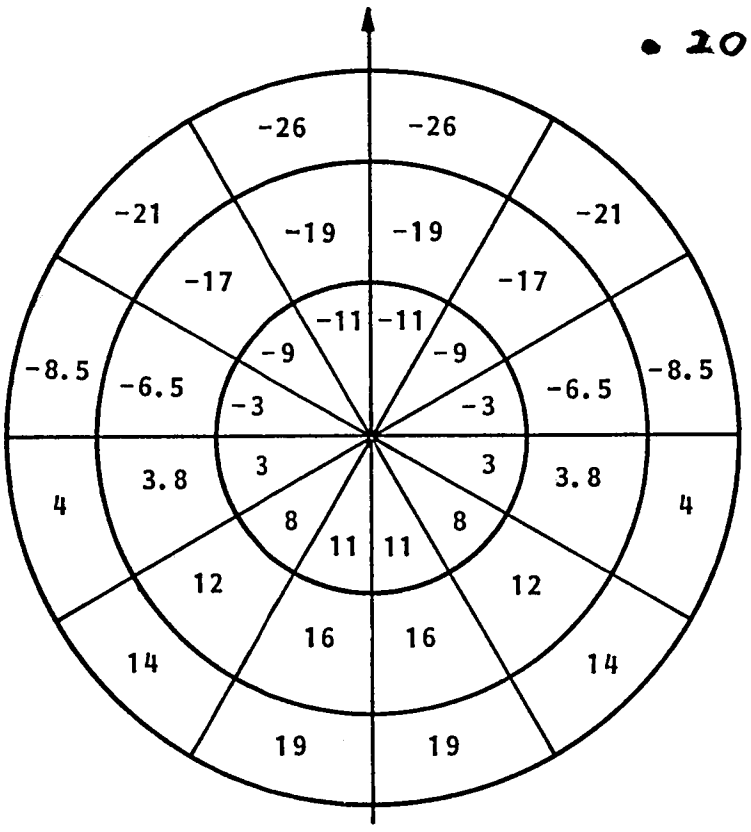

WITHOUT BAFFLE
$\Delta T_{MAX} = 45$

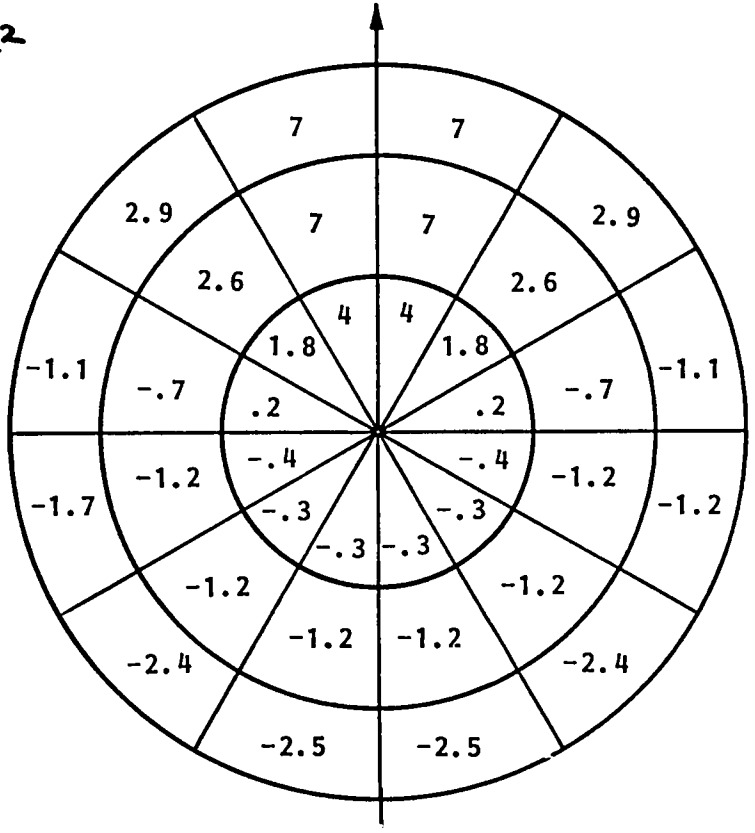

WITH BAFFLE
$\Delta T_{MAX} = 9.5$

DEVIATIONS FROM MEAN SURFACE TEMPERATURE (°K)

Al

45 kg/m^2

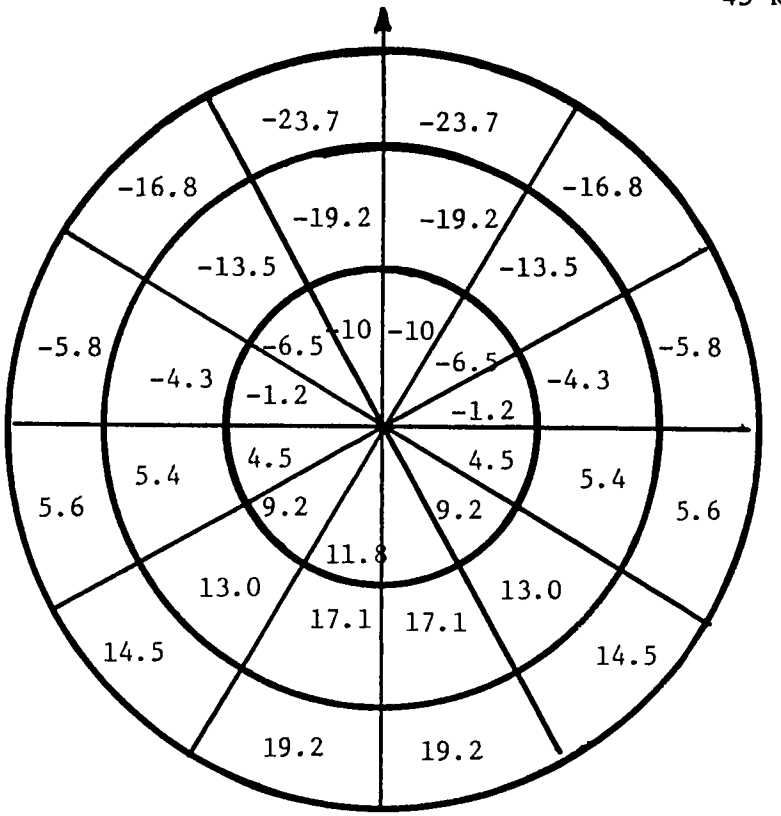

WITHOUT BAFFLE

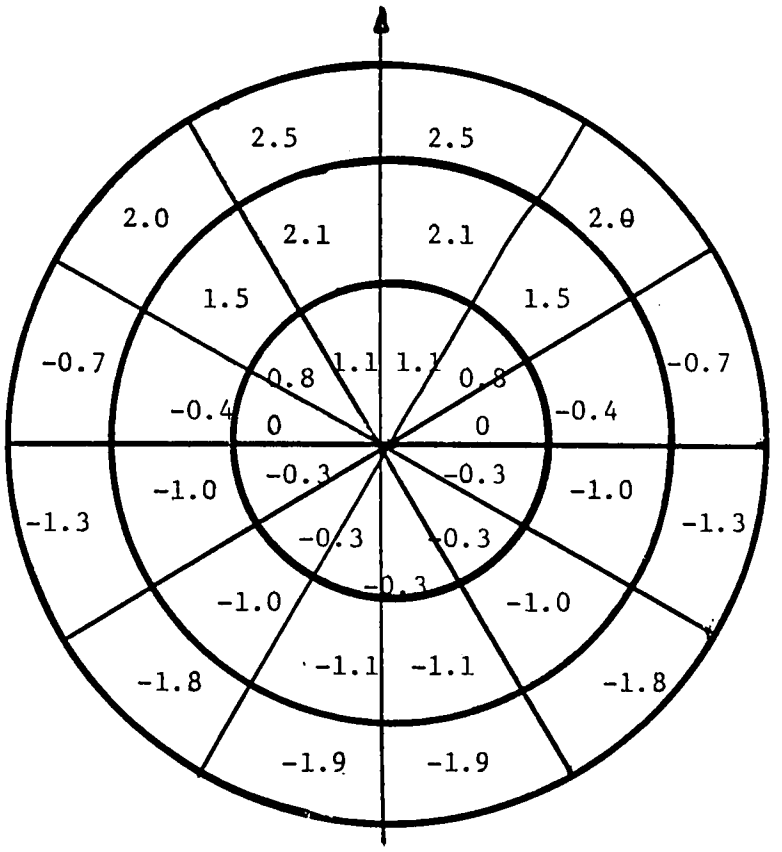

WITH BAFFLE

This foil shows, for ULE, the maximum temporal variation of front surface temperatures for the unshielded and shielded mirror. The variations are reduced by at least a factor of 2 by adding the 20 m baffle to the mirror.

MAXIMUM ORBITAL VARIATION OF SURFACE TEMPERATURE (°K)

- ULE
- 20 kg/m²

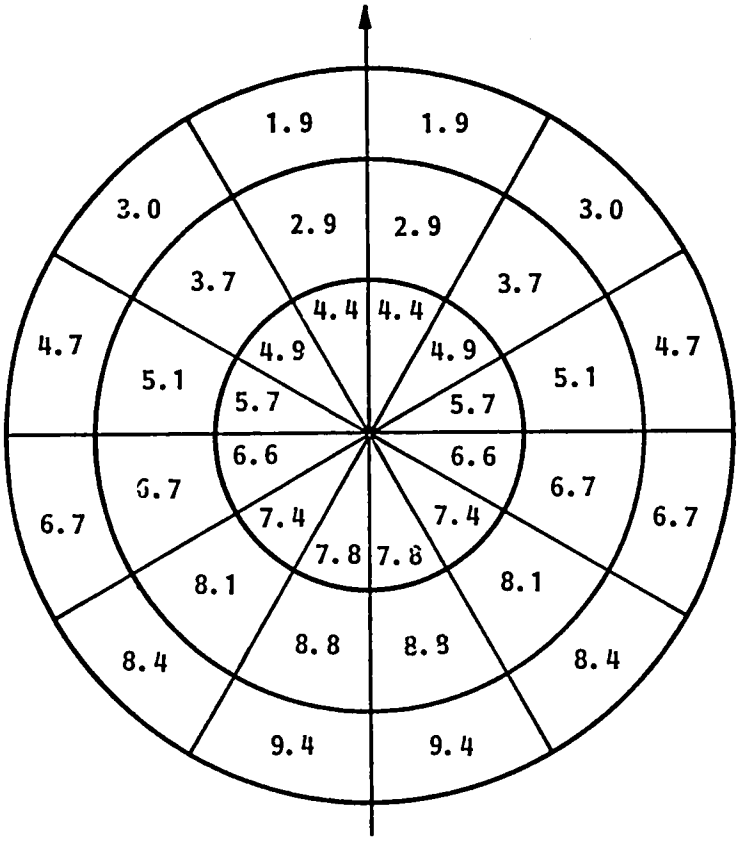

WITHOUT BAFFLE

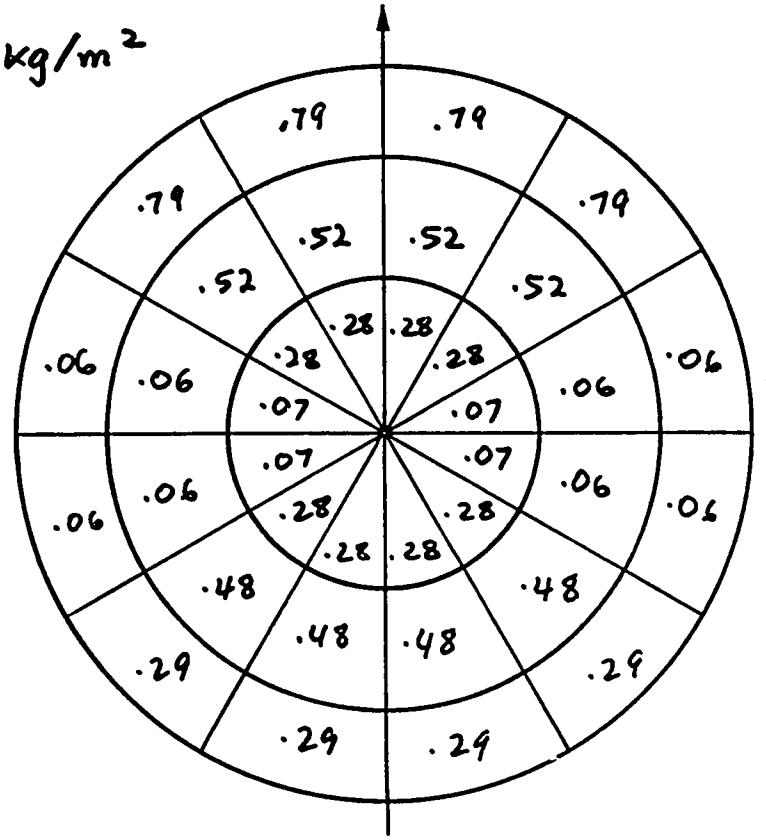

WITH BAFFLE

LDR

MAXIMUM ORBITAL VARIATION OF SURFACE TEMPERATURE ($^{\circ}$K)

ULE

45 kg/m^2

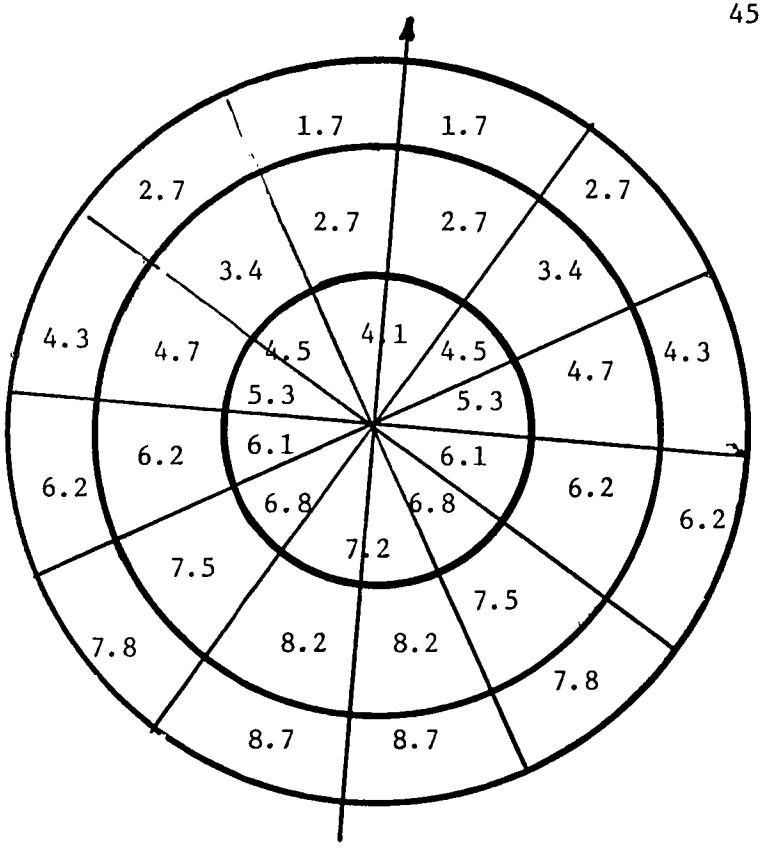

WITHOUT BAFFLE

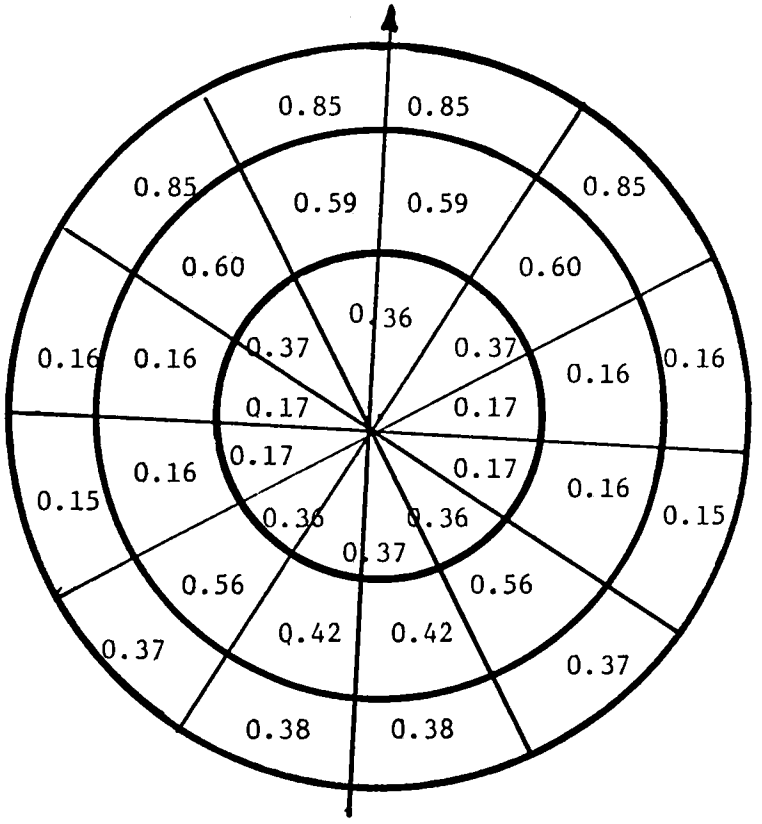

WITH BAFFLE

The maximum temporal variations of front surface temperatures for Aluminum mirrors are also reduced by a factor of 2 or more due to the addition of the baffle. - The change in surface temperature during the orbit can be related to a change in front-to-back temperature difference, assuming heat conduction only and a steady-state condition (justified because of the short time constant for Aluminum):

$$\Delta(\Delta T) = [4h_r T_f^3 \sigma / k] \Delta T_f$$

where T_f the temporal average of the front surface temperature (local), where all other quantities were defined earlier. The thermal deformation of a mirror, for a flat mirror and with no across gradients, is proportional to (ΔT). Ignoring the curvature of the mirror and the across gradients, we can therefore estimate the reduction in the mirror deformation due to changes in the through-the-mirror temeperature gradient changes: This reduction is about a factor 6 at worst (least reduction in surface temperature variation), much better in many cases, as the foil shows. Consequently, keeping in mind the simplifying assumptions made above, we can conclude that the minimum operational wavelength of the Aluminum mirror is reduced from the earlier estimate, based on static thermal conside rations and assuming no baffle, of 500 μm to less than 100 μm.

MAXIMUM ORBITAL VARIATION OF SURFACE TEMPERATURE (°K)

- ALUMINUM
- 20 kg/m²

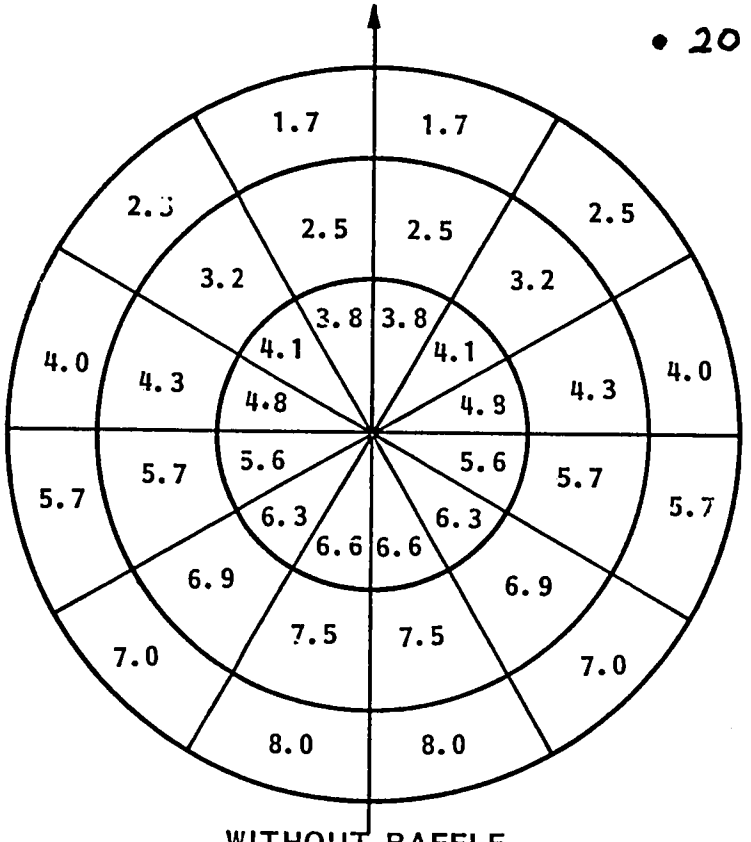

WITHOUT BAFFLE

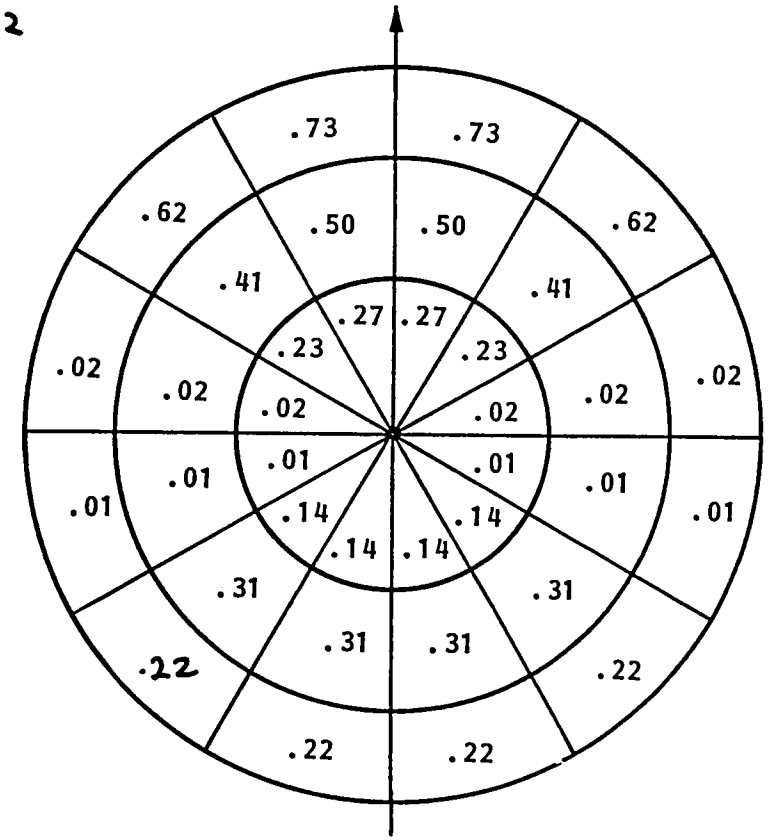

WITH BAFFLE

MAXIMUM ORBITAL VARIATION OF SURFACE TEMPERATURE (°K)

AL

45 kg/m^2

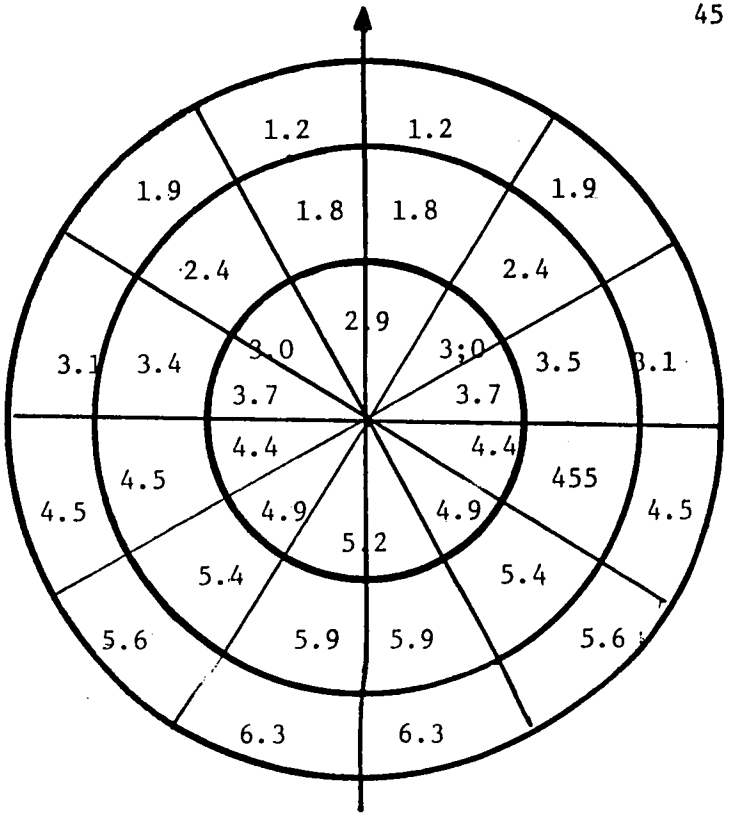

WITHOUT BAFFLE

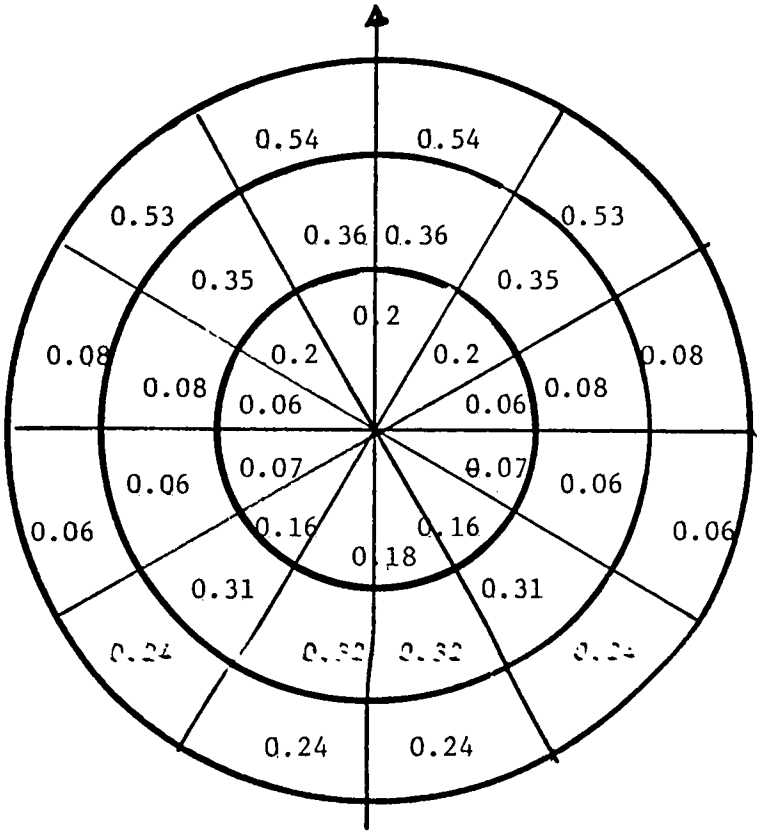

WITH BAFFLE

1. Report No.	2. Government Accession No.	3. Recipient's Catalog No.
NASA CR-152402		

4. Title and Subtitle	5. Report Date
Large Deployable Reflector (LDR)	December 15, 1980
	6. Performing Organization Code
7. Author(s) W. H. Alff, L. W. Bandermann M. K. Bartosewcz, R. H. Pohle	8. Performing Organization Report No. LMSC-D766449
	10. Work Unit No. T-5927
9. Performing Organization Name and Address Lockheed Missiles & Space Company, Inc. Palo Alto, California 94304	11. Contract or Grant No. NAS2-10427
	13. Type of Report and Period Covered CR Final Report
12. Sponsoring Agency Name and Address National Aeronautics & Space Administration Washington, D.C. 20546	14. Sponsoring Agency Code RTOP 506-62-41

15. Supplementary Notes

Technical Monitor - Thomas R. Pochari, Mail Stop 244-7, NASA Ames Research Center, Moffett Field, CA 94035 (415) 965-5708 FTS 448-5708

16. Abstract

The results of a technology study are presented for a large, ambient temperature, orbiting astronomical reflecting telescope, which is diffraction-limited at 30 μm. The reflector (LDR) is deployed with one Shuttle load into a ten-year lifetime orbit in the early 1990s. A 10- to 30-m diameter reflector was determined to be feasible with the mirror fabrication and control technology which is now in development.

17. Key Words (Suggested by Author(s))	18. Distribution Statement
Large Deployable Reflector Telescope (LDRT), Mirror Fabrication, Alignment System, Segmented Glass Mirror	Unclassified - Unlimited STAR Category 89

19. Security Classif. (of this report)	20. Security Classif. (of this page)	21. No. of Pages	22. Price*
Unclassified	Unclassified	179	

*For sale by the National Technical Information Service, Springfield, Virginia 22161